Theses and Dissertations   1. Thesis and Dissertation Collection, all items

2010-09

Sensitivity of the meridional overturning circulation to the pattern of the surface density flux

Lewis, David Reid.

Monterey, California. Naval Postgraduate School

https://hdl.handle.net/10945/5195

NAVAL POSTGRADUATE SCHOOL

MONTEREY, CALIFORNIA

THESIS

SENSITIVITY OF THE MERIDIONAL OVERTURNING CIRCULATION TO THE PATTERN OF THE SURFACE DENSITY FLUX

by

David Reid Lewis

September 2010

Thesis Advisor:	Timour Radko
Second Reader:	Gabriele Jost

THIS PAGE INTENTIONALLY LEFT BLANK

REPORT DOCUMENTATION PAGE		*Form Approved OMB No. 0704-0188*
Public reporting burden for this collection of information is estimated to average 1 hour per response, including the time for reviewing instruction, searching existing data sources, gathering and maintaining the data needed, and completing and reviewing the collection of information. Send comments regarding this burden estimate or any other aspect of this collection of information, including suggestions for reducing this burden, to Washington headquarters Services, Directorate for Information Operations and Reports, 1215 Jefferson Davis Highway, Suite 1204, Arlington, VA 22202-4302, and to the Office of Management and Budget, Paperwork Reduction Project (0704-0188) Washington DC 20503.
1. AGENCY USE ONLY *(Leave blank)*	**2. REPORT DATE** September 2010	**3. REPORT TYPE AND DATES COVERED** Master's Thesis
4. TITLE AND SUBTITLE Sensitivity of the Meridional Overturning Circulation to the Pattern of the Surface Density Flux		**5. FUNDING NUMBERS**
6. AUTHOR(S) David Reid Lewis		
7. PERFORMING ORGANIZATION NAME(S) AND ADDRESS(ES) Naval Postgraduate School Monterey, CA 93943-5000		**8. PERFORMING ORGANIZATION REPORT NUMBER**
9. SPONSORING /MONITORING AGENCY NAME(S) AND ADDRESS(ES) N/A		**10. SPONSORING/MONITORING AGENCY REPORT NUMBER**
11. SUPPLEMENTARY NOTES The views expressed in this thesis are those of the author and do not reflect the official policy or position of the Department of Defense or the U.S. Government. IRB Protocol number _____N/A_____.
12a. DISTRIBUTION / AVAILABILITY STATEMENT Approved for public release; distribution is unlimited		**12b. DISTRIBUTION CODE**
	13. ABSTRACT (maximum 200 words) The dynamic response of the thermocline to the thermodynamic forcing at the sea surface is analyzed in terms of its ability to influence the pattern of the oceanic meridional overturning. The technique utilized in this study expands upon an improved version of Walin's (1982) water-mass transformation theory, developed by Radko et al. (2008). Utilizing a general circulation model (GCM), two series of experiments are performed where surface air-sea density flux distributions are systematically perturbed in different locations to test the Meridional Overturning Circulation (MOC) response. The experiments are diagnosed using the water-mass transformation theory, which makes it possible to quantify the role of adiabatic processes in the global overturning circulation.

Through these tests, this study finds that adiabatic processes dominate the MOC in the upper ocean and that the general circulation structure can be described using the improved water-mass transformation model. However, strength of flow in the Western Boundary regions is not well described by the theoretical model. The highest sensitivity of the MOC to thermodynamic forcing is found in the eastern Atlantic circumpolar regions while western boundary regions are characterized by low sensitivity. Further, the MOC does not show a high sensitivity to heating perturbations in the context of a larger zonal temperature structure. The finding is significant in its potential application to U.S. Navy's ocean modeling efforts and long-term strategy related to climate change. |
14. SUBJECT TERMS Meridional Overturning Circulation, Thermohaline Circulation, Thermocline, Residual-Mean Theory, Air-Sea Fluxes, Surface Density Flux , Mixed-Layer Density, Water-mass Transformation		**15. NUMBER OF PAGES** 105
		16. PRICE CODE
17. SECURITY CLASSIFICATION OF REPORT Unclassified	**18. SECURITY CLASSIFICATION OF THIS PAGE** Unclassified	**19. SECURITY CLASSIFICATION OF ABSTRACT** Unclassified / **20. LIMITATION OF ABSTRACT** UU

NSN 7540-01-280-5500

Standard Form 298 (Rev. 2-89)
Prescribed by ANSI Std. 239-18

i

THIS PAGE INTENTIONALLY LEFT BLANK

SENSITIVITY OF THE MERIDIONAL OVERTURNING CIRCULATION TO THE PATTERN OF THE SURFACE DENSITY FLUX

David Reid Lewis
Lieutenant Commander, United States Navy
B.S., Rensselaer Polytechnic Institute, 1998

Submitted in partial fulfillment of the
requirements for the degree of

MASTER OF SCIENCE IN METEOROLOGY AND PHYSICAL OCEANOGRAPHY

from the

**NAVAL POSTGRADUATE SCHOOL
September 2010**

Author: David Reid Lewis

Approved by: Timour Radko
               Thesis Advisor

               Gabriele Jost
               Second Reader

               Jeff Paduan
               Chairman, Department of Oceanography

iii

THIS PAGE INTENTIONALLY LEFT BLANK

ABSTRACT

The dynamic response of the thermocline to the thermodynamic forcing at the sea surface is analyzed in terms of its ability to influence the pattern of the oceanic meridional overturning. The technique utilized in this study expands upon an improved version of Walin's (1982) water-mass transformation theory, developed by Radko et al. (2008). Utilizing a general circulation model (GCM), two series of experiments are performed where surface air-sea density flux distributions are systematically perturbed in different locations to test the Meridional Overturning Circulation (MOC) response. The experiments are diagnosed using the water-mass transformation theory, which makes it possible to quantify the role of adiabatic processes in the global overturning circulation.

Through these tests, this study finds that adiabatic processes dominate the MOC in the upper ocean and that the general circulation structure can be described using the improved water-mass transformation model. However, strength of flow in the Western Boundary regions is not well described by the theoretical model. The highest sensitivity of the MOC to thermodynamic forcing is found in the eastern Atlantic circumpolar regions while western boundary regions are characterized by low sensitivity. Further, the MOC does not show a high sensitivity to heating perturbations in the context of a larger zonal temperature structure. The finding is significant in its potential application to U.S. Navy's ocean modeling efforts and long-term strategy related to climate change.

THIS PAGE INTENTIONALLY LEFT BLANK

TABLE OF CONTENTS

LIST OF FIGURES

x

THIS PAGE INTENTIONALLY LEFT BLANK

LIST OF TABLES

THIS PAGE INTENTIONALLY LEFT BLANK

LIST OF ACRONYMS AND ABBREVIATIONS

ACC	Antarctic Circumpolar Current
AMOC	Atlantic Meridional Overturning Circulation
EBC	Eastern Boundary Current
ECMWF	European Centre for Medium-Range Weather Forecasts
GCM	General Circulation Model
MITgcm	Massachusetts Institute of Technology general circulation model
MGD	Meridional Density Gradient
MOC	Meridional Overturning Circulation
Sv	Sverdrup
WBC	Western Boundary Current

THIS PAGE INTENTIONALLY LEFT BLANK

ACKNOWLEDGMENTS

In no way could I have accomplished this project without the help and support of a great number of people. The faculty members for the oceanography, meteorology, and math departments have all been extremely helpful to me as I have progressed through this curriculum. Many thanks to each of you for all of the additional time you spent answering my questions and instructing me in your respective fields of expertise. Thanks also to Donna Cuadrez and the rest of the thesis processing group for your time and expertise.

The numerical modeling and technical components of this experiment would not have been possible without the patient help of the High Performance Computing (HPC) group here at NPS. Most notably, Dr. Jeff Hafferman, Brian Andrus, and Eric Adint were always there to quickly help me resolve the many issues I had setting up numerical experiments. Special thanks goes to Dr. Gabriele Jost, for the innumerable hours she spent helping me with the coding issues I was having. I am extremely grateful to have had each of you help open my eyes to the field of high performance computing.

I am extremely grateful to have had Dr. Timour Radko as my advisor. I cannot thank him enough for all of the mentoring, support, and patience he provided throughout this process. It was an honor to work for such an exceptional instructor and thesis advisor.

To my friends, the members of my section (the magnificent 7): this is the most close-knit group I have had the privilege of being a part of in my career. Thanks for all of your support, and for helping me transition into the METOC community; I will look forward to seeing each of you again out in the fleet.

Finally, I would like to thank Jen. Her loving support and patience made all of this possible. Through the good times or the stressful times, she was there to encourage me, and I am eternally grateful to have her with me.

THIS PAGE INTENTIONALLY LEFT BLANK

I.   INTRODUCTION

The oceans of the world are a major component in the earth's climate system. Covering over 70% of the earth's surface, oceans absorb a predominant amount of the sun's radiation reaching the planet, directly converting this radiation into heat energy. Direct ocean surface interaction with the atmosphere provides a further significant exchange of heat. The magnitude and spatial variation of heat transfer depends upon several processes, including surface wave magnitude and sea spray interactions, the presence of clouds, and precipitation from the atmosphere. In the ocean interior, on a global scale the process is primarily one of meridional transfer of heat from lower to higher latitudes. This transfer is possible because of the high specific heat capacity of sea-water. Thus, on a global scale, a significant amount of the heat that is absorbed near the equator can be advected away from its source region, and eventually released back into the relatively cooler atmosphere at higher latitudes. In the North Atlantic alone, the Atlantic Meridional Overturning Circulation (AMOC) transports over 10^{15} W of heat (Ganachaud and Wunsch 2000) poleward. This meridional heat transport provides an important stabilizing effect on the earth's climate system.

The global scale circulation described above is typically referred to as "Meridional Overturning Circulation," (MOC) and it is the primary focus of this study. While the MOC is a mechanism-neutral term, it does encompass several driving components, which are all subject of the ongoing research activities motivated by the increasing concern about global climate change. Much effort has been expended to describe the primary thermodynamic and mechanical forcing mechanisms that are responsible for driving the MOC. Its magnitude, stability, and sensitivity to these mechanisms are also of great interest. The air-sea heat flux has a direct impact on ocean circulation patterns: heat loss or gain affects the density of seawater, thereby fostering sinking or rising motions that must be accompanied by the lateral transfer of volume. Salinity exchanges act in a similar manner. Another driving mechanism is related to density diffusion, which is traditionally believed to play a significant role in interior abyssal circulation. The combination of these processes acting on the ocean is defined as

Thermohaline Circulation (see Figure 1).   While the classical theory emphasizes thermodynamic mechanisms of the maintenance of MOC, other oceanic processes can also exert the controlling influence on the overturning. For instance, winds and gravity driven internal tides and waves directly impart mechanical energy into the ocean. Therefore, understanding the relationships between each of these driving mechanisms is of particular importance in the attempt to gain insight into the interior processes from surface observations.   Success in this field could lead to a better prognosis of anthropogenic climate change.

SAMW	Subantarctic Mode Water
AAIW	Antarctic Intermediate Water
RSOW	Red Sea Overflow Water
AABW	Antarctic Bottom Water
NPDW	North Pacific Deep Water
AAC	Antarctic Circumpolar Current
CDW	Circumpolar Deep Water
NADW	North Atlantic Deep Water
UPPER IW	Upper Intermediate Water
IODW	Indian Ocean Deep Water
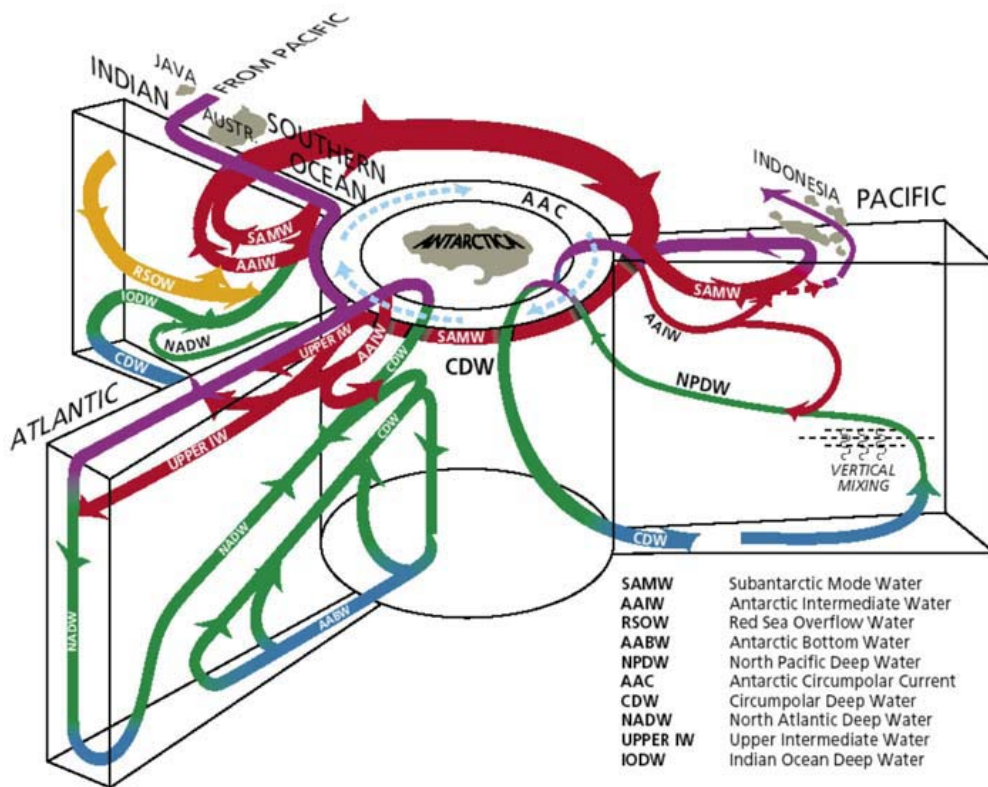
Figure 1.   Classical representation of the global thermohaline circulation and oceanic conveyer belt (From Aguado and Burt, Understanding Weather and Climate 2005).

2

II.   BACKGROUND

A.   CLASSICAL THEORY

Several of the leading classical theories governing global scale circulation stem from Sandstrom's (1916) pioneering work, where he described the ocean as a thermodynamic system that could not maintain circulation in the vertical plane if the forcing is limited to the air-sea buoyancy flux. His suggestion that buoyancy forcing had to be transmitted to the ocean interior by other processes led to the development of theories based upon vertical mixing as the primary mechanism for transmission of this signal. Among the most influential theories are Munk's advetive-diffusive balance (1966), Stommel's "Two-box model" (Stommel 1961), conceptual frameworks developed by Wyrtki (1961), and Stommel and Arons' (1960 a, b), all of which emphasized the interior modification of density in forcing the entire system (see Figure 2).
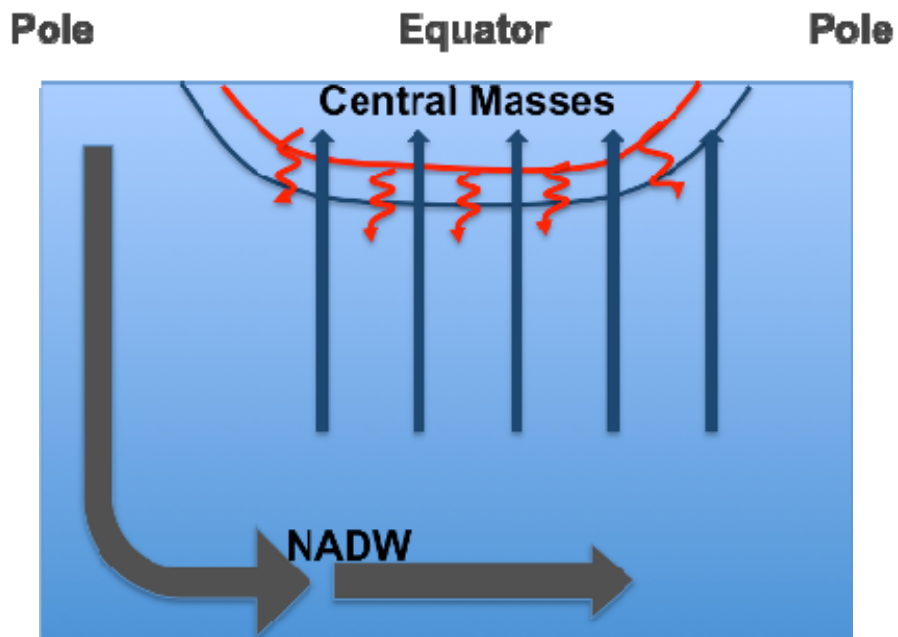
Figure 2.   Schematic of Munk's Advective-Diffusive Thermocline Theory: Heat from the warmer, stratified thermocline diffuses down into the abyssal depths where it balances deep-water upwelling.

By the early 1990s, several studies had been completed which questioned some of the assumptions behind the classical thermodynamic theories of the MOC. Principal among these studies were improved estimates of the diapycnal mixing in the ocean interior (e.g., Gregg 1989; Ledwell et al. 1993). These studies found that the level of vertical diffusivity in the central thermocline ($k_V \sim 10^{-5}$ m^2s^{-1}) was much less than the values ($5\text{-}10*10^{-5}m^2s^{-1}$) required by diffusive models to support a MOC of sufficient strength to match the ocean's true state (e.g., Bryan 1987). Toggweiler and Samuels (1993, 1995, 1998) reinforced this skepticism when they concluded, on the basis of radiocarbon sampling, that diapycnal mixing was insufficient to sustain the 15 Sverdrup (1 Sverdrup = 1 Sv= 10^6 m^3s^{-1}) MOC estimated in the Atlantic Ocean. More recently, a finding (De Boer et al. 2010) that the AMOC is not necessarily positively correlated with the Meridional Density Gradient (MDG) cast further doubt upon the primacy of the density-driven theories.

B.   RECENT ADVANCES

As a result of research activities over the past 25 years, the emphasis has shifted significantly from primarily diffusively driven models towards a more comprehensive conceptualization incorporating mechanical forcing mechanisms, as well as effects of geometry and the water-mass transformation in the upper mixed-layer. In this context, modern MOC theory (Webb and Suginohara 2001; Samelson 2004, 2009; Boccaletti et al. 2005; Radko 2007; among others) has come to identify two primary components of circulation—a shallow component residing in the main thermocline, and a deep circulation in the abyssal ocean. In the abyssal regions, shielded from the direct influence of wind, small-scale mixing processes are necessary to resupply potential energy removed from the interior by overturning and eddy-generating processes (Wunsch and Ferrari 2004). However, in the strongly stratified central thermocline, dynamics are controlled by the ventilation of water masses along the isopycnals that outcrop at the sea surface (Luyten et al. 1983)

4

Coincidental to this evolution, there has been an increased emphasis on near surface and thermocline dynamics and its associated mechanical (wind) forcing. Until recently, most theories ignored atmospheric wind stress as a major forcing mechanism, primarily due to classical theoretical emphasis on abyssal dynamics, but studies by Toggweiler and Samuels (1995, 1998) and Timmermann and Goosse (2004) highlighted the critical importance of wind stress in forcing the AMOC. Boccaletti et al. (2005) showed through modeling experiments using a "heatfunction" that surface circulation dominates the heat transport in global ocean models, making it likely that ocean heat fluxes will respond to changes in atmospheric winds rather than changes in abyssal mixing. Gnanadesikin et al. (2005) reinforced this finding via an analysis of the buoyancy transport and its role in the energetic of the MOC system.

In conjunction with the shift to "ventilated" wind-driven dynamics, another recently emerging area of study is the linkage between the AMOC strength and the geometric asymmetries between the Southern and Northern hemispheres. In this context, the Antarctic Circumpolar Current (ACC) emerged as a critical asymmetric feature requiring analysis. Two studies by Webb and Suginohara (2001a, 2001b) indicated the AMOC could be sustained in part by upwelling forced by the ACC and southern ocean winds. Only recently have consistent theoretical models been developed for the ACC. One of the primary difficulties in conceptualizing the role of the ACC involved connecting non-geostrophic circulation patterns in the ACC with geostrophic patterns existing in the interior of the Atlantic. However, development of analytical residual-mean theories by Marshall and Radko (2003), Radko (2005), and Olbers and Visbeck (2005) made it possible to link wind stress, geostrophic eddies, and surface buoyancy fluxes in a single framework and thus describe the ACC-MOC connection. Using this theory, Radko (2007) demonstrated that a pole-to-pole MOC could be sustained entirely as a result of positive feedback between wind input and temperature gradient. A critical assumption of residual-mean theory is that interior mixing below the mixed layer occurs along isopycnals, and the ability of this model to account for a significant fraction of the MOC further supports the importance of adiabatic processes in the ocean interior.
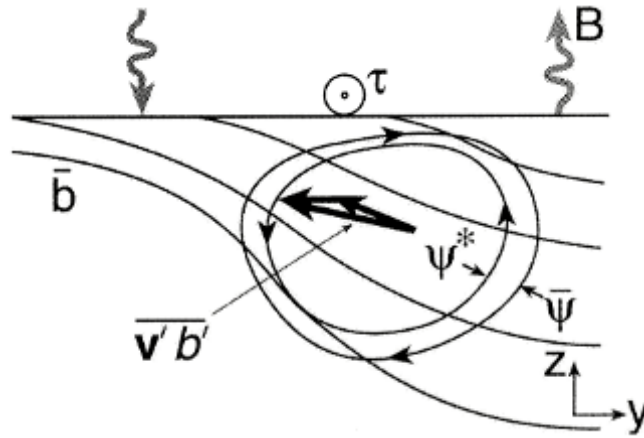
Figure 3.   Decomposition of the flow into Eulerian and Eddy components (From Marshall and Radko 2003)
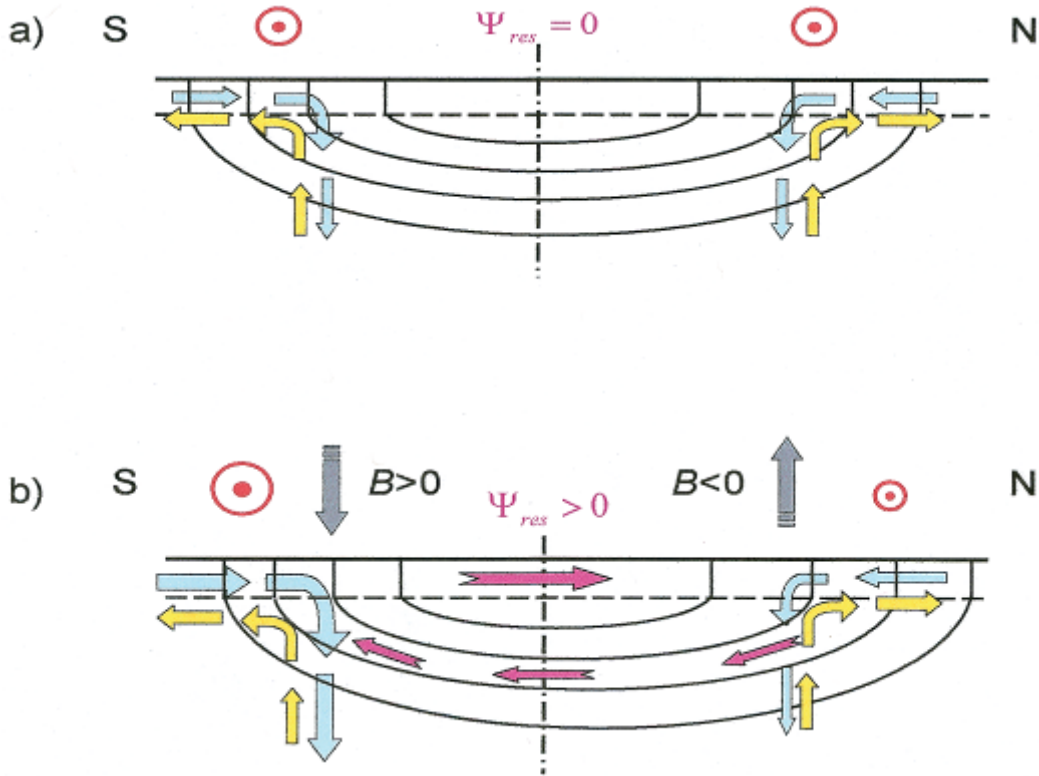
Figure 4.   Effects of the forcing asymmetries on the MOC. a.) Symmetric forcing conditions are assumed on each hemisphere. In such a situation the interhemispheric transport vanishes. b.) Dual-asymmetric forcing induces a net residual flow across hemispheres (From Radko 2007)

C. CONTRIBUTION OF THIS STUDY

In view of findings discussed in Section 1.B., the debate on the relative importance of surface driven adiabatic advection versus diabatic interior mixing in forcing the MOC has shifted recently to favor the adiabatic argument. On a quantitative level, both processes are important in controlling the MOC structure and stability. Questions remain as to the specific pathways in which heat and energy are transported into the ocean interior. Numerical modeling appears to be the obvious and most convenient approach to address these issues. However, all numerical models utilize parameterizations of sub-grid processes, introducing significant uncertainty into the analysis of the vertical structure of the MOC. While global characteristics of the oceanic overturning can be estimated from air-sea fluxes (Trenberth and Caron 2001), the detailed physical description remains elusive.

Nonetheless, attempts have been made to analyze vertical structure. A conspicuously successful approach was developed by Walin (1982), who related integrated rates of water mass transformation at isopycnal surfaces to the air-sea buoyancy fluxes. Since water mass transformation at a given buoyancy surface is linked to diapycnal volume flux (Tziperman 1986), it became possible to evaluate diapycnal transport from sea surface data. Isopycnal/adiabatic, pole-to-pole diagnostics posed a more challenging problem since isopycnal flux is not directly linked to integral measures of density forcing at the surface. However, with the application of residual mean theory, Radko, Kamenkovich, and Dare (hereafter referred to as RKD 2008) were able to expand on Walin's method by connecting the MOC strength to the difference in subduction rates—processes controlled by sea surface density flux—at the northern and southern outcrops of each density layer. Their analysis of European Centre for Medium-Range Weather Forecasts (ECMWF) and Levitus climatology surface data, yielded results consistent with circulation patterns and magnitudes observed in their general circulation model (GCM) runs, and with previous estimates of MOC overturning.

In light of these recent findings, this paper will analyze the sensitivity of the MOC to the pattern and magnitude of the surface density/heat flux, with the goal of answering three questions:

1. What processes provide the dominant driving mechanisms for the MOC? Are the dominant processes adiabatic or diabatic in nature?
2. Can we predict (at least qualitatively) the structure and magnitude of the MOC, based only upon surface and atmospheric observations?
3. How does the MOC structure and magnitude change when surface forcing patterns are changed spatially? Do changes in the surface forcing in certain regions affect the MOC structure and magnitude more than other regions?

These three questions are inextricably linked; only in a case where adiabatic processes are dominant can we hope to obtain interior characteristics without extensive in-situ measurements. Only in a case where adiabatic processes are dominant is the MOC structure directly related to surface forcing patterns.

The analysis will be presented in the context of diagnostics based on idealized ocean model runs. In Chapter III, methodology, assumptions, and preliminary calculations are set up. In Chapter IV, the response of the MOC to isolated heating sources distributed at different spatial locations is described. Discussion and final conclusions are given in Chapter V. Finally, some suggestions for further research will be given in Chapter VI.

III. METHODOLOGY

This study is based on a set of idealized numerical simulations. The chosen setup is representative of the process-oriented modeling of intermediate complexity, which is used to study the influence of the air-sea heat fluxes on the strength of the MOC. Of particular concern is the spatial variation in the distribution of heat fluxes. Thus in subsection (A) the experimental framework for this study is described, while elements of the RKD formulation used in this study are described in subsection (B). The complete RKD formulation can be found in RKD (2008) or in the NPS Thesis written by Dare (2006).

A. EXPERIMENTAL SET-UP

1. The General Circulation Model

For this study, the Massachusetts Institute of Technology General Circulation Model (MITgcm) was employed. The MITgcm is a numerical model designed for the study of the atmosphere, ocean, and climate. It can be used to model both atmospheric and oceanic circulation and has non-hydrostatic capability which allows it to be used to study both small and large- scale processes. It uses the finite volume method to solve oceanographic equations, providing support for the treatment of irregular geometries using orthogonal curvilinear grids and shaved cells. Tangent linear and adjoint code are maintained alongside the forward model, permitting sensitivity and optimization studies. MITgcm supports a wide variety of physical parameterizations and was developed to perform efficiently on a wide variety of platforms. For more information about MITgcm, visit http://mitgcm.org.

2. Configuration of Experiments

For the purpose of this study, two sets of experiments were run using the MITgcm. Both sets were initiated off of a single 1000-year control run to equilibrate the ocean circulation system. The computational domain was represented by an idealized

single basin bowl shaped geometry utilizing a Cartesian coordinate system. The model runs were integrated forward at 20-minute intervals. In each of the model runs, the basin spanned 6660 km zonally and 13,320 km meridionally, with the intent of simulating circulation on a scale consistent with the Atlantic Ocean. For all experiment sets we employed a model resolution of 133.2 km in both axes, and 20 vertical levels. Vertical resolution was varied exponentially from 22 m at the surface to 678 m at the deepest level, thus capturing the thermocline in greater detail.

Zonal surface wind stress was directly input, utilizing forcing patterns that were generated using a sinusoidal curve to represent the meridional profile. For all model runs in this study, the wind forcing profile was symmetric about the equator and is given by the expression $\tau = 0.075 \times \sin(3\pi y / 99) + 0.075 \times \sin(5\pi y / 99) \, \text{N/m}^2$. Meanwhile, the baseline thermodynamic forcing involved relaxation of the SST to the target temperature profile that was also symmetric about the equator. The expression for the target temperature profile is given by $Q_{profile} = 2.5 + 12\sin(\pi y / 99) \, ^\circ\text{C}$, and the relaxation time was set to 60 days (see Figure 5). This thermodynamic profile forcing was utilized for the initializing model run. However, for the experiment runs heat fluxes were generated using two different configurations, as will be described below.
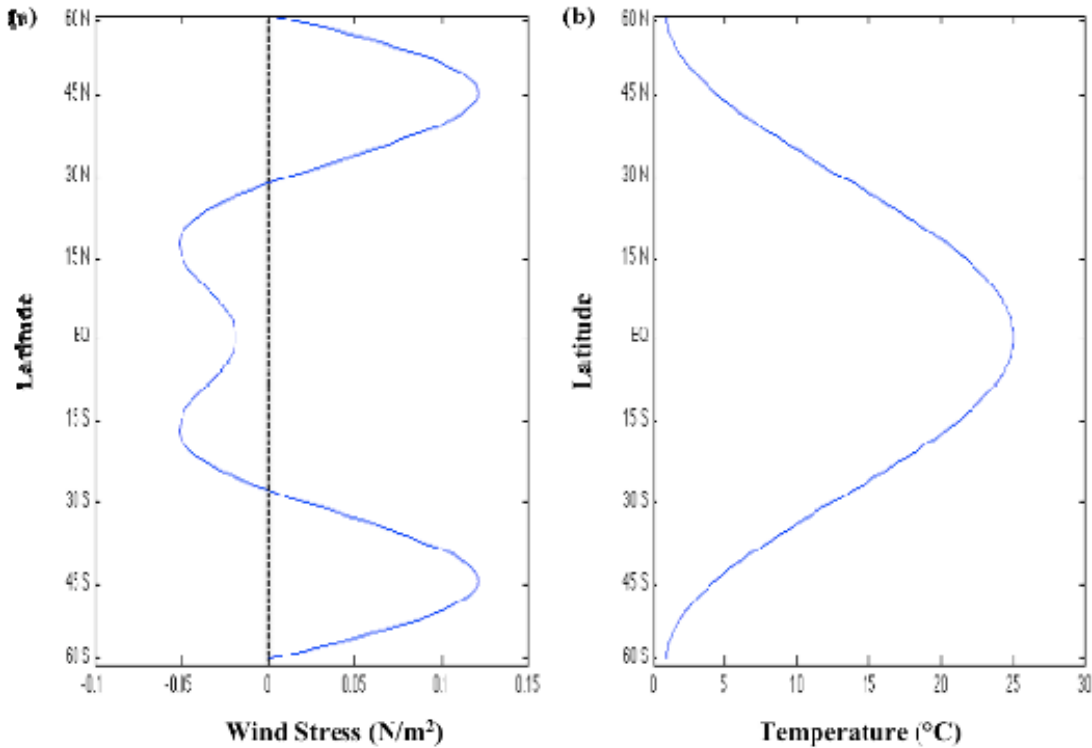
Figure 5.   (a) Winds Stress and (b) SST forcing profiles input into the model runs.

a.   Configuration 1

In the first set of experiments, 12 runs were integrated forward 500 years from the 1000-year checkpoint. In each of the 12 runs, the temperature-forcing pattern was modified by adding a heating source within the circular area of 600km in diameter. The heating source was placed in a different location for each model run (see Figure 6). Within grid elements defined by the location of the heating source, the target SSTs were adjusted 2 degrees Celsius higher than the symmetric norm, implicitly modeling a stronger heat flux into the region. In addition, the Gent-McWilliams parameterization to represent the effect of mesoscale eddies on isopycnals (Gent and McWilliams 1990) was employed and the vertical mixing coefficient was tuned down an order of magnitude to better simulate an adiabatic state.

11
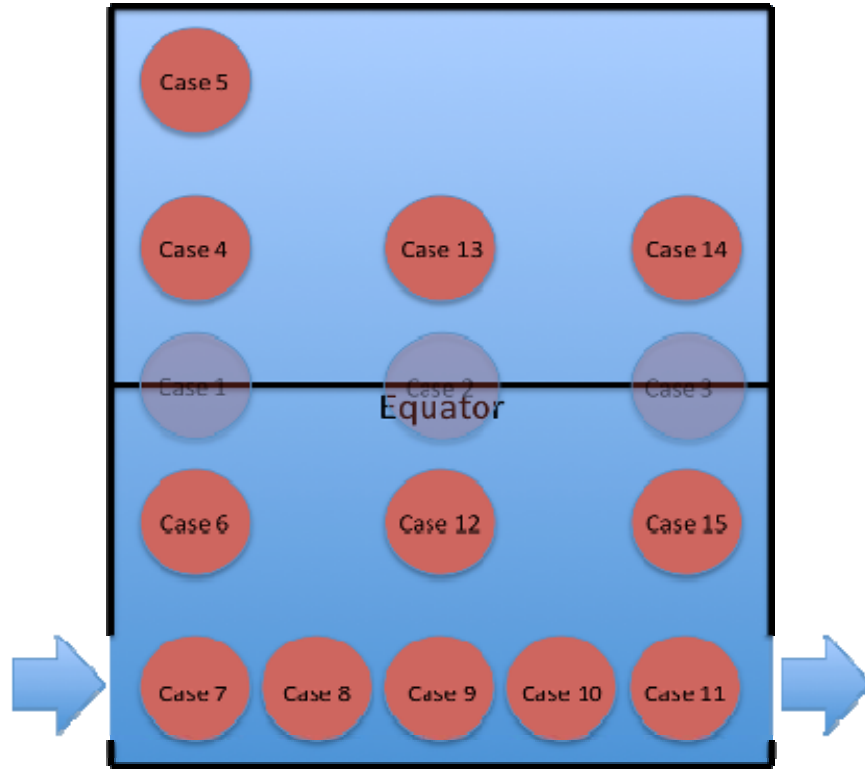
Figure 6.   Schematic representation of the heating sources for each experiment run
(labeled by case #). For Configuration 1, the sources were adjusted +2 °C from
the mean profile, while for Configuration 2 the sources represent the area where a
heat flux of 50 W/m^2 was directly applied

b.   *Configuration 2*

In the second configuration set, the basic state was first integrated forward
another 500 years in an environment of complete insulation. Surface heat fluxes were
input directly and were set to zero across the entire surface. Again, the Gent-McWilliams
parameterization was employed at this point and the vertical mixing coefficient was
reduced by an order of magnitude. After 500 years a set of 12 runs was integrated
forward from this state for another 500 years. During this integration period, surface heat
forcing was introduced directly, with heating sources placed in the same locations as
described for Configuration 1 (see Figure 6). The heating source imparted a downward

(heat gain) flux of 50 W/m^2, while the rest of the ocean surface was set to an upward (heat loss) flux of approximately 0.2 W/m^2 in order to maintain a zero net heat gain or loss over the entire ocean surface.

c.   Numerical Parameters

A list of numerical parameters for the experiment sets is given in (Table 1). These parameters are consistent with previous general circulation modeling studies, with the exception that when the Gent-McWilliams parameterizations were employed beginning at the 1000-year mark, the vertical mixing coefficient was reduced significantly. The intent behind this change was to bring the model closer to an adiabatic state and thereby test the model derived MOC values against the calculations based on the Walin-RKD formulation. Furthermore, for the SST forced runs in configuration 1, the model derived MOC values could be broadly related to current estimates of the Atlantic MOC magnitude. If, despite the reduction in vertical mixing values, realistic MOC values could be obtained through this experiment it would provide further justification for the adiabatic view of the MOC.

Table 1.   Numerical parameters for experimental runs

Parameter(s)	Value(s)
Basin width, length	6926.4 km, 13320 km (approx. 60° by 120°)
Basin depth	4005 m
Horizontal, vertical diffusivity	2×10^3 m^2 s^{-1}, 5×10^{-6} m^2 s^{-1} (5×10^{-5} m^2 s^{-1} in the initialization for all experiments)
Horizontal, vertical viscosity	5×10^4 m^2 s^{-1}, 5×10^{-5} m^2 s^{-1}
Longitude and latitude grid spacing	133.2 km (approx. 1.2°)
Number of vertical levels, grid spacing	20 levels varied exponentially from 22 to 678 m
Temperature restoring timescale	60 days
Time step, momentum	20 min
Time step, tracers	20 min

d.   *Diagnostics*

Once data from each experimental run was obtained, the model output was further analyzed utilizing MATLAB. The first diagnostics applied to all runs was a calculation of the inter-hemispheric transport, which was defined as an integral, over the equatorial plane, of the northward (positive) and southward (negative) volume flux components:

$$MOC(N) = \sum_{i=1}^{x_{max}} \sum_{k=4}^{z_{max}} V_{ik}^{(+)} \cdot dz_k \cdot dx \tag{1}$$

$$MOC(S) = \sum_{i=1}^{x_{max}} \sum_{k=4}^{z_{max}} V_{ik}^{(-)} \cdot dz_k \cdot dx \tag{2}$$

where $V_{ik}^{(+)}$ and $V_{ik}^{(-)}$ represent the individual grid meridional velocity components (m/s), dz_k represents the kth layer thickness, and dx is a constant x grid spacing of 133.2 km. The summations did not include the first three data levels (k=1...3) in order to exclude from consideration Ekman transport in the upper mixed layer.

The second calculation also involved evaluating the MOC at the equator, but this time as a function of density.   This was achieved by integrating all flux components through the x-z plane that lied below an incrementally decreasing density contour line (see Figure 7). In order to take smaller intervals of density contour lines, the gridded 51x20 data fields (the westernmost grid-point was not calculated) were linearly interpolated onto a 5101x2000 mesh. Then the interpolated values were summed (for each x grid point (i)) from the model floor up to the maximum value of *z* not exceeding the specified σ contour value at x grid-point (i),

$$MOC(\sigma) = \sum_{i=2}^{x_{max}} \sum_{k=z_{\sigma c}(i)}^{z_{max}(i)} V_{ik} \cdot dz_k \cdot dx \tag{3}$$

providing a net volume flux value as a function of σ .

14
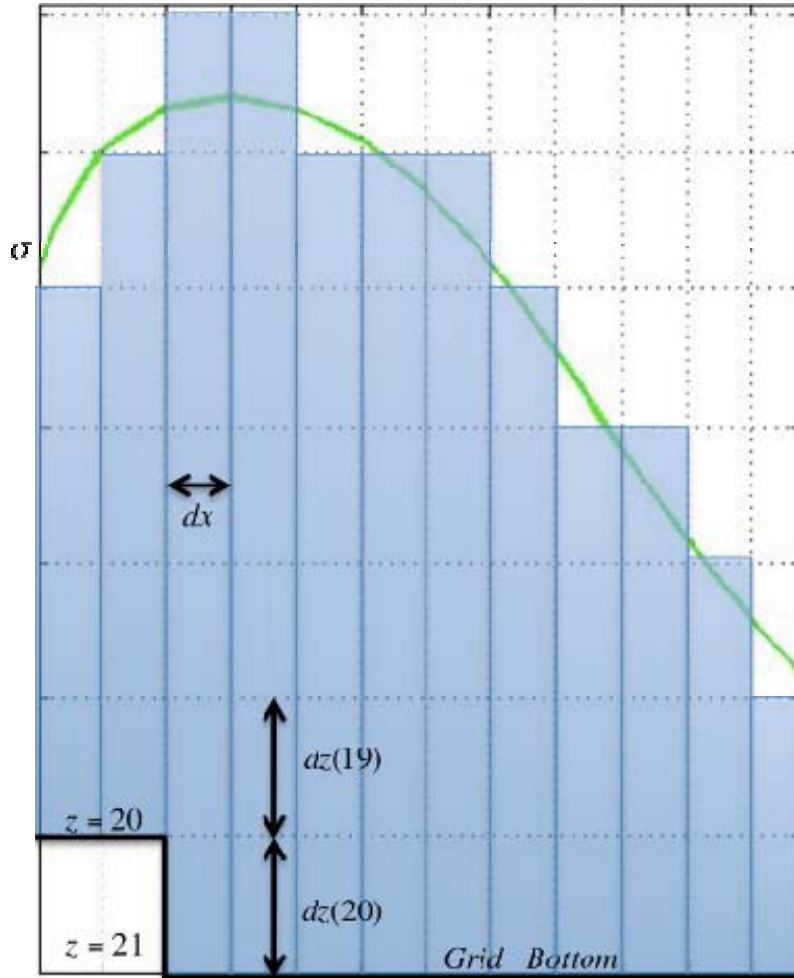
Figure 7.   Schematic of the Equatorial MOC calculation as a function of density.
Shaded area indicates regions that are summed to form $MOC(\sigma)$

The third diagnostic involves an application of the water-mass transformation theory (Walin 1982) to the model output. The surface density flux is analyzed to compute the water-mass transformation function $F(\sigma)$ defined by Equation (21) (see Appendix).   The underlying concept behind this diagnostic is relatively simple. By evaluating surface density flux as well as the geometry in which the mixed-layer density is changing, and then comparing these integrated values along two different isopycnals, RKD (2007) showed that the difference between the two values should be approximately equivalent to the rate of subduction from (to) the mixed-layer into (out of)

15

the ocean interior. For this study, a critical assumption is that one of the boundaries represents a density value "just above" the highest density value in the ocean, thus making the integrated value $F(\varepsilon)$ equal to zero.

The purpose of these diagnostics is two-fold. First, a direct comparison can be made between Walin-inferred volume flux and the actual inter-hemispheric transport. This comparison will provide evidence that a signal input at the mixed-layer is seen in the interior of the ocean (see Figure 8). The second objective is to quantify the change in the MOC magnitude in response to the variation in the air-sea heat flux. This quantity will be referred to hereafter as the "sensitivity value," which is defined as follows:

$$\gamma = \frac{\Delta MOC}{\Delta Q} \tag{4}$$

where ΔMOC represents a difference in the inter-hemispheric transport between the basic and perturbed simulations and ΔQ is defined as:

$$\Delta Q = (Q_N - Q_S) - (Q_{N_{control}} - Q_{S_{control}}) \tag{5}$$

In other words, ΔQ represents a difference between the hemispheric heating asymmetries in the control and configuration runs. The latter diagnostics is applied to all configuration 2 experiments in an attempt to identify locations that are most (least) effective in driving the MOC.
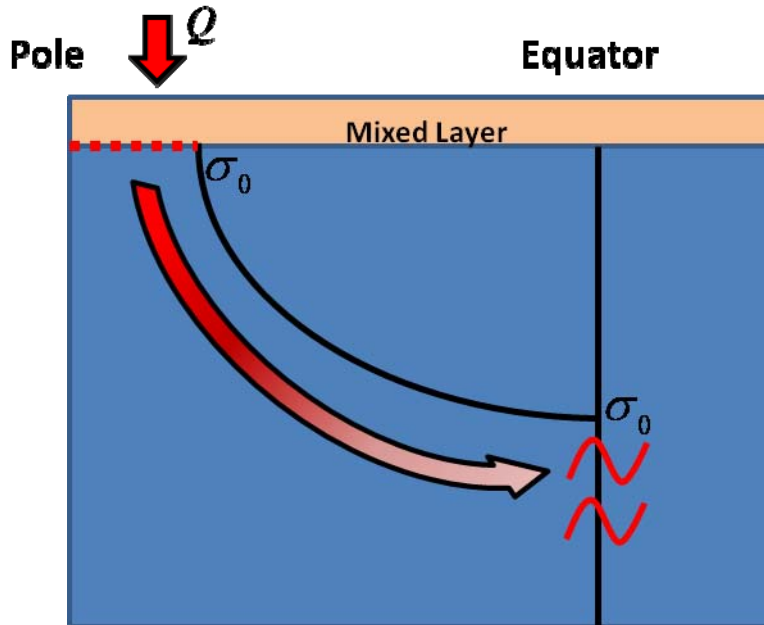
Figure 8.   Schematic of the theory-based analysis. In the predominantly adiabatic ocean the Walin-inferred flux across the bottom of the mixed layer (red dashed line) will closely match volume flux across the Equator (red curves) for each value of Sigma

e.   Pathways of Heat Transport

In conjunction with the analysis of the MOC signal in terms of the affected density range, it is desirable to examine the actual spatial patterns of heat transport from sea-surface into the ocean interior. Since one of the primary goals of this study is to model adiabatic processes, we focus our inquiry on the individual isopycnal surfaces and examine the temperature variation associated with heat input at different surface locations (Figure 6).   Thus observations of the pattern in which temperature deviates from the control run will be discussed in the context of Walin-inferred and actual volume flux calculations. The diagnostic was applied to the configuration 1 model runs.

To accomplish the surface analysis, at the end of the 1000 year control run, a surface of constant temperature was selected for analysis. The surface was created through a linear interpolation of the grid, and was chosen to approximately represent the bottom of the upper thermocline. For this study, the interpolation was referenced to a temperature of 8.5 °C. Figure 9 shows a three-dimensional view of this surface.
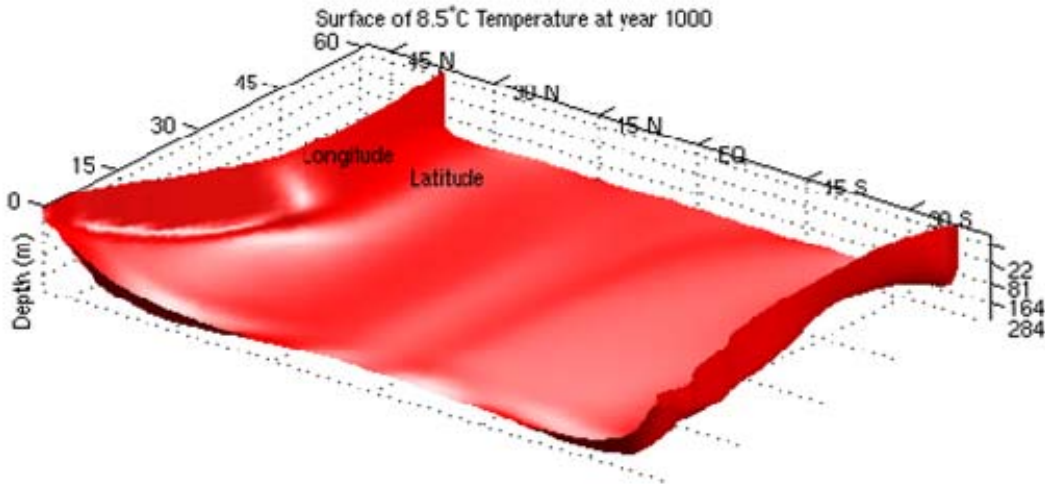
Figure 9.   The control surface of temperature 8.5 °C.

Once this surface was created, data from the surrounding grid points in both the forward integrated control run and the configuration run were interpolated onto this surface. The sets of control point values were then subtracted from the related sets of configuration run values to yield a difference value at each surface point. These values were then mapped onto a 2-D surface for ease of viewing (see Figure 10).
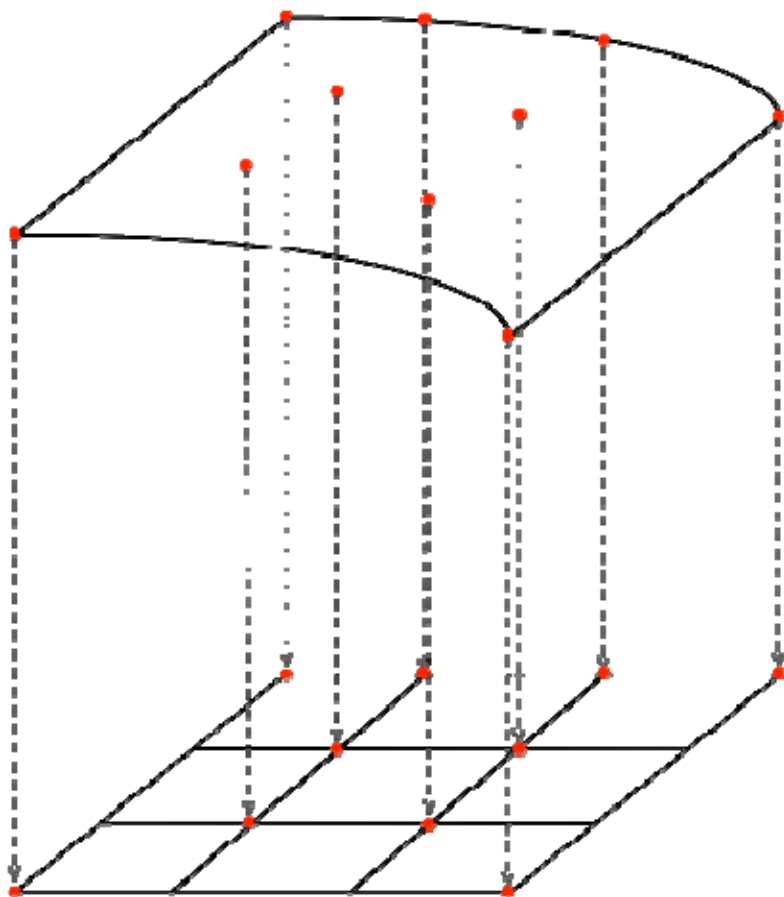
Figure 10.   Depiction of the 3-D surface mappimg onto a 2-D plane.

19

THIS PAGE INTENTIONALLY LEFT BLANK

IV.   RESULTS

A.   MODEL OUTPUT

Data fields for each model run were recorded at yearly intervals. A visual inspection of these outputs shows the SST profile forced model captures many features seen in nature. Figures 11 and 12 give a snapshot of the control SST forced model run at 500 years (1500 years total time). Figure 11 shows the top layer currents, from which the Western Boundary Currents (WBC), Equatorial Counter-Current, ACC, and gyre circulations can clearly be seen. Figure 12a shows the snapshot SST field, which clearly indicates the transport of heat from the warmer Equatorial regions into the mid-latitudes via the WBCs. Figure 12b shows a cross-sectional temperature profile taken at the Equator. The thermocline depth presented in this figure can be clearly seen as decreasing from West to East, consistent with observations of the Atlantic stratification. One difference to note is that the depth of the thermocline shown in Figure 10b is shallower at all points than what is observed in the world oceans. This is due to the effect of the vertical diffusivity being reduced to a minimum in all runs.
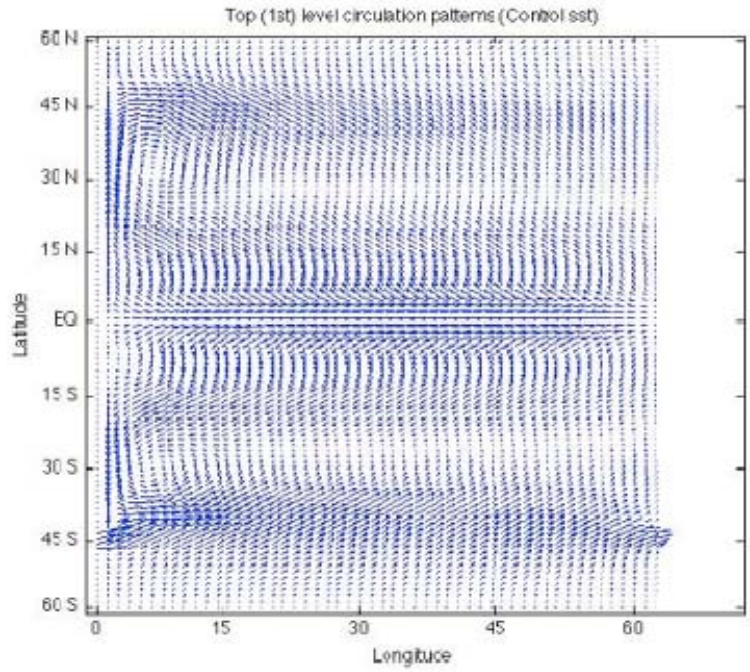
Figure 11.   Surface layer currents from the SST forced Control run.
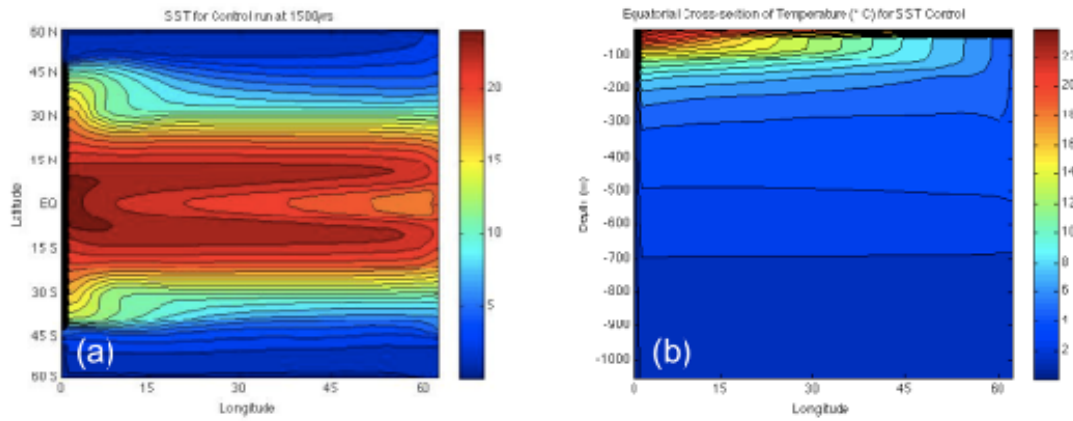
Figure 12.   Temperature fields in the SST forced control run at 500 years (a) SST pattern
at 500 years (b) Zonal section of temperature at the Equator.

B.   STREAMFUNCTION ANALYSIS

1.   Configuration 1: SST Forcing

To be precise in the detection of subtle effects associated with the localized changes in the heating pattern all results for the SST forced runs were compared against the control run, which was identical to the Configuration 1 runs in all respects, except for the presence of the localized heat source. Figure 13 gives the streamfunction profile for the control run, while Figure 14 shows the integrated volume transport as a function of density anomaly. While there was little relative change in the overall structure of the MOC from case to case, signals indicating slight changes in the MOC structure could be detected when comparing the Configuration 1 runs against the control experiment.
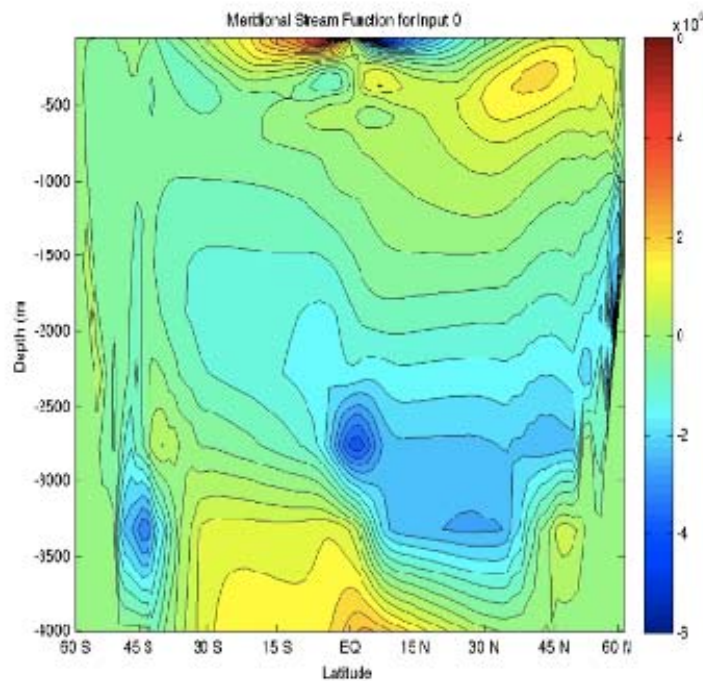
Figure 13.   Streamfunction for the Control SST forced model run. All model runs in the Configuration 1 set produced streamfunctions nearly identical to the Control.
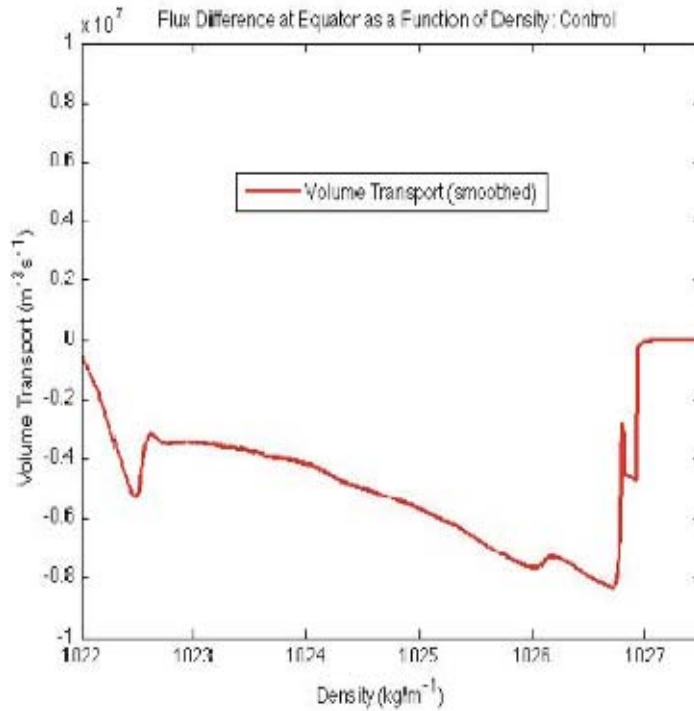
Figure 14.   Volume transport as a function of density (integrated upward from the ocean bottom)

2.   Configuration 2: Heat Flux Forcing

Figures 15 through 17 show zonally integrated volume streamfunction plots for six cases of experiment two (2). Figure 15 shows a comparison between the northern (15a) and the southern mid-latitude WBC (15b) heating sources. General heating patterns are nearly symmetrically opposite—for both cases the most notable density outcropping regions are poleward of the heating source, and the strongest circulations are within the upper 1000m and symmetrically opposite. However, there are a couple of interesting exceptions: most notably, there is a northward circulation branch at depth (1500–2500m) that exists in both cases. While the circulation is weaker in case 4 (Figure 15a), it still exists, contributing to about a 1 Sv difference in MOC magnitudes between the northern and southern heating cases. Secondly, the effect of the ACC is clearly evident, acting as a barrier to return flow in both cases, and shifting the overall circulation pattern northward.

24
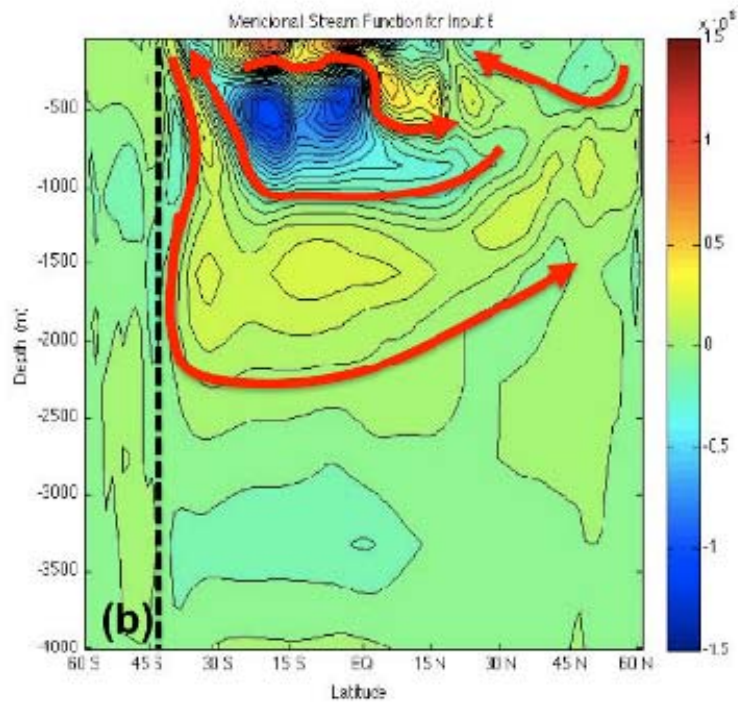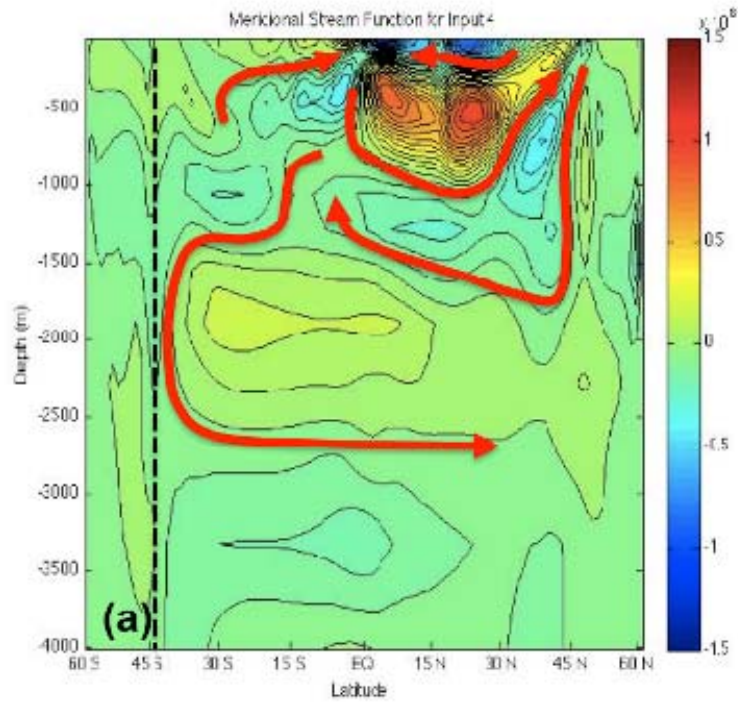
Figure 15.   Streamfunction plots for (a) case 4 and (b) case 6. Positive (yellow-red) values indicate counter-clockwise rotation. Note the influence of the ACC induced barrier (dashed lines) on the overall flow field
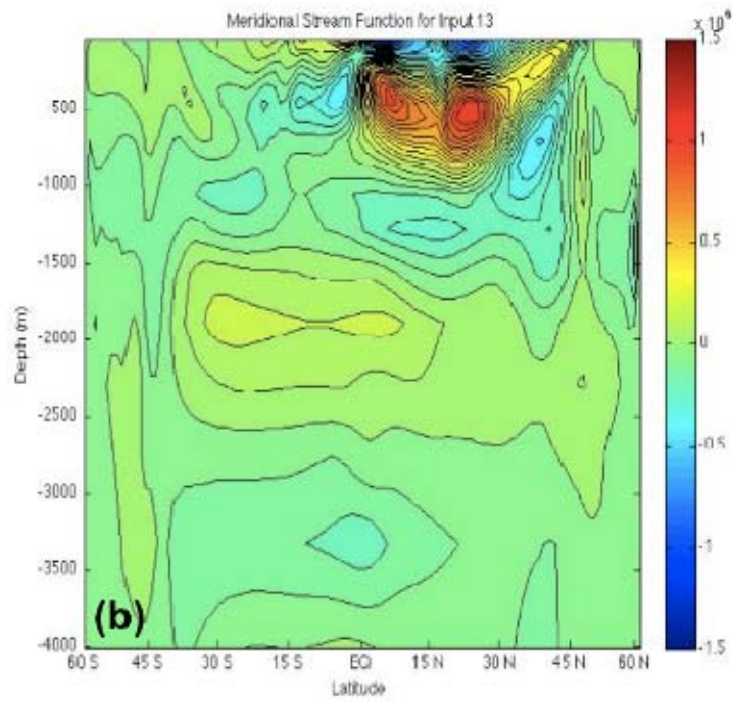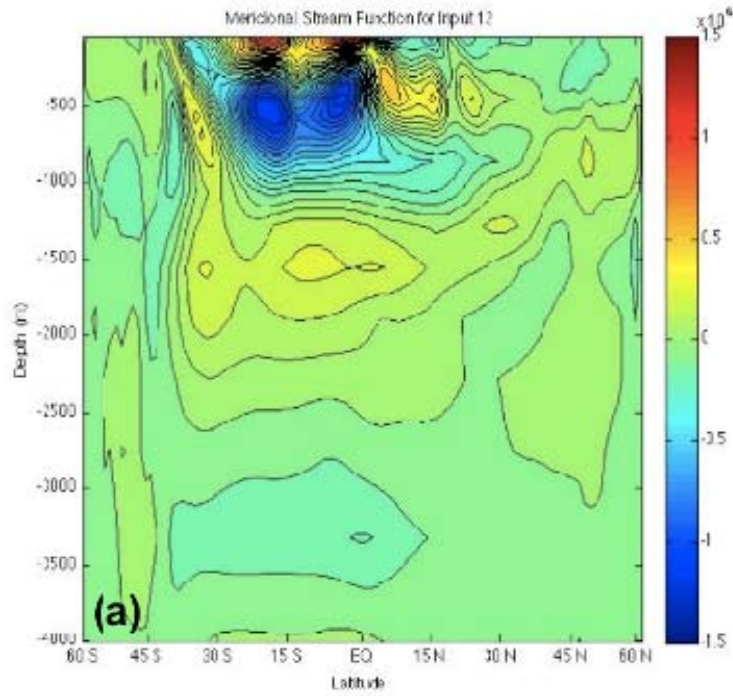
Figure 16.   Streamfunction plots for (a) case 12 and (b) case 13, representing 50W perturbations of the mid-latitude gyres
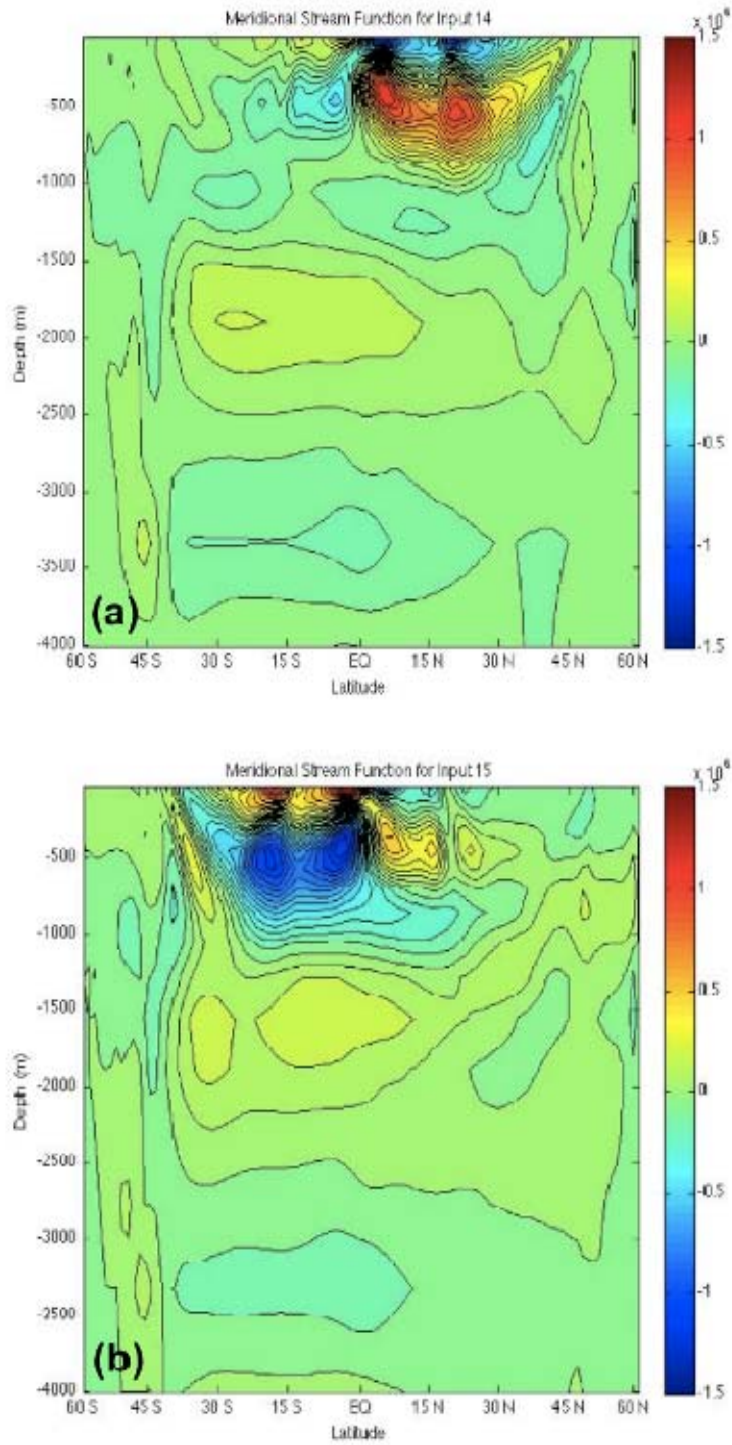
Figure 17.　Streamfunction plots for (a) case 14 and (b) case 14, representing 50W perturbations of the EBCs

Figure 16 shows a comparison between the northern (16a) and southern (16b) gyre heating sources, and Figure 17 shows the comparison between the northern (17a) and southern (17b) EBC heating sources. The patterns for the mid-latitude gyres and Eastern Boundary Currents (EBC), presented in Figures 17a and 17b are almost identical to those of cases 4 and 6. Figures 15, 16, and 17 show that in most of the 50W case runs there seems to be little variation in the MOC response to zonal shifting of heating perturbations. However, there is an exception to this general trend in the ACC perturbations. Figure 18 shows a comparison between cases 7 and 10, representing perturbations in the western ACC and the east-central ACC, respectively. While the patterns of circulation are very similar, case 10 (Figure 18b) exhibits a noticeable increase in strength in the two main overturning cells beneath of the equator and the northern mid-latitudes.
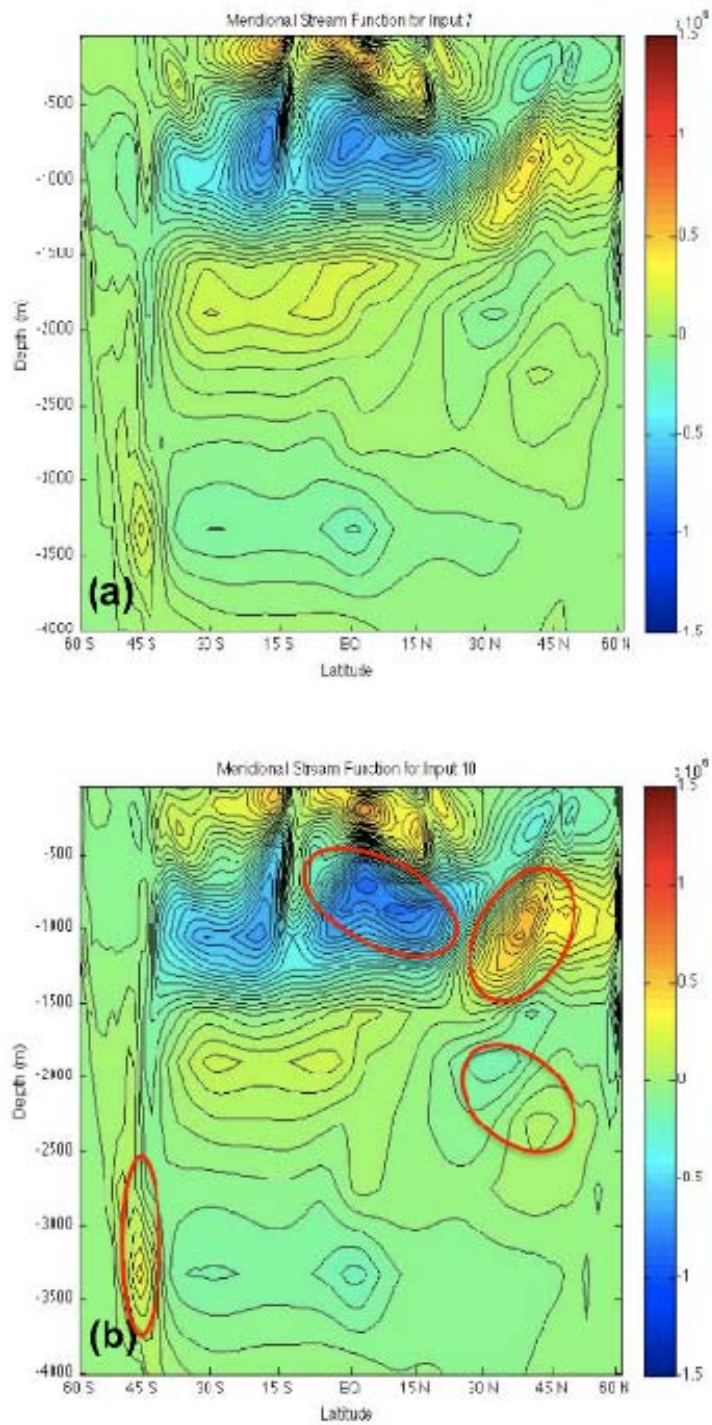
Figure 18.   Streamfunction plots for (a) case 7 and (b) case 10, representing 50W perturbations of the ACC in the west and east, respectively. Note the slight increase in circulation magnitude in the circled areas of case 10

C.   COMPARISONS OF THE INTER-HEMISPHERIC TRANSPORT AND WALIN-BASED INFERRED CIRCULATION

1.   Equatorial Volume Transport Calculations

In this section, the calculation of the integrated volume transport across the equator is compared against an inferred adiabatic MOC calculation based on the Walin/RKD method. Figure 19 provides an interpretation of the equatorial transport in the run number 4 of the Configuration 2 set. In this figure, positive transport regions (into the northern hemisphere) are represented by upward pointing arrows, while downward pointing arrows represent negative transport regions (into the southern hemisphere). Hence, in Figure 19 while the maximum net transport represented by the peak of the curve is about 2.3 Sverdrups, the actual MOC value is represented by the change in value from a minimum occurring near 1026 kg/m^3 to the peak—a value of about 2.6 Sv. A region of minimal exchange occurs wherever the slope of the curve is near zero. This interpretation applies to all of the integrated volume transport curves shown in this study.
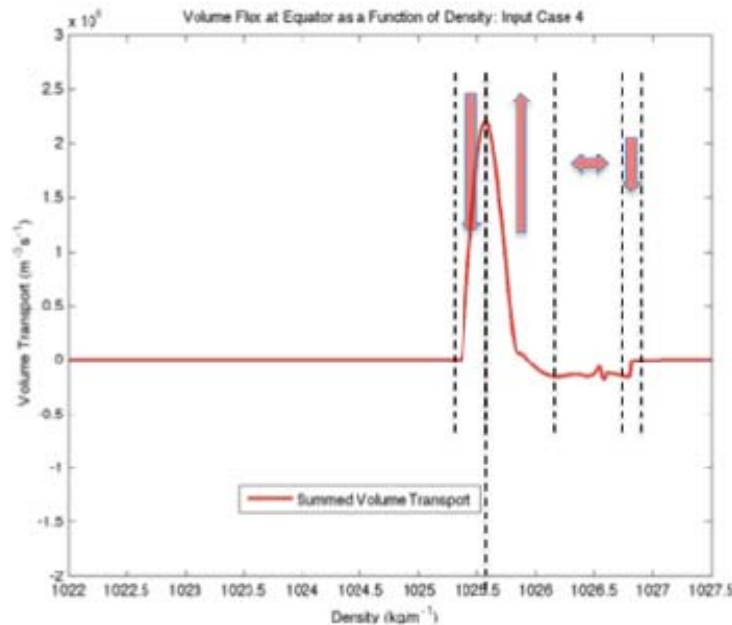
Figure 19.   Actual inter-hemispheric volume flux and interpretation

2. Configuration 1: SST Forcing

Figures 20 through 24 show comparisons between inter-hemispheric transport and the Walin-based inferred MOC calculations for the SST forced model runs. These figures present variation in the inferred (Walin-based) MOC relative to the control run. The differences are small, but in most cases the signal can be detected and correlated with the actual inter-hemispheric transport. Most cases exhibit a further order of magnitude difference between the Walin-based calculations (larger values) and the measured volume flux at the Equator (smaller values), which is attributed to the attenuation of the signal on its way from the outcrop to the equator by the diabatic processes. Only in the ACC case runs are the magnitudes between the two calculated values similar. As in the 50W direct heat perturbation runs (Configuration 2), the ACC runs register responses that are somewhat unique from the other runs and so cases 7 through 11 are grouped into Figure 21 for ease of analysis.

a. WBC Dynamics

Unlike the ACC runs, the model circulation system did not appear show a coherent response to WBC perturbations. Figure 20 shows the Equatorial integrated volume flux for case 6 (southern WBC perturbation). There does not appear to be a signal response of any consequence for this case or for cases 4 and 5 (northern WBC perturbations). The spikiness of the signal in the lower density levels more than likely represents noise. It should be noted that all of the SST profile forced runs exhibit the same levels of noise in the lower density ranges. Since the thickness of each level (Δz) increases exponentially with depth, it is likely that this noise is a result of the linear interpolation of the original data grid onto a smaller grid scale, combined with the small scale of the signal difference values (hence why it does not show up for the 50W runs).
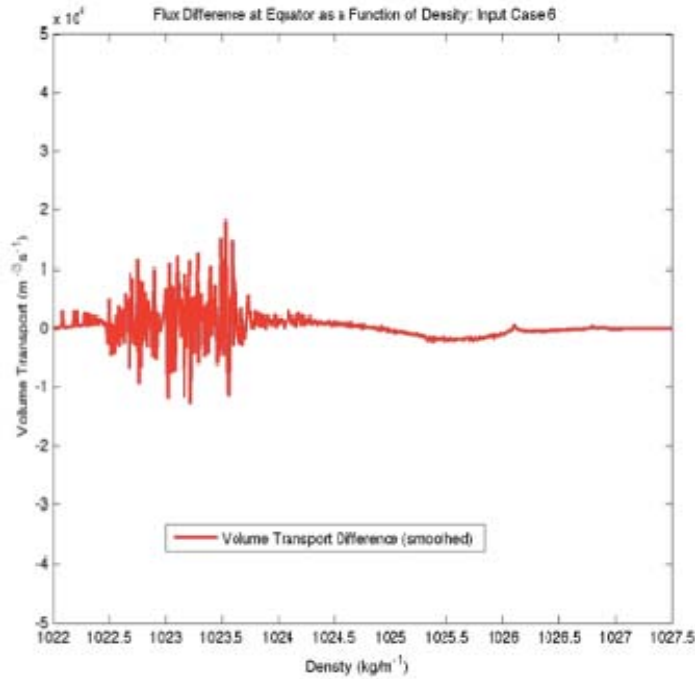
Figure 20.   SST forced run (case 6): an example where no obvious signal response occurs.

b.   *ACC Dynamics*

Figure 21 shows the response of the actual inter-hemispheric transport to each of the ACC perturbations (Figure 21a: cases 7–11) and compares it with the Walin-based inferred calculation (Figure 21b). The overall equatorial signatures for each of the ACC perturbations are very consistent, all showing a skewing of the distribution to the 1026 to 1027 kg/m^3 density range, where the largest variations occur.   Like the Configuration 2 runs, the magnitudes generally increase with more eastward placement of the SST perturbation.   While the Walin-based calculation seems to capture the general trend of the signal response to this movement, correlation is rather weak.   One signal however, does seem to be captured by the Walin calculation, a spike occurring at density 1026.12 kg/m^3 (circled).   The spike also increases in magnitude with more eastward placement of the SST perturbation, and is clearly present in both calculations.

32
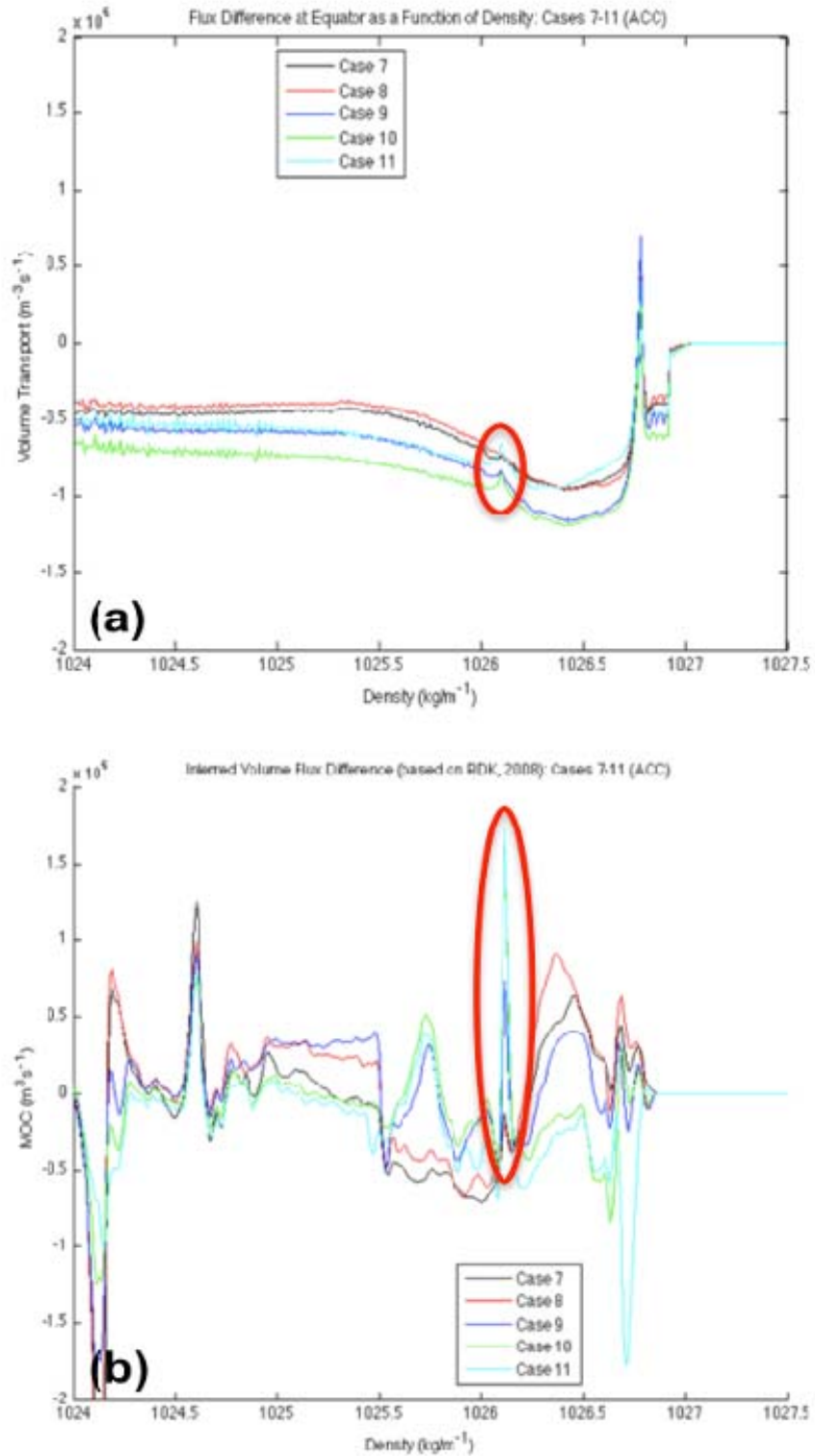
Figure 21. (a) Equatorial volume flux and (b) Walin-RDK inferred volume transport for
ACC cases 7 through 11. Walin inferred curves are smoothed.

c.   *Gyre and EBC Comparisons*

For case runs 12 through 15, the Walin-based calculation appears to pickup the general structure of circulation at depth, but not many of the finer details. In all four cases, there is a pattern in the density range 1026.05 to 1026.15 that both calculations corroborate well, though the Walin-based values are an order of magnitude larger than the observed Equatorial values. Another trait that seems to appear in each of the gyre and EBC cases is the shift of the MOC perturbation in the density classes between the equatorial calculations and the Walin based calculations. A potential explanation for this shifting is diabatic transformation of waters, but considering the inability of the Walin-based calculations to adequately describe finer features of the circulation pattern, this explanation must be taken with caution. In two of the case runs (12 and 14) the main distribution minima appear to be aligned.

Figures 22–24 compare SST forced cases 12, 14, and 15. Curves and dotted lines were placed in certain regions of the distributions to highlight potential areas of correlation produced by the two methods.

Figure 22.   (a) Equatorial volume flux and (b) Walin-RDK inferred adiabatic volume transport for southern gyre case 12.

Figure 23.   (a) Equatorial volume flux and (b) Walin-RDK inferred adiabatic volume transport for northern EBC case 14.

Figure 24.   (a) Equatorial volume flux and (b) Walin-RDK inferred adiabatic volume
transport for southern EBC case 15.

3. Configuration 2: Heat Flux Forcing

Figures 25 through 31 compare the actual Equatorial volume flux with the Walin-based inferred MOC calculations for the model runs in configuration 2. Several interesting features are revealed by these runs. First, in every case, there exists a positive correlation (i.e. the distributions are oriented in the same direction) between Walin-based inferred MOC calculation and the Equatorial volume flux. Second, for all the WBC and gyre perturbed model runs, the density distributions are almost exactly aligned. In the cases (7–11, and 15) where the density distributions do not line up, the offset is relatively small and the overall shape of the distributions bear a close resemblance.

Since the ACC perturbed distributions exhibit several unique characteristics, they are placed together in a single figure (Figure 27) for easy comparison. For all of the ACC case runs, a 0.25 to 0.30 kg/m^3 density offset can be clearly seen. Another feature of interest is the slight shift in the density level of the maximum integrated southern transport between the ACC case runs. The level of maximum integrated volume transport shifts to slightly denser waters as the heating perturbation shifts from west to east in the ACC. The shift in the perturbation field to the east also produces a slight increase in the maximum integrated volume transport value as seen in Figure 27a. Figure 27b shows that the Walin inferred calculation captures both the density and magnitude shifts for case runs 7 through 9. It continues to capture the density shift through case 11. However, it does not capture the magnitude shift in cases 10 and 11.

Figures 28 through 31, representing case runs 12–15, clearly reveal the asymmetry discussed in the streamfunction analysis. There is good correlation between the inferred and actual MOC perturbations except for the northern gyre case (case 13). In that case run, the Walin inferred calculation does not capture the full extent of the measured volume flux. In case runs 12 and 13 there is a significant secondary distribution in the lower density ranges. This distribution is not consistent with any Equatorial observations and is most likely a result of near surface pooling of heated water

within the gyres. Such a condition would have the effect of unrealistically altering the terms within the integral in Equation (25) (see Appendix), thus producing a spurious contribution.
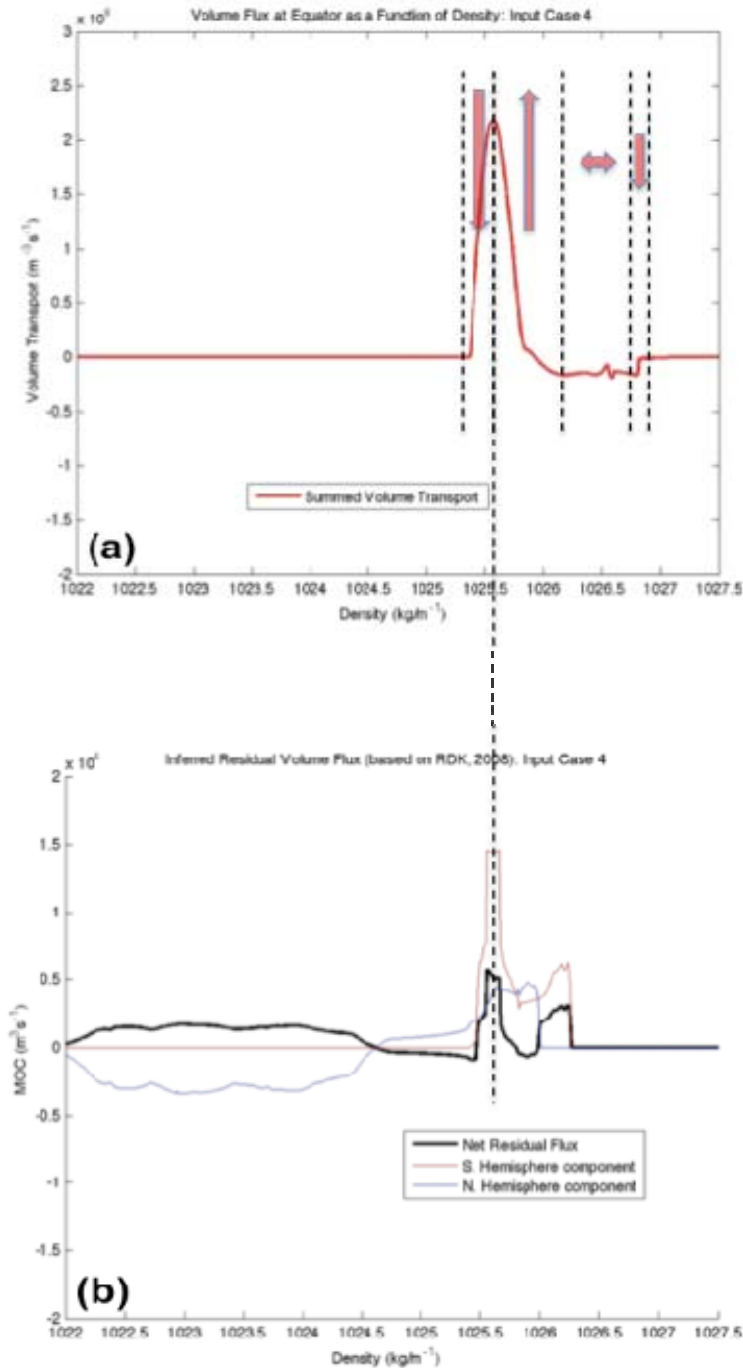
Figure 25. Calculated (a) Equatorial volume flux and (b) Walin-RDK inferred adiabatic volume transport for northern WBC case 4
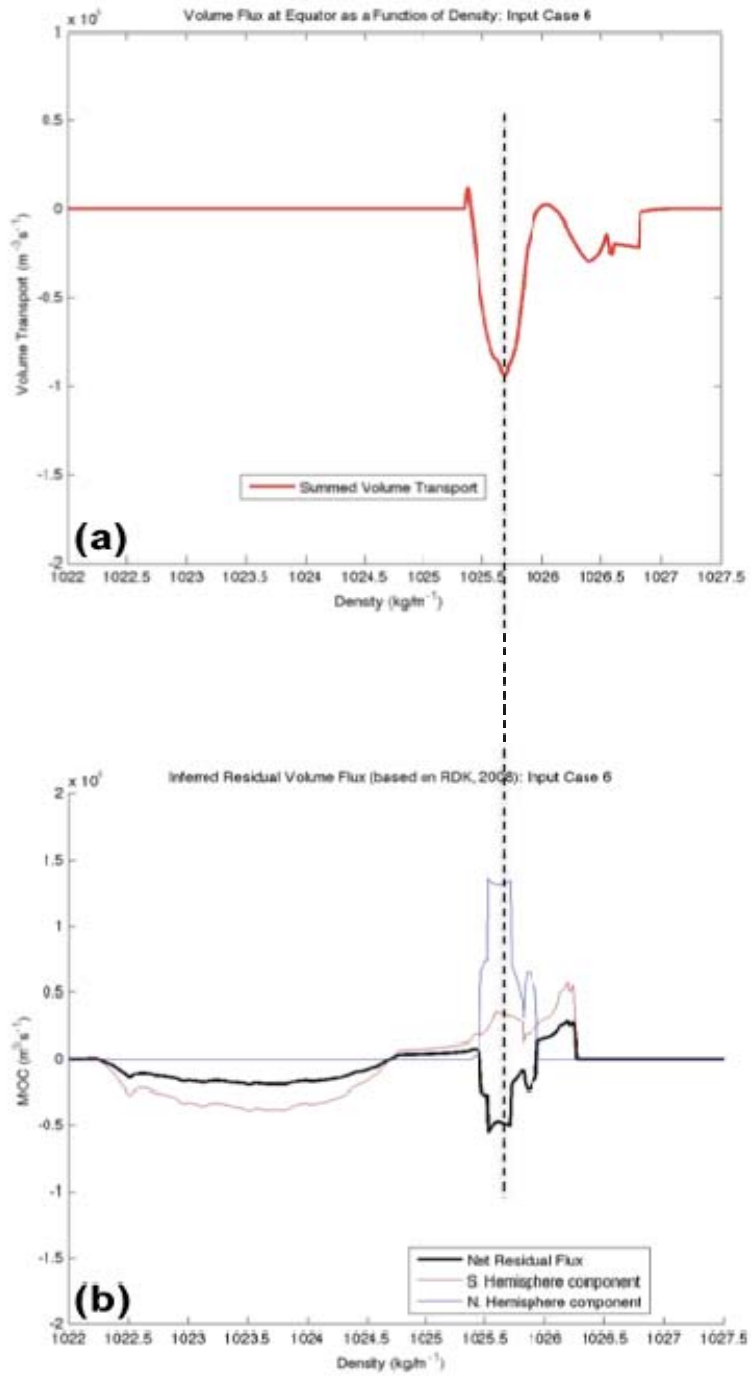
Figure 26.   Calculated (a) Equatorial volume flux and (b) Walin-RDK inferred adiabatic volume transport for southern WBC case 6
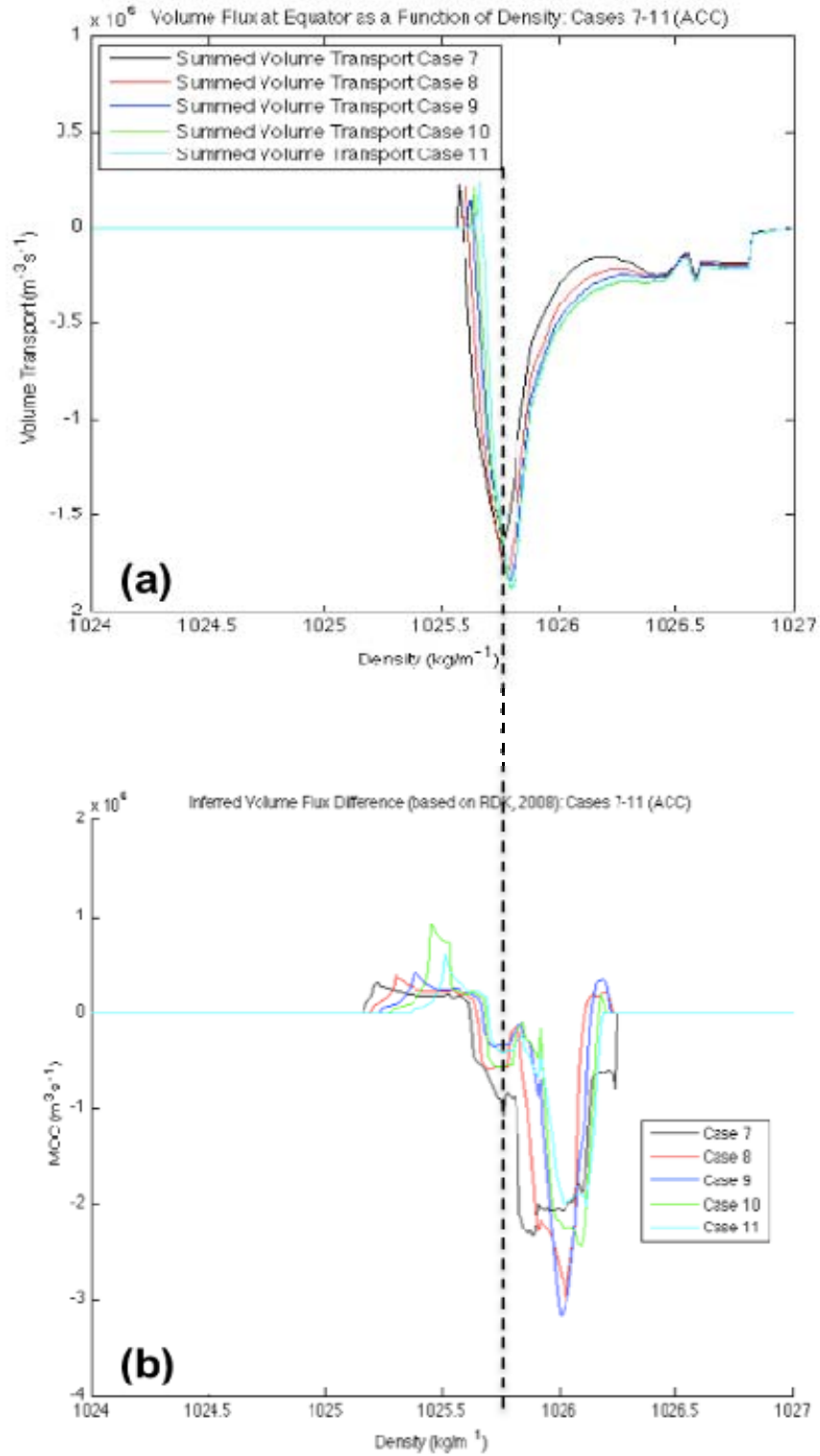
Figure 27.   (a) Equatorial volume flux and (b) Walin-RDK inferred adiabatic volume transport for ACC cases 7 through 11
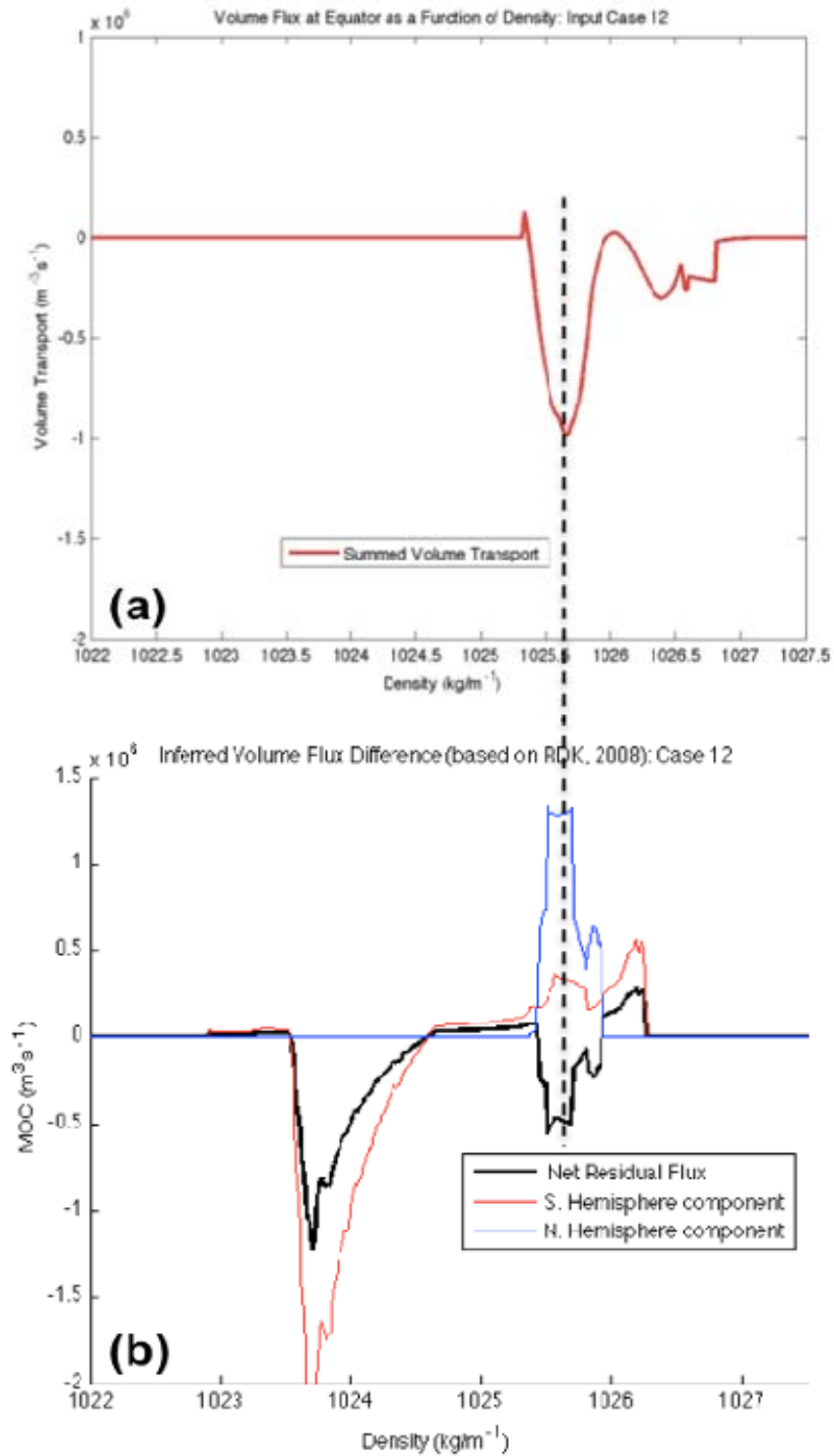
Figure 28.   (a) Equatorial volume flux and (b) Walin-RDK inferred adiabatic volume
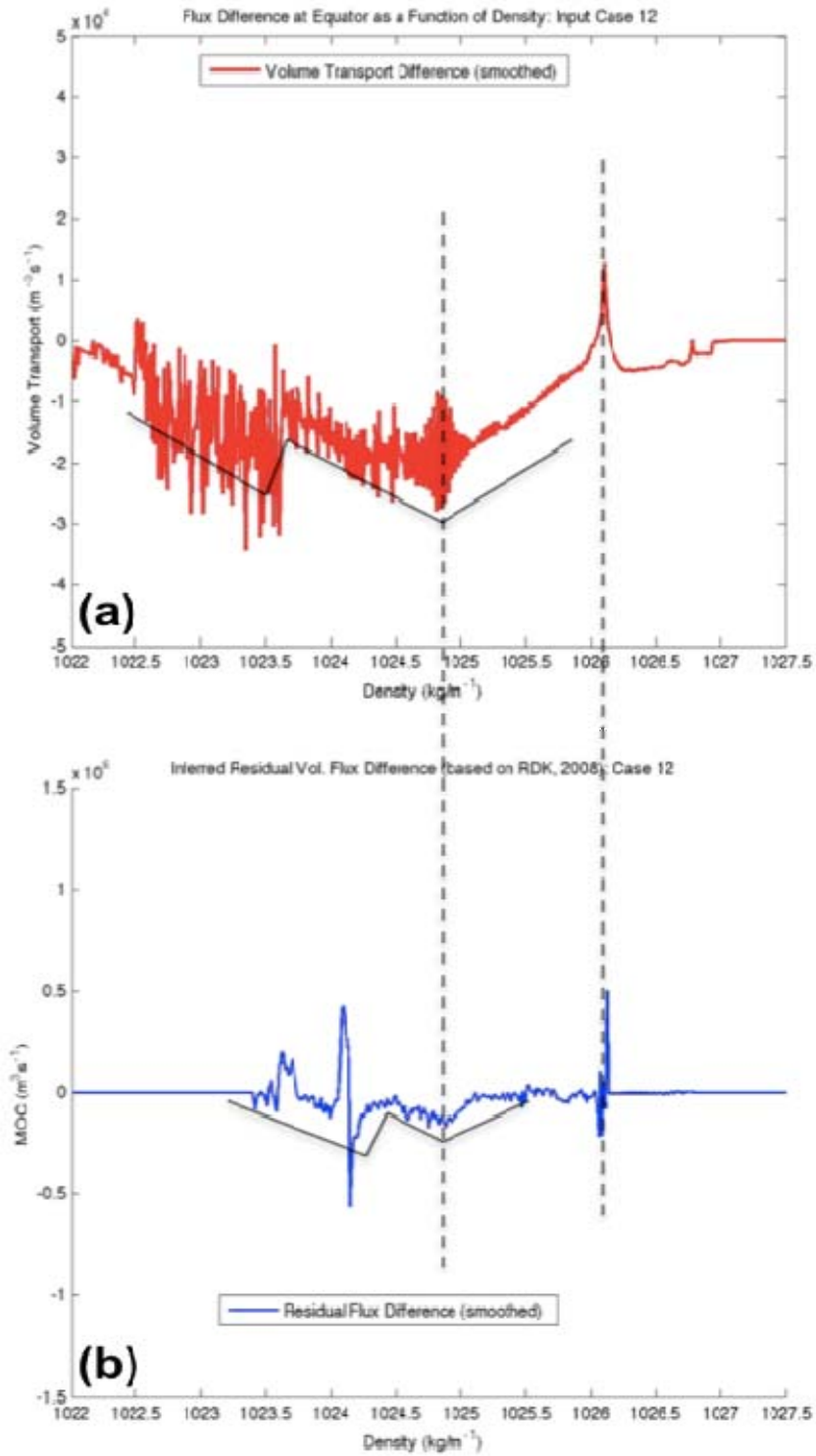transport for southern gyre case 12
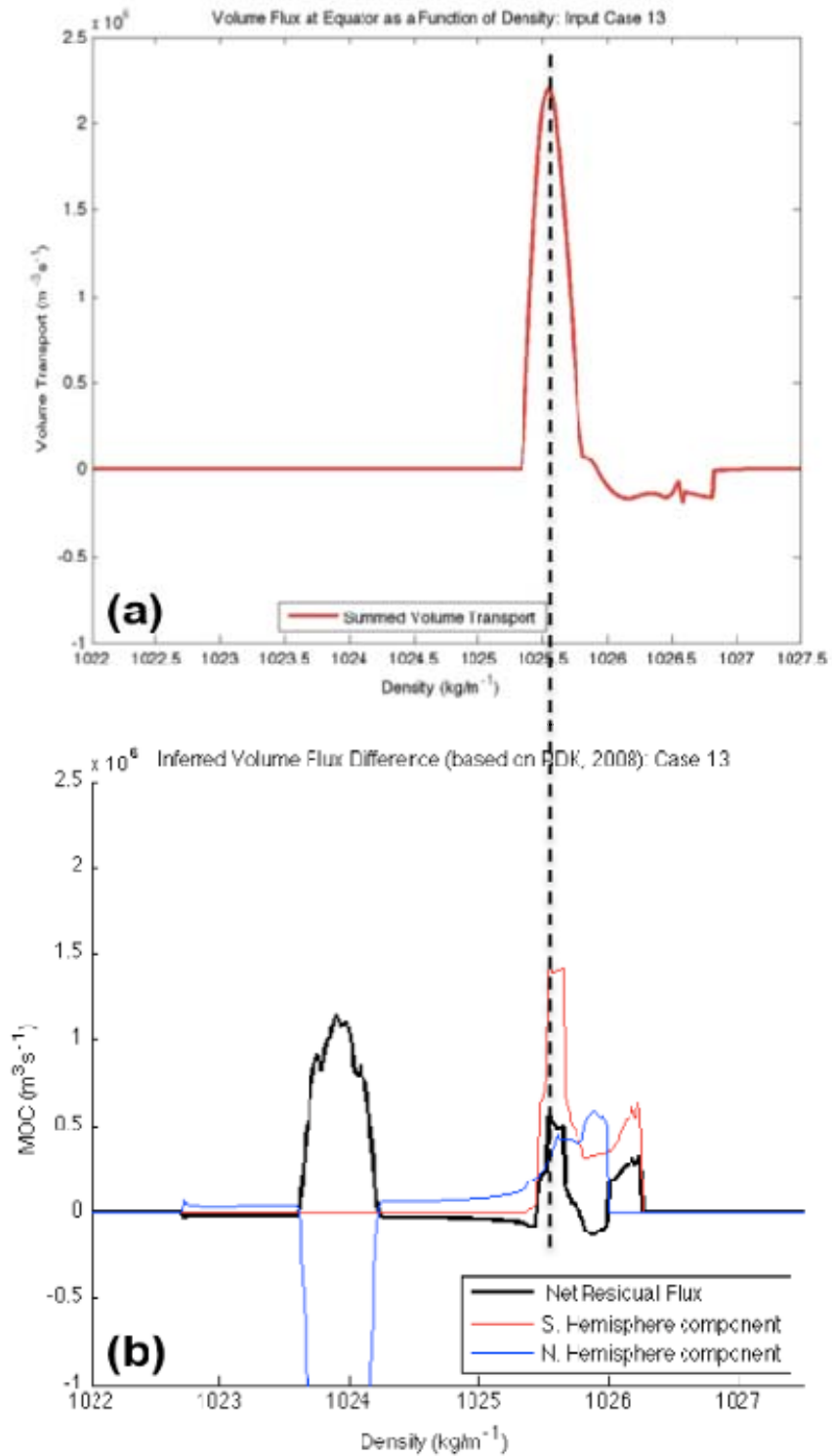
Figure 29.   (a) Equatorial volume flux and (b) Walin-RDK inferred adiabatic volume transport for northern gyre case 13
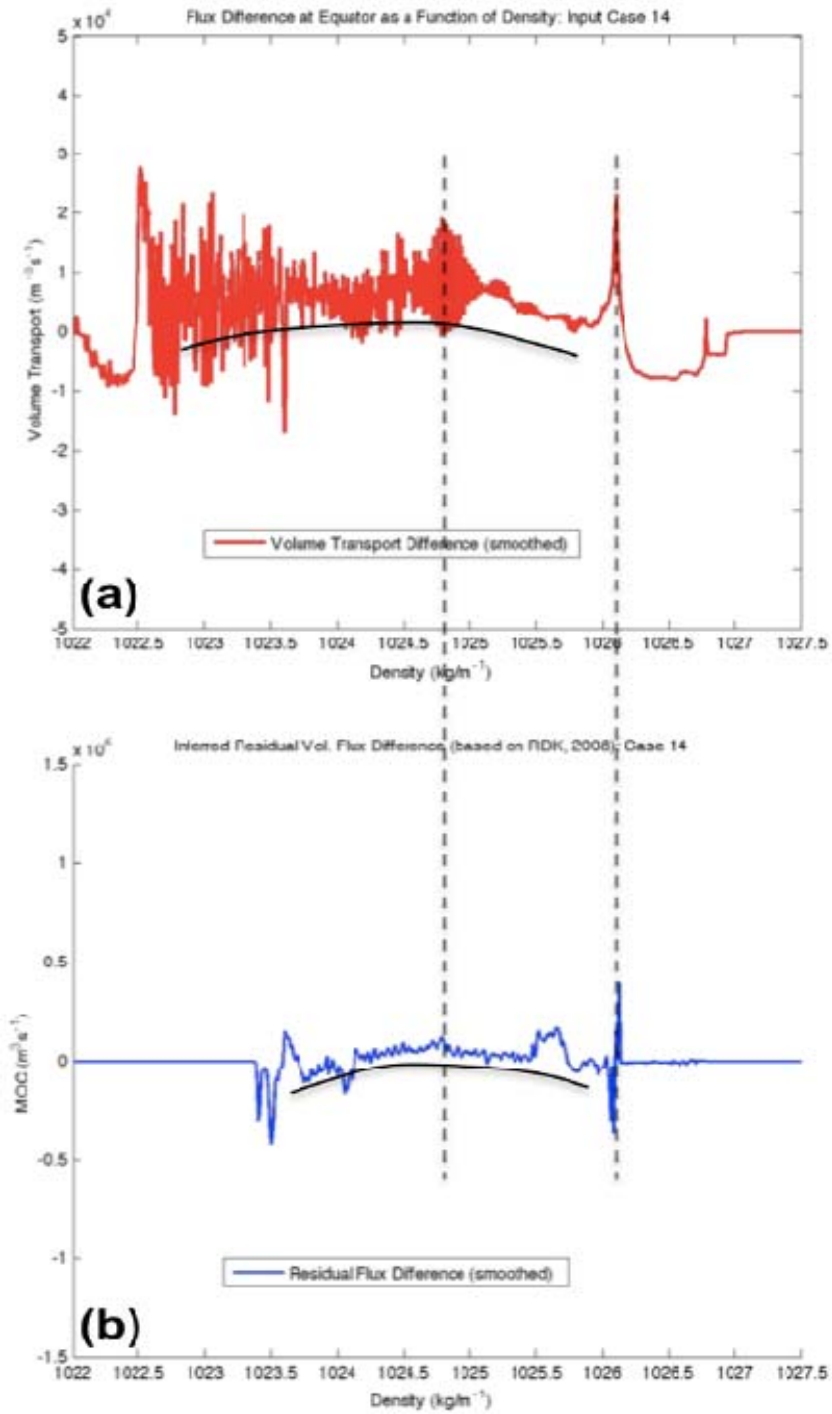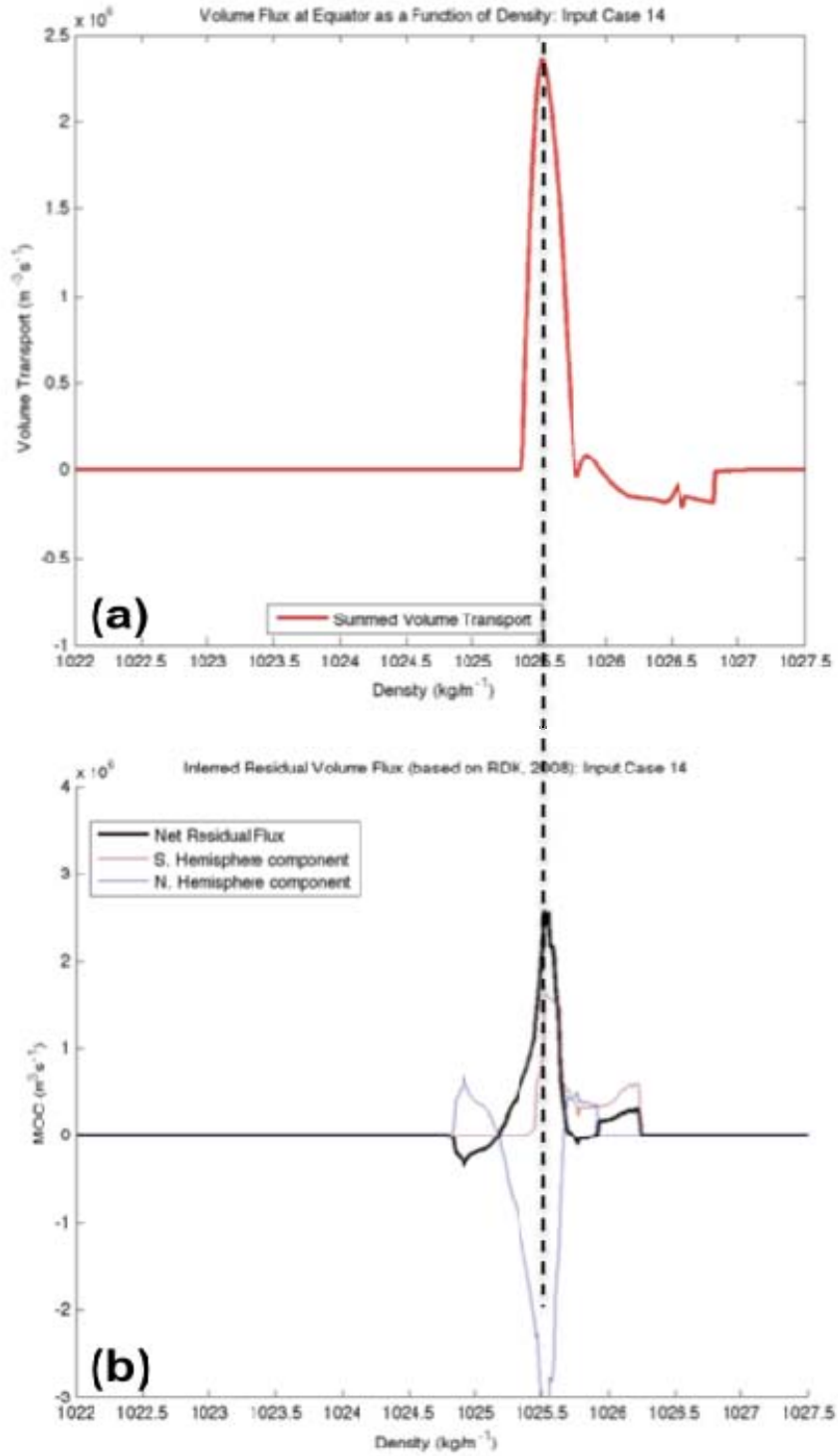
Figure 30.   (a) Equatorial volume flux and (b) Walin-RDK inferred adiabatic volume
transport for northern EBC case 14

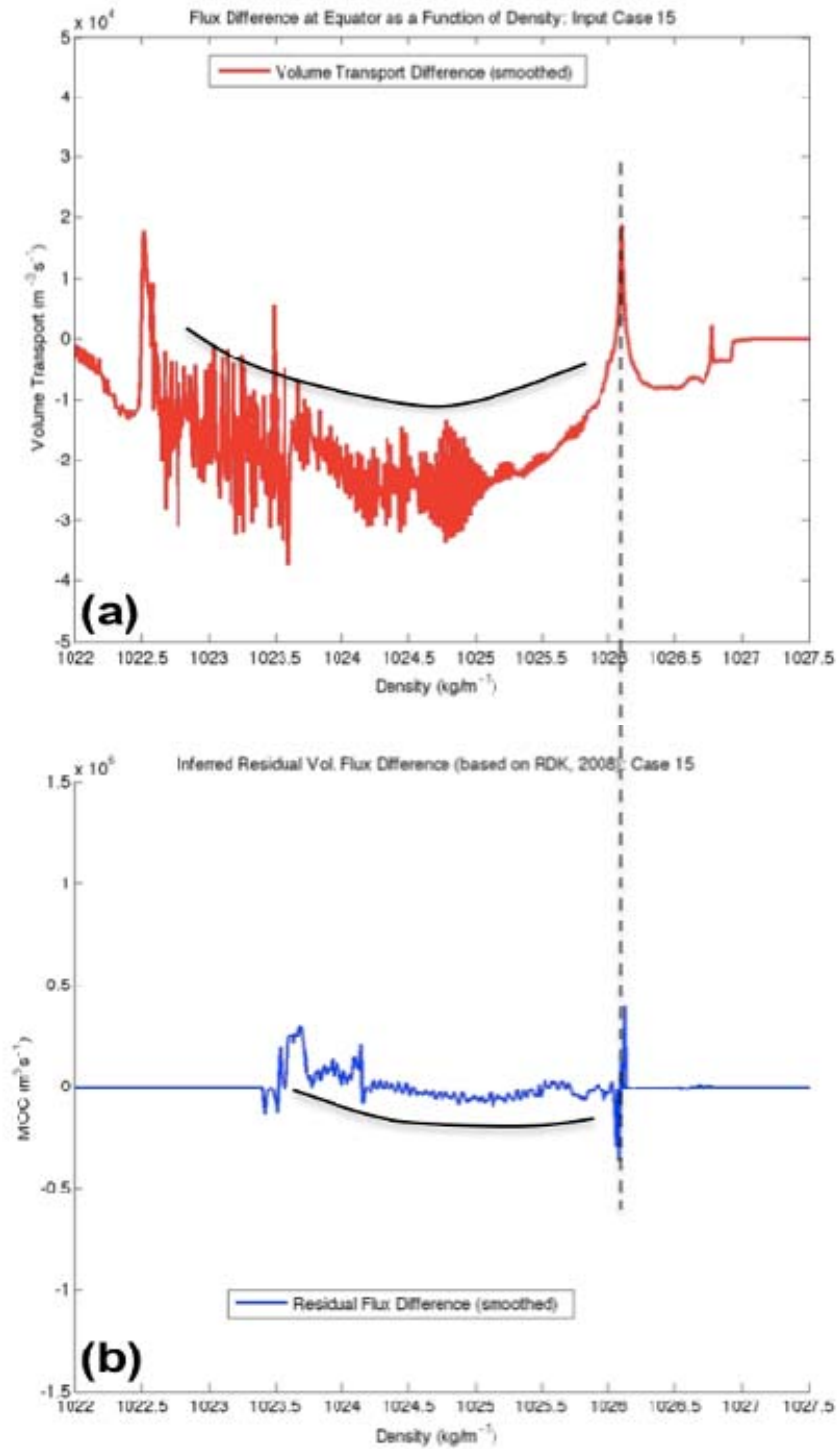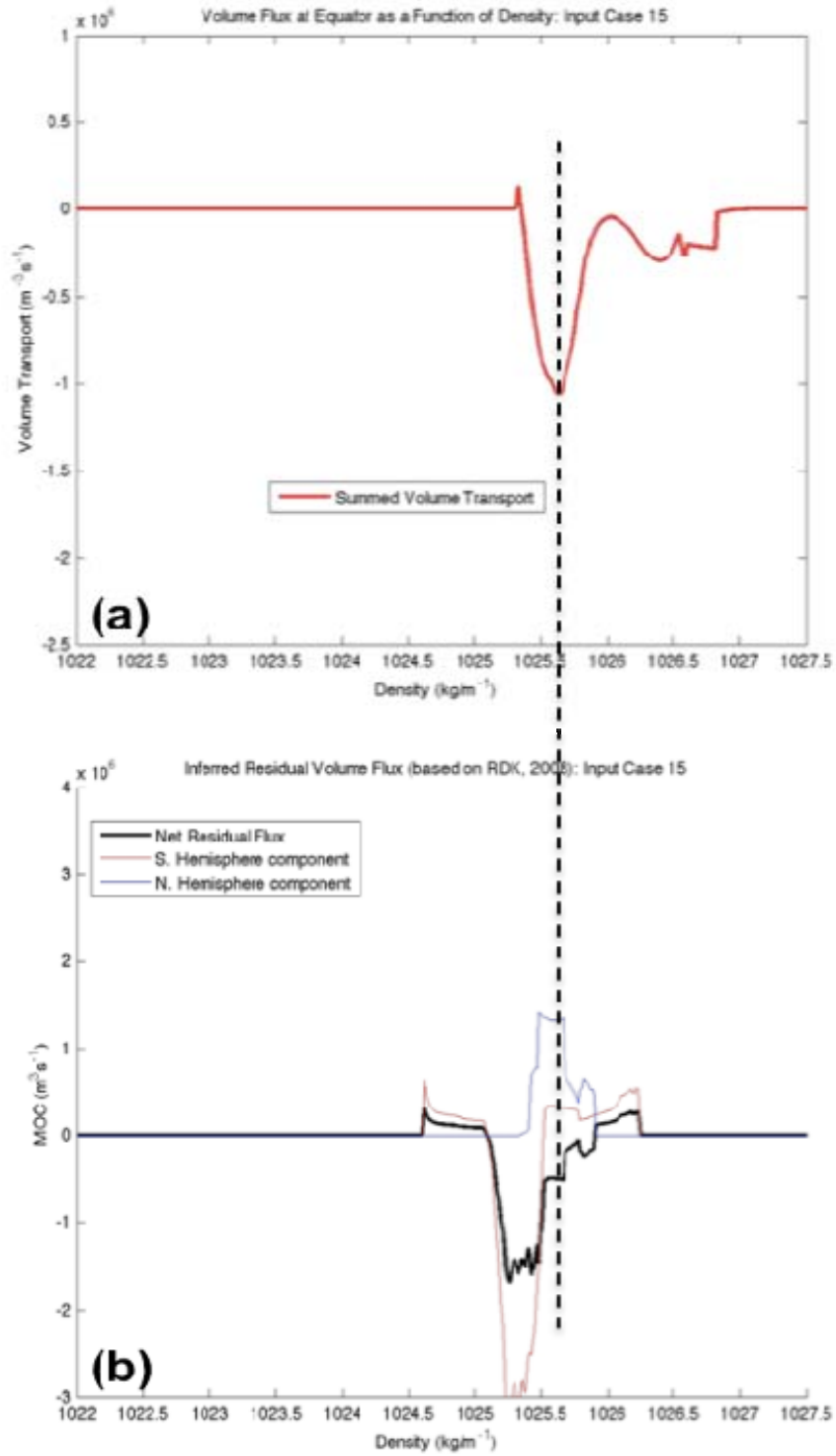Figure 31.   (a) Equatorial volume flux and (b) Walin-RDK inferred adiabatic volume transport for southern EBC case 15

D.   MECHANISMS OF WATER-MASS TRANSFORMATION

In examining the Walin-inferred diagnostics for configurations 1 and 2, it is important to look at the individual terms that comprise the water-mass transformation function. While a complete formulation is found in the appendix, we will denote $F(\sigma)$ here for reference:

$$F(\sigma) = \oiint_{\sigma} \frac{B_0}{|\nabla \sigma_m|} dl \qquad (6)$$

Note that the interplay of three components determines the value of $F(\sigma)$. These are (1) the summed length of the isopycnal contour, (2) the surface bouyancy flux input, B_0, at each point on the isopycnal contour, and (3) the magnitude of the mixed-layer density gradient at each point on the isopycnal contour. The total inferred volume flux is calculated by comparing values of $F(\sigma)$ for each hemisphere. Thus by noting that with few exceptions, the density contour shapes and lengths in each hemisphere are very similar, we can ignore the direct effect of integration and instead concentrate the analysis on components 2 and 3.

These two terms represent two different processes affecting water-mass transformation: the bouyancy flux term is a direct input, while the density gradient contribution is an indirect input whereby the effect of heating shifts the density contours within the mixed layer. Figure 32 provides a schematic illustrating these contributions.
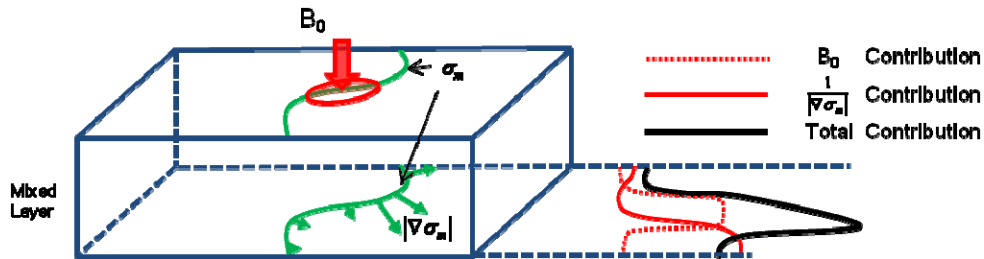
Figure 32.   Schematic of the relative contribution of terms in the overall water-mass transformation function.

The contribution of these two processes can be most directly seen in some of the Configuration 2 (50W) runs. For example, in Figure 31b, the heating perturbation exists in the southern hemisphere. Its direct input is clearly seen in the thin red line. But what is interesting is that there is also a northern contribution (the thin blue line) to the net volume flux despite the lack of a strong surface buoyancy perturbation signal in that region. This contribution is solely based upon the much smaller density gradient values that exist in this region. Smaller density gradients act to amplify the effect of buoyancy flux at the surface felt in the ocean interior. In most cases this indirect effect does not dominate the overall volume flux signal, but it does provide a significant contribution.

E.   DISTRIBUTION OF THE MOC IN TERMS OF DENSITY: ACTUAL AND INFERRED PATTERNS

We have seen the detailed distributions of the MOC in terms of density, and now we more systematically examine the shift in the density of the maximal signal. It is of interest to determine how well the Walin-RKD procedure can capture the location of the maximal MOC signal in density coordinates. The scatter-plots in Figures 33 and 34 compare the density values of maximum MOC directly evaluated at the Equator and the Walin-inferred calculation, with the red line representing a perfect 1-to-1 correlation between the two calculations. Two tables with the numerical sets of results are shown in the Appendix. From the figures, it is clear that the Configuration 1 (direct heating) runs produced much closer density correlations. Caution must be sounded though, as it is probable that the better grouping is partially a result of the weaker thermocline stratification seen in the direct heating experiments, a condition not seen in the real ocean thermocline.
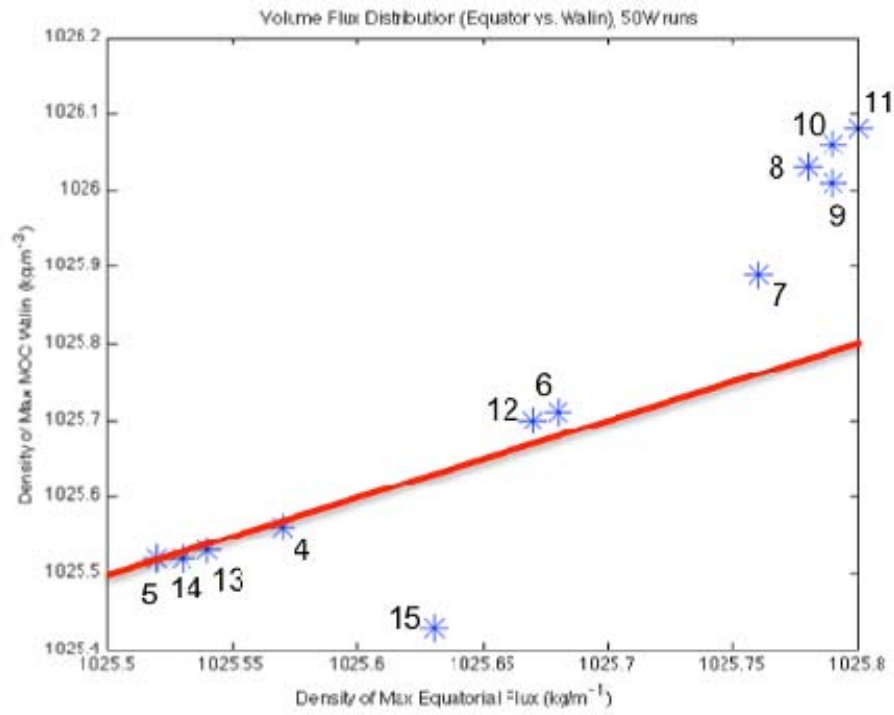
Figure 33.　Representation of Walin-inferred vs. Equatorial MOC$_{max}$ density values for experiment 2. Red line represents 100% correlation
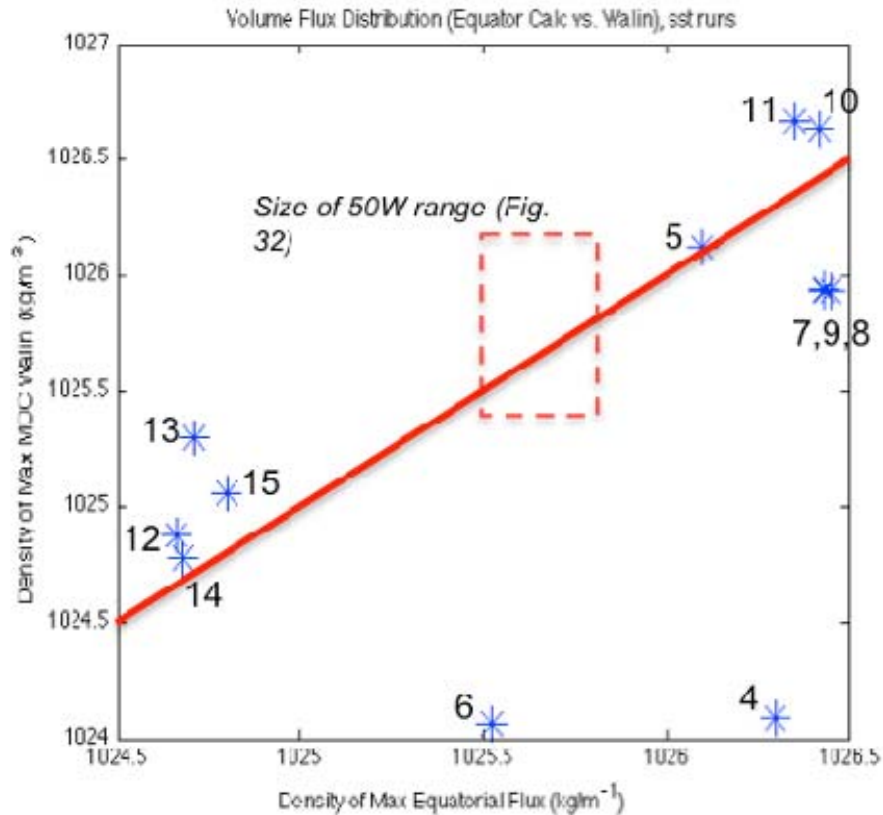
Figure 34.   Representation of Walin-inferred vs. Equatorial MOC_{max} density values for
experiment 1. The solid red line represents 100% correlation

F.   PATHWAYS OF HEAT TRANSPORT

Figures 35–43 show the mapped 3-D surface temperature differences between individual SST case runs and the SST control run. Note that even though the differential temperature range is quite small (0.24 degrees Celsius), these differences are sufficient to reveal the pattern of heat transfer and its variation between the individual runs. However, based on general characteristics of the ocean, it can be generally stated that (1) regions where the temperature differential is positive (orange or red colors) represent areas where the surface heat input tends to deepen the thermocline relative to the control run, and (2) regions where the temperature differential is negative (blue colors) represent areas where the secondary upwelling circulation triggered by the reorganizations of the thermocline controls the response to surface heating.

Figures 35 and 36 show temperature differential patterns for the two mid-latitude WBC perturbation runs (cases 4 and 6). Three interesting features draw immediate attention. First and somewhat counter-intuitively, the regions of largest cold water upwelling are located almost directly below the regions of the sea-surface heating perturbations. This pattern is also present throughout all of the examples, regardless of perturbation location, shown in this study. Second, it can clearly be seen that upwelling in the case 6 (southern WBC) run is clearly stronger than the upwelling below the perturbation in the case 4 (northern WBC) run. In a similar manner, the warm water subduction seen in the case 4 run is clearly stronger than what is seen in the case 6 run. Finally, it is very interesting to note how the rest of the ocean interior is very much insulated from the heating or cooling signals seen in both of these case runs. Heat transfer to this surface at depth is localized when the perturbation source is located in either WBC.
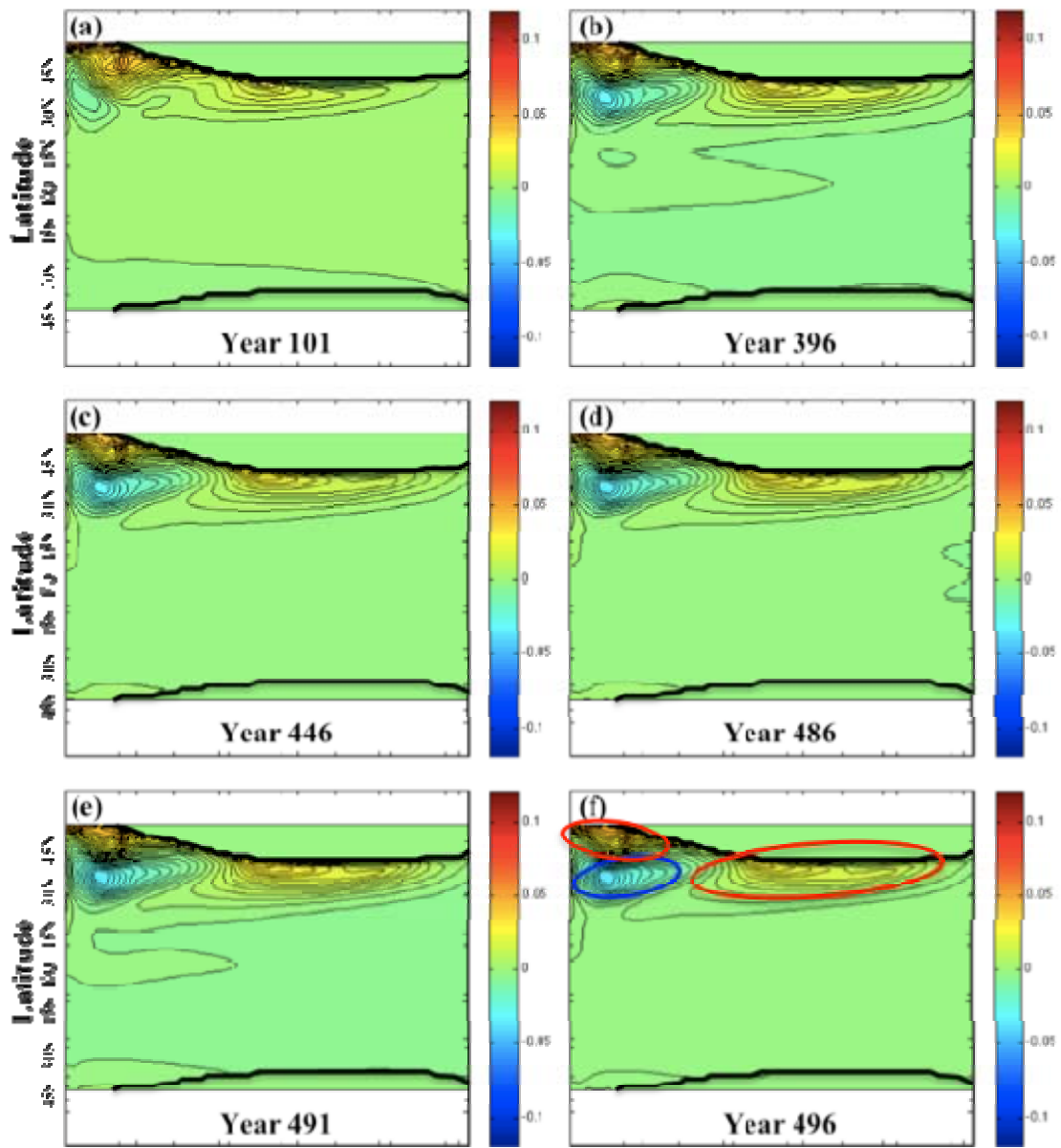
Figure 35.   2-D view of temperature difference between SST case 4 and the SST control run. Figures (a) through (e) show the progression at six different years into the model run.
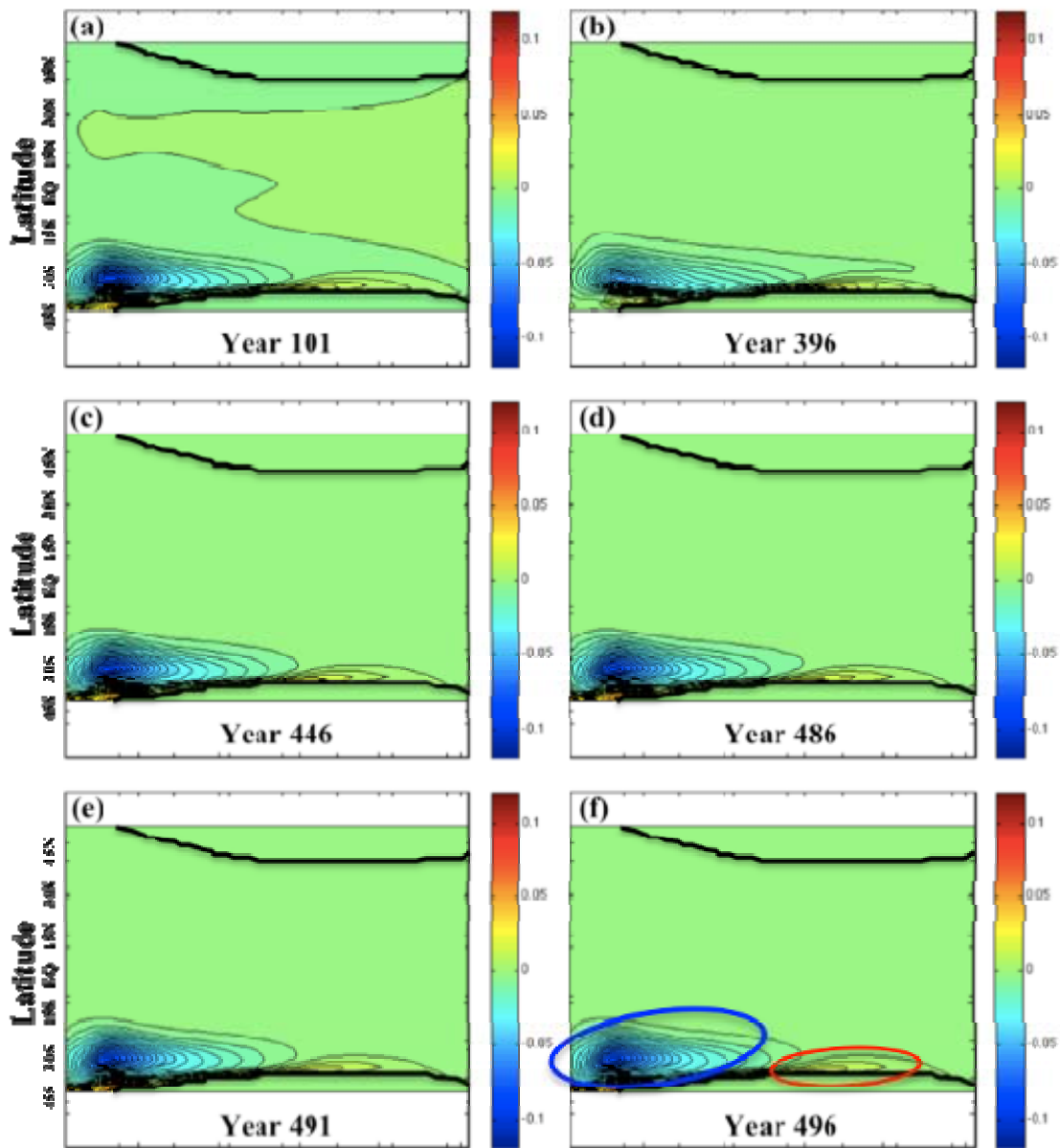
Figure 36.   2-D view of temperature difference between SST case 6 and the SST control run.

Figures 37–40 show the heating progression for three ACC perturbation case runs (cases 7, 9, and 10). As opposed to the WBC perturbation runs, when portions of the ACC are heated the effects are felt throughout the ocean interior. However, the degree to which the ocean interior is affected differs as the heating perturbation is moved from west (case 7) to east (case 10). In all three cases, near the end of the model run a state exists

where subduction of warmer waters occurs in the western half of the ACC boundary region, while in the east ACC boundary region colder waters are upwelled (or possibly advected from poleward regions). For the case 7 end-state, this west-to-east gradient is strongest, but the contrast is progressively weaker for case 9 and then for case 10. Ironically, the infiltration of heat into the interior is weakest for case 7, but progressively becomes stronger by case 10. In addition, the progression to the end-state is different between model runs, with the west-to-east heating gradient going from weakest to strongest with time for case 7, and progressing in the opposite manner for case 10. In all of the ACC cases, the path in which heat is transported to the interior equatorial regions appears to be through the western boundary region, perhaps via the DWBC.
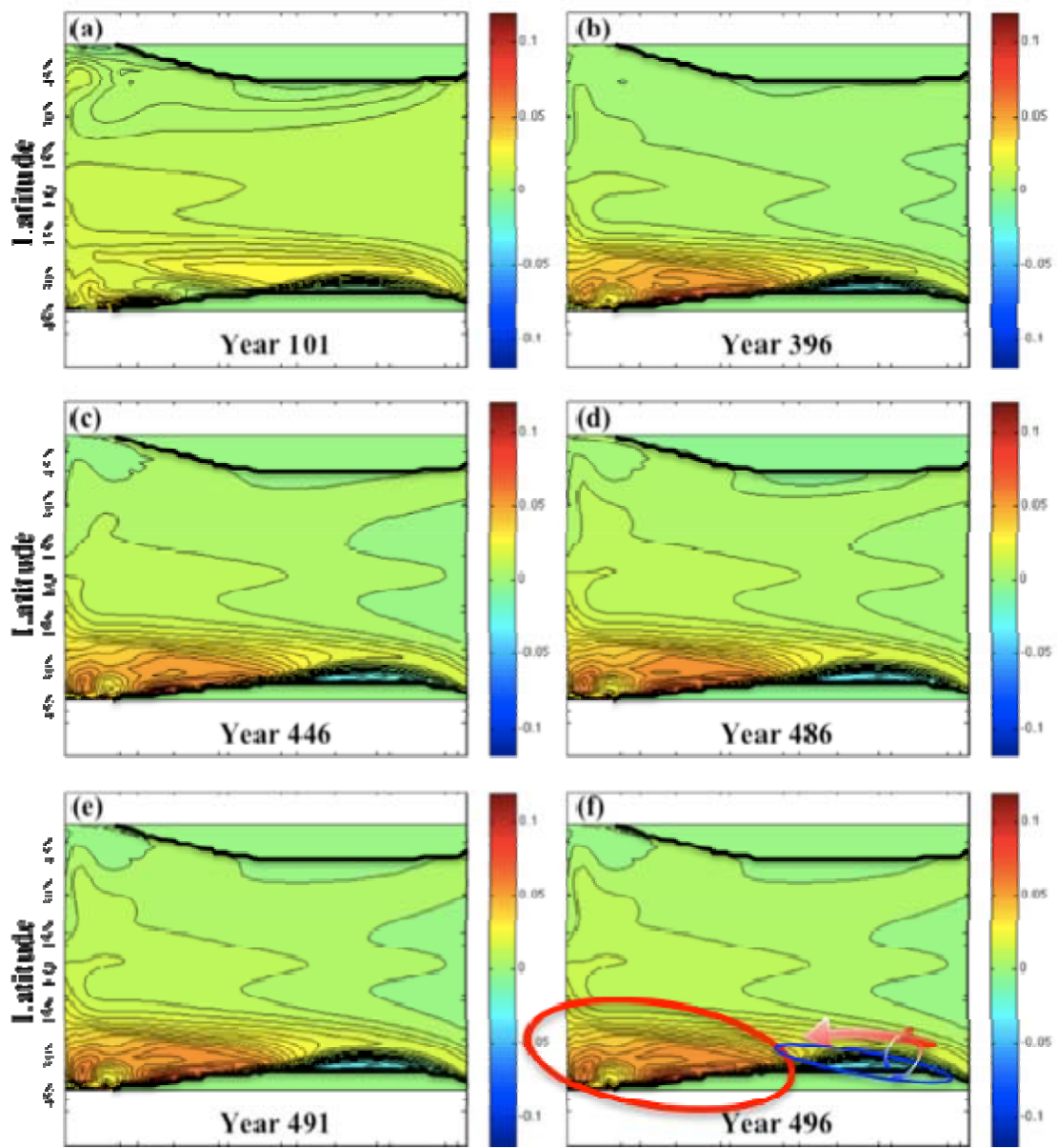
Figure 37.   2-D view of temperature difference between SST case 7 and the SST control run.
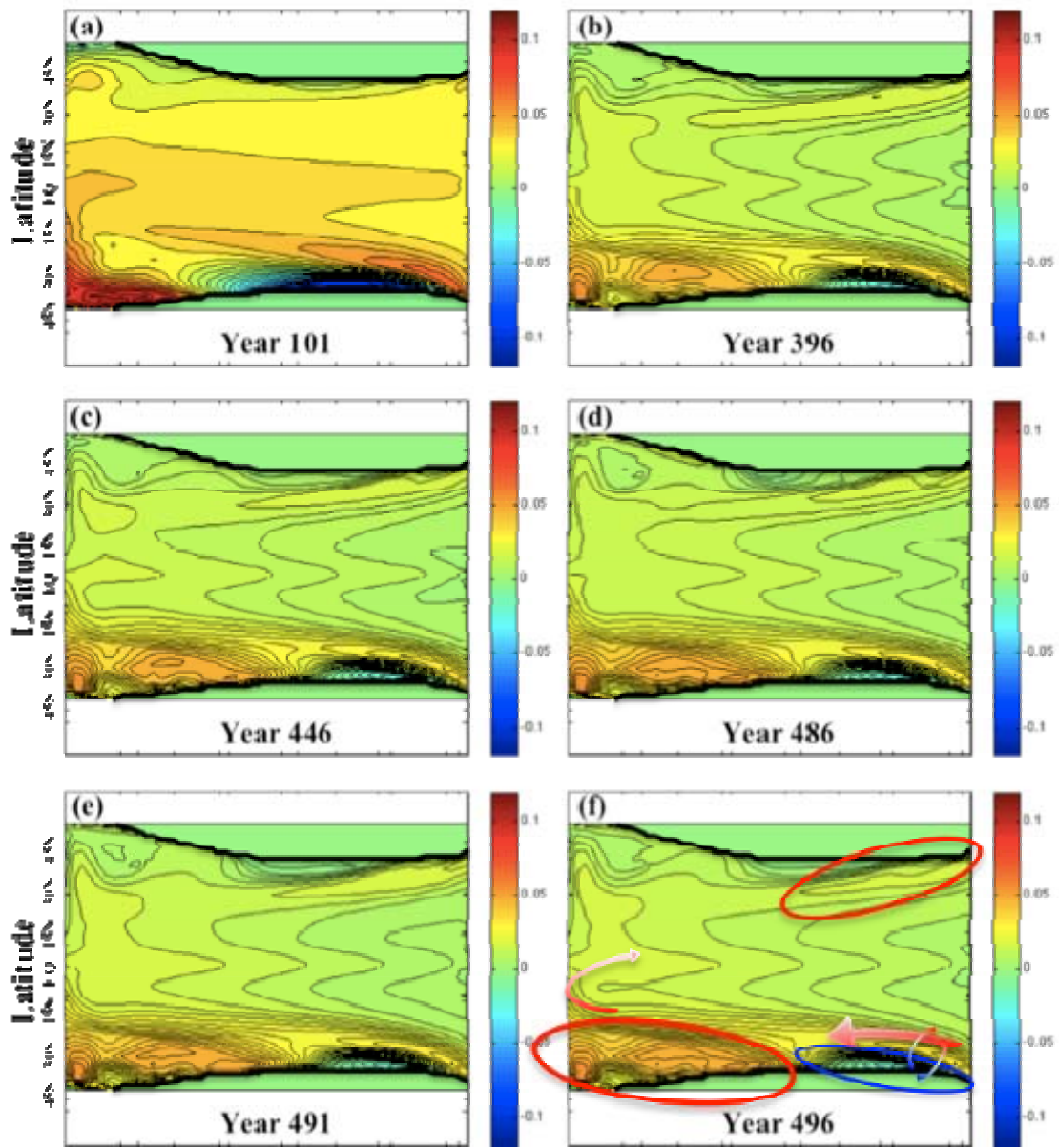
Figure 38.   2-D view of temperature difference between SST case 9 and the SST control run.
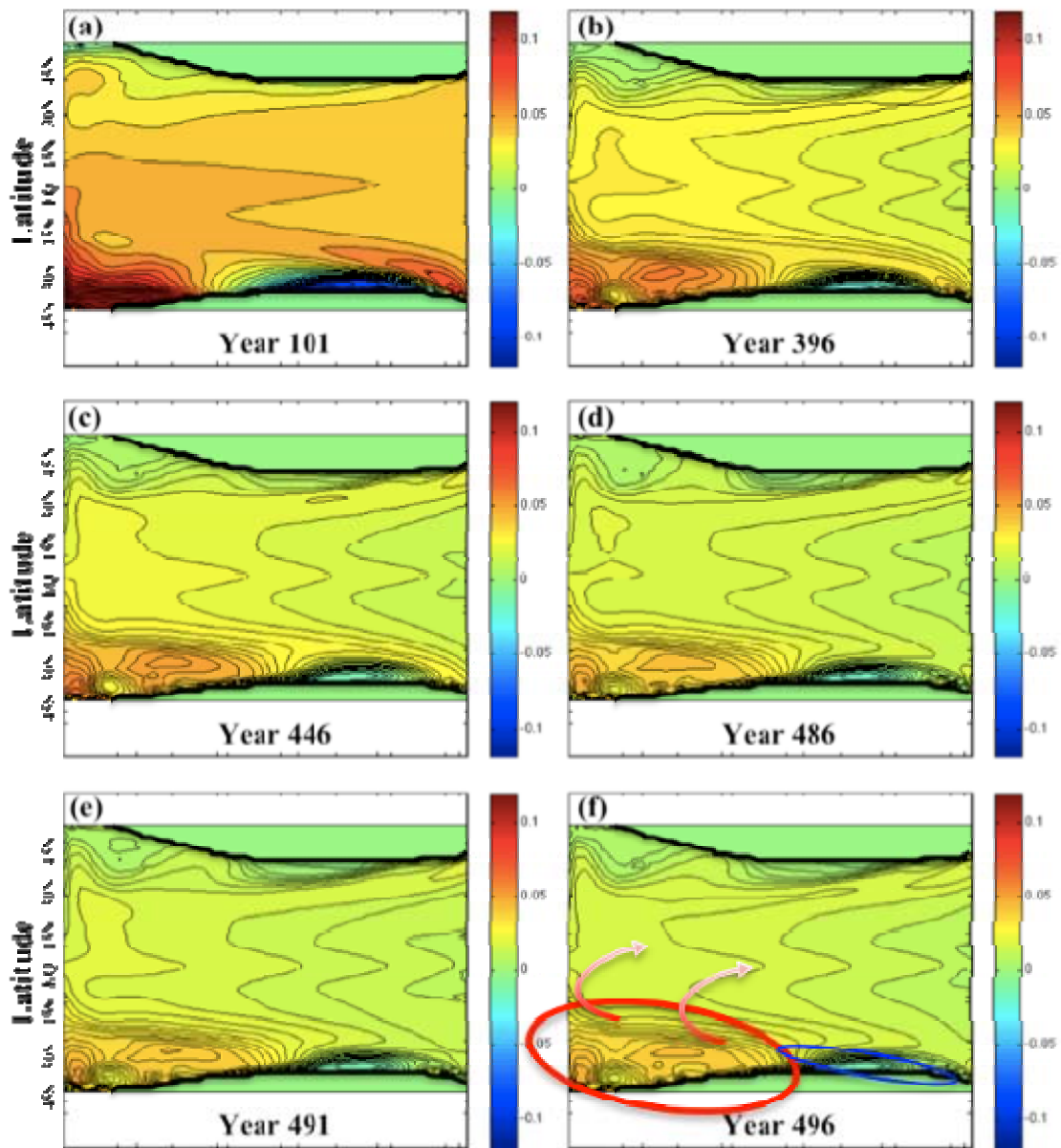
Figure 39.   2-D view of temperature difference between SST case 10 and the SST control run. (a) through (e) show the progression at six different years into the model run.

For SST cases 12–15 (Figures 40–43), and especially for cases 14 and 15, the ocean interior is more significantly affected by the sea-surface heat input than any of the other case runs. In addition, the primary pathway appears to be through the EBCs, a more direct connection to the surface heating source. For cases 12 and 13, a subduction differential between the two cases (similar to cases 4 and 6) can be seen underneath the

56

perturbation region. This larger region of relatively cooler water helps contribute to a stronger west to east positive gradient in the equatorial regions of the case 12 run. Cases 14 and 15 have the least upwelling response and the strongest interior temperature differences of any of the runs, however, there is little asymmetry in the overall flows for these two case runs.
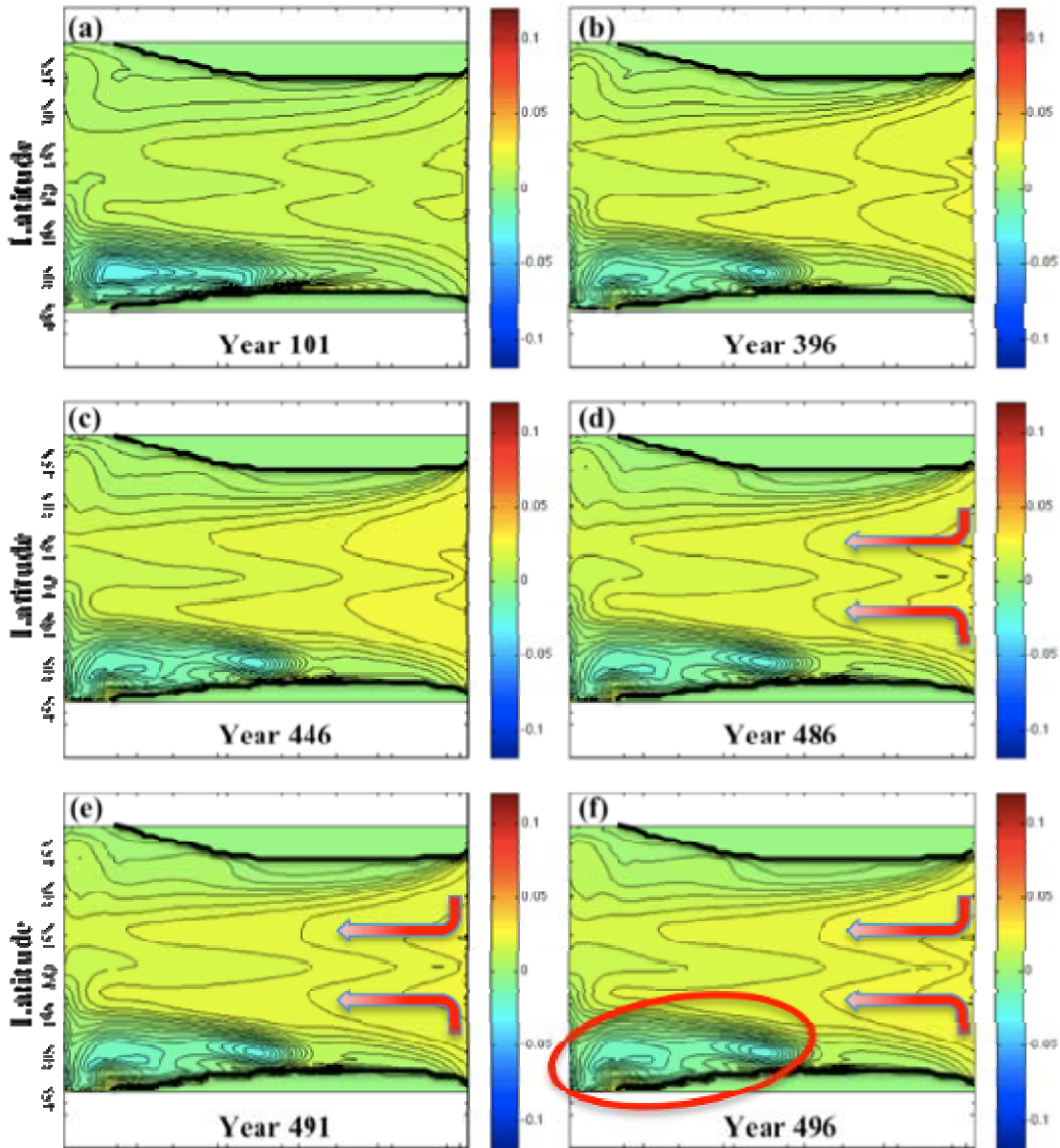
Figure 40. 2-D view of temperature difference between SST case 12 and the SST control run. Note the slightly stronger contrast from light green to yellow in the equatorial region as compared to Figure 40.

57
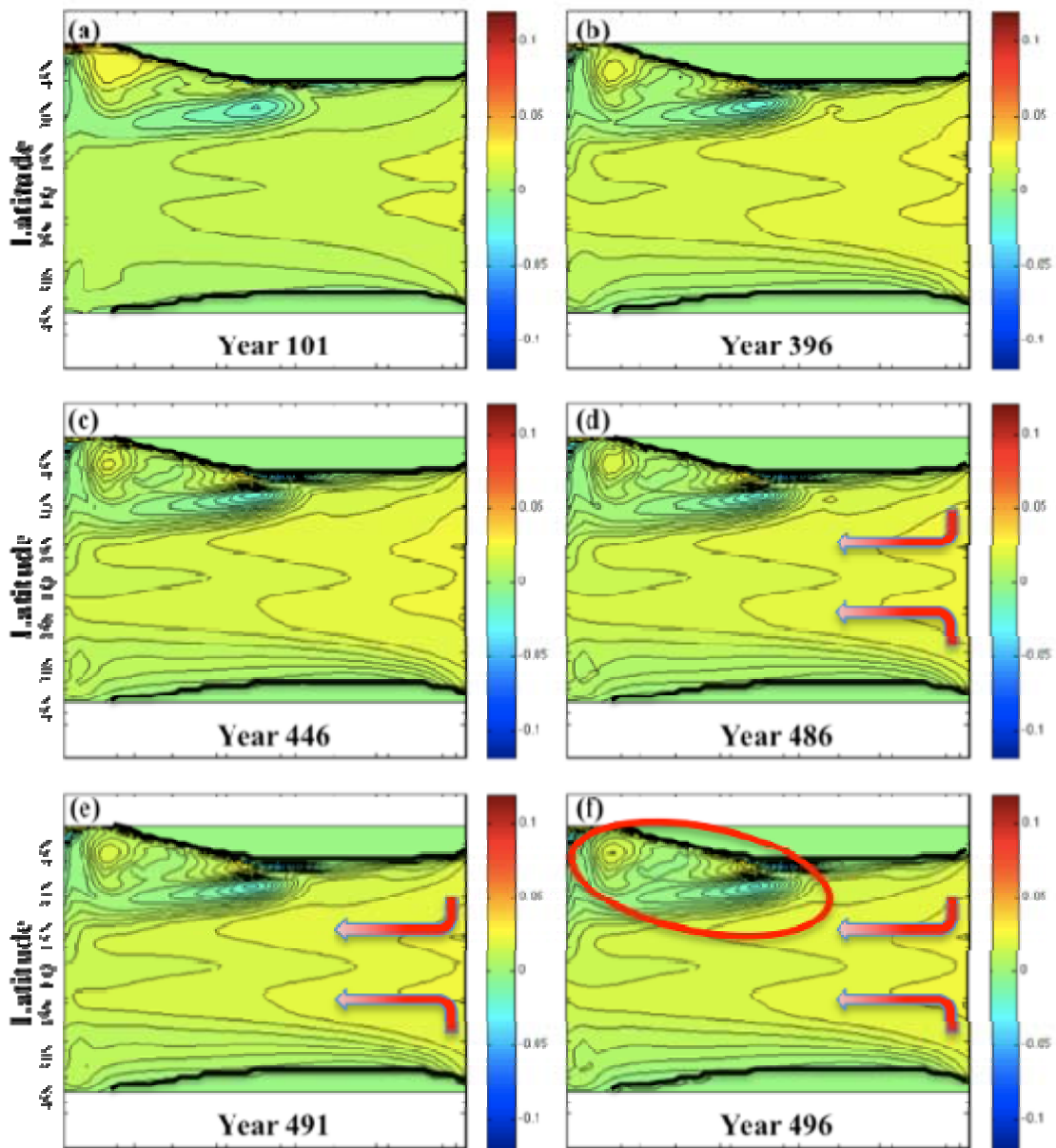
Figure 41.   2-D view of temperature difference between SST case 13 and the SST control run. (a) through (e) show the progression at six different years into the model run.
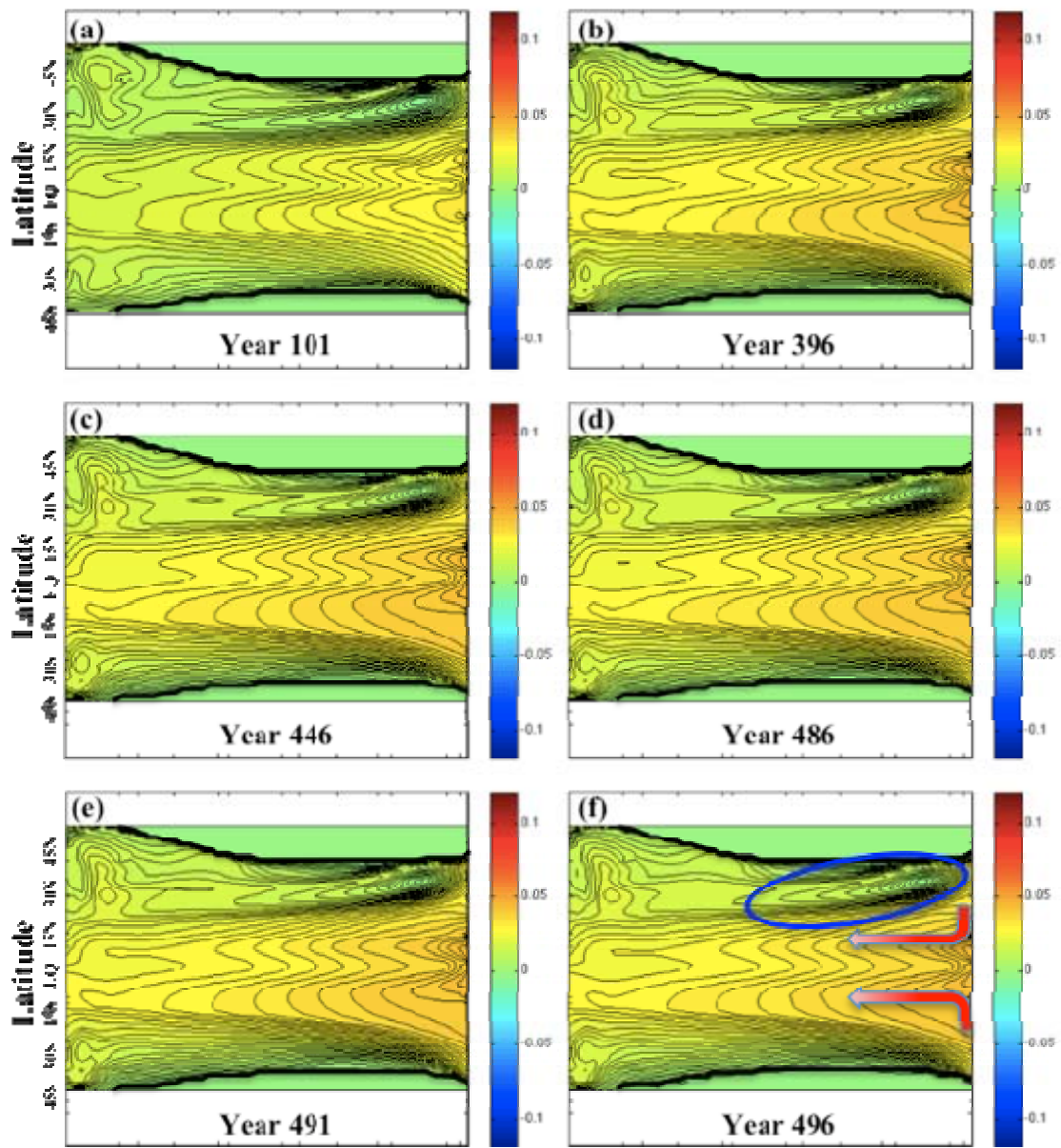
Figure 42.   2-D view of temperature difference between SST case 14 and the SST control run. (a) through (e) show the progression at six different years into the model run.
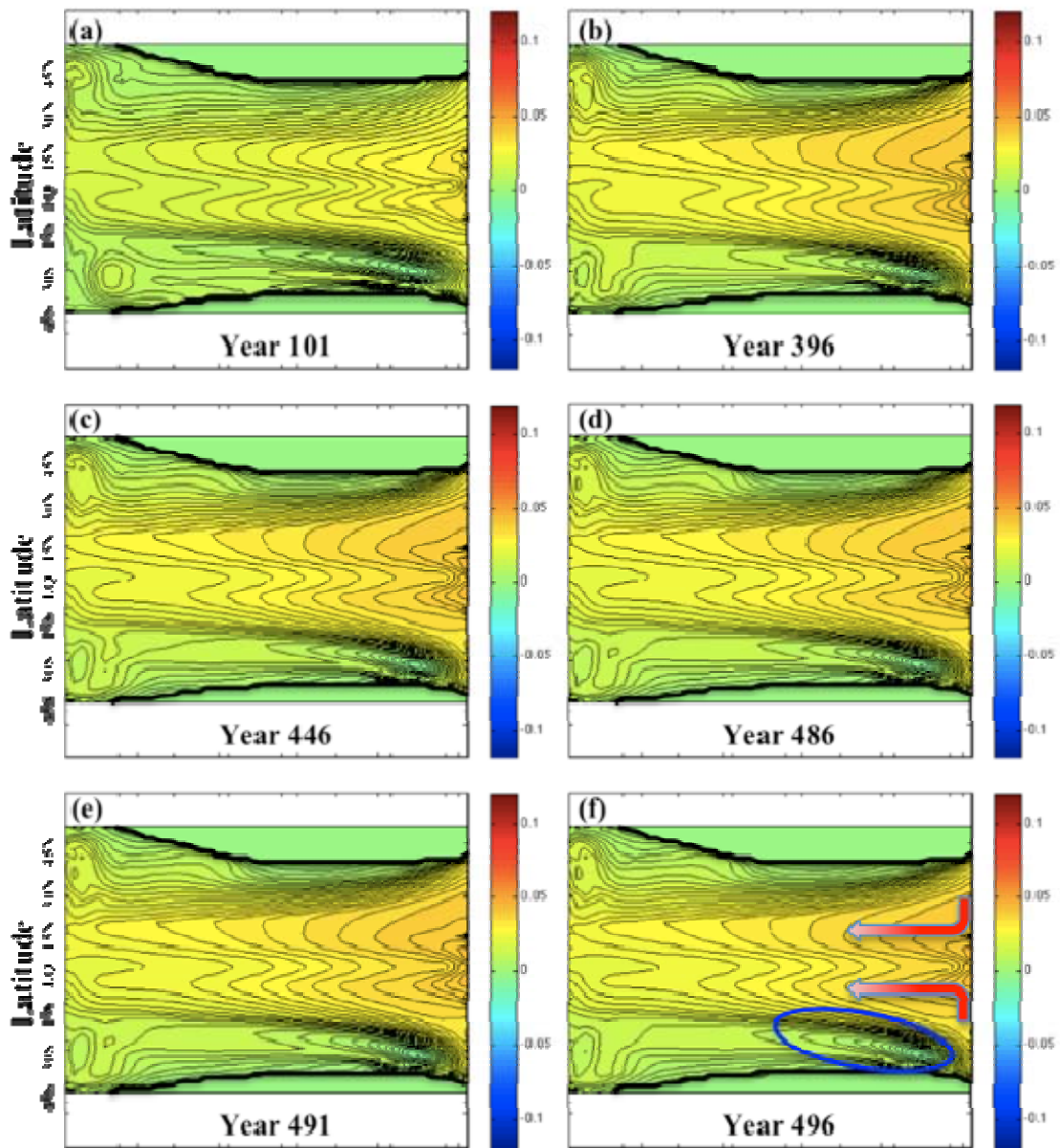
Figure 43.   2-D view of temperature difference between SST case 15 and the SST control run. (a) through (e) show the progression at six different years into the model run.

Again, it should be noted that a positive differential is not synonymous with positive total heat transport into the interior. Nonetheless, the differences highlight the impact of surface heating felt by the ocean interior.

G. SENSITIVITY (GAMMA) VALUES AND COMPARISONS

Figures 44 and 45 show the results of the Sensitivity value calculations for experiments 2 and 1. Nearly all of the direct heating runs show sensitivities that are approximately two orders of magnitude, greater than the SST forced runs. In most cases, the Walin-based calculations (blue stars) match up well with the Equatorial volume flux calculations (red stars). The only exceptions occur in the WBC and the northern gyre runs.
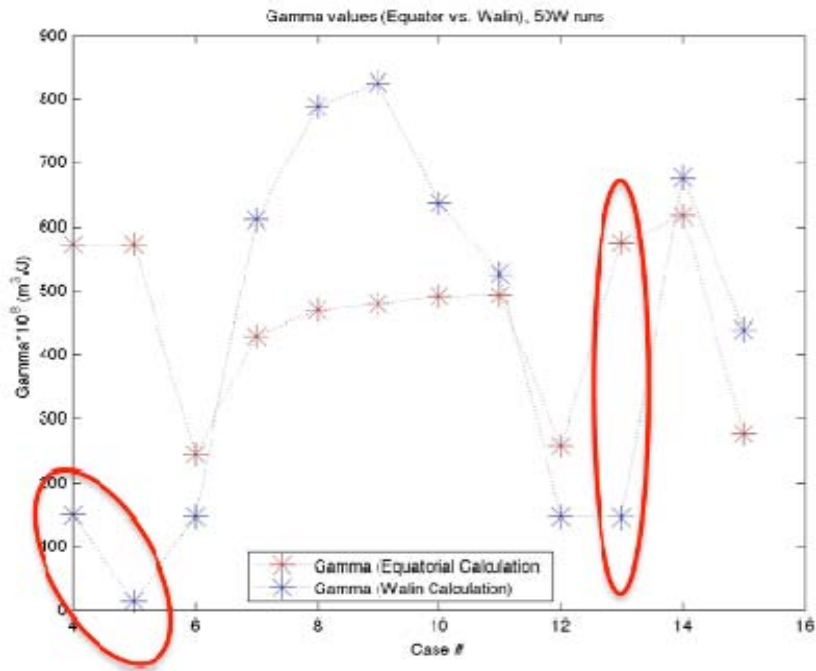
Figure 44. Sensitivity values for heat flux forced runs
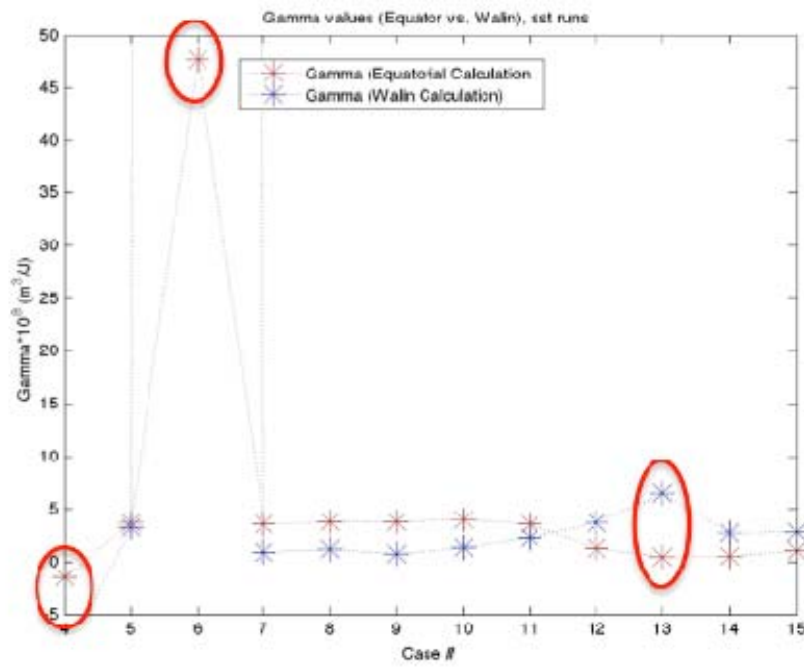
Figure 45.   Sensitivity values for SST forced runs

V.   DISCUSSION AND CONCLUSIONS

A fundamental problem in physical oceanography and climate science concerns the mechanisms for transport of heat from sea-surface into the ocean interior and its associated impact on the large-scale circulation patterns. The physics and dynamics at play are not fully understood. The difficulties in developing a transparent and intuitive view of the MOC stem from the necessity to conjoin the mechanical and thermodynamic forcing mechanisms in a single theoretical framework. This study attempts to elucidate the connection between the MOC and the air-sea heat transfer by systematically exploring the role of the location of heat input. The analysis is based on the inspection of two sets of experiments: one configuration set utilized a SST profile that was perturbed in different spatial locations, while the other configuration set utilized direct heating of an otherwise semi-insulated ocean to the same locations. Through the application of the diagnostic methods described in section III, characteristics and patterns of interior circulation were linked with the spatially differing heat perturbations. Unique pathways of heat transport were identified in the model runs and physically explained.

The SST forced runs in experiment one produced extremely weak responses with sensitivity levels shown to be two orders of magnitude less than their counterpart direct heating experiments (see Figures 44 and 45). There are several possible reasons for this small signal response. Most likely, the perturbation signals were suppressed in the presence of the larger scale patterns of forcing governing the SST runs. These large-scale patterns of wind-stress forcing and baseline temperature forcing were completely symmetric, thus potentially inhibiting the effects of any localized perturbations. Nonetheless, responses at the Equator were still detected. Indeed, the similarity of the Equatorial volume flux calculations within the ACC case runs and their uniqueness from the other case run distributions testifies to the direct link between the thermodynamic forcing at the sea-surface and the inter-hemispheric transport.

The isopycnal surface analysis also yielded detectable changes between the SST case runs in terms of the pattern of interior heating. The pathways of heat transport resulting from forcing the WBC, ACC, and gyre/EBC regions differ in several key aspects. The WBC perturbations produced only localized changes from the control within the analyzed interior surface. The ACC and gyre/EBC perturbations all produced more broad-scale interior heating, but the pathways and shape of the heating distribution differed, with the ACC perturbations feeding heat into the interior via the western boundary. Meanwhile, the other perturbations seem to have fed heat into the interior directly by a combination of the time-mean advection and lateral diffusive spreading.

Perhaps due in part to the limited size of the signal response, there was a significant noise element introduced into the Equatorial volume flux calculations. This noise was predominantly seen in the lower density regions, where the z mesh component was smallest (more potential for interpolation error) and surface processes may have unduly influenced the interpolated summations. Despite this noise, distribution patterns in the case of the gyres and EBCs could be loosely correlated to the Walin-based inferred volume flux calculation. However, correlations were much weaker in those cases where the perturbations centered in highly advective regions, such as the WBCs and the ACC. Furthermore, the maximum MOC values in the inferred and actual calculations (Figure 44) differ substantially. This scattering, as well as the density "shifting" between Walin-derived and Equatorial distributions within several of the cases, seem to indicate that diabatic processes are interfering with the transmission of surface forcing signals adiabatically into the interior ocean. Overall, while the Walin-RKD calculations did not capture the Equatorial volume transport in all details, especially with regard to the magnitude of the circulation, there was a broader correlation in terms of the overall distribution shape within the SST forced runs.

Several spurious signals were also seen in nearly all of the Walin calculated MOC distributions, the most notable instance occurring around the density range of 1026.05 to 1026.15. The existence of this signal in nearly all of the runs, and its consistent location in the distribution, indicate that this is not a transient feature. One potential explanation for this effect is the lack of stratification seen at shallower depths in the experiment (1)

runs—a result of maintaining the vertical mixing coefficient at 10^{-6} m^2/s. Thus, a large volume of water could be accounted for within a small density interval.

The modeled circulation was more responsive to the forcing by the direct heating (Configuration two). Generally, the MOC magnitudes were approximately 2–2.5 Sv for the northern hemisphere perturbation runs, 1 Sv for the southern hemisphere mid-latitude perturbations, and 1.5–2 Sv for the ACC perturbation runs. This overall result is interesting, considering that: (1) the thermocline is more diffuse than in the Configuration one runs, and (2) the geometry and wind forcing patterns are the same between the two experiments. These differences are attributed to relative size of the perturbation relative to the background state, which were larger for the second case. There were no other external processes of a magnitude large enough to overwhelm the 50W perturbation signal.

But why is there such an asymmetry between the ocean's response to northern hemisphere, southern mid-latitudes, and ACC perturbations? Some insight was gained by the inspection of the Equatorial velocity profiles in the model runs. The physical explanation is indicated in Figure 46, which schematically represents the meridional velocity component.
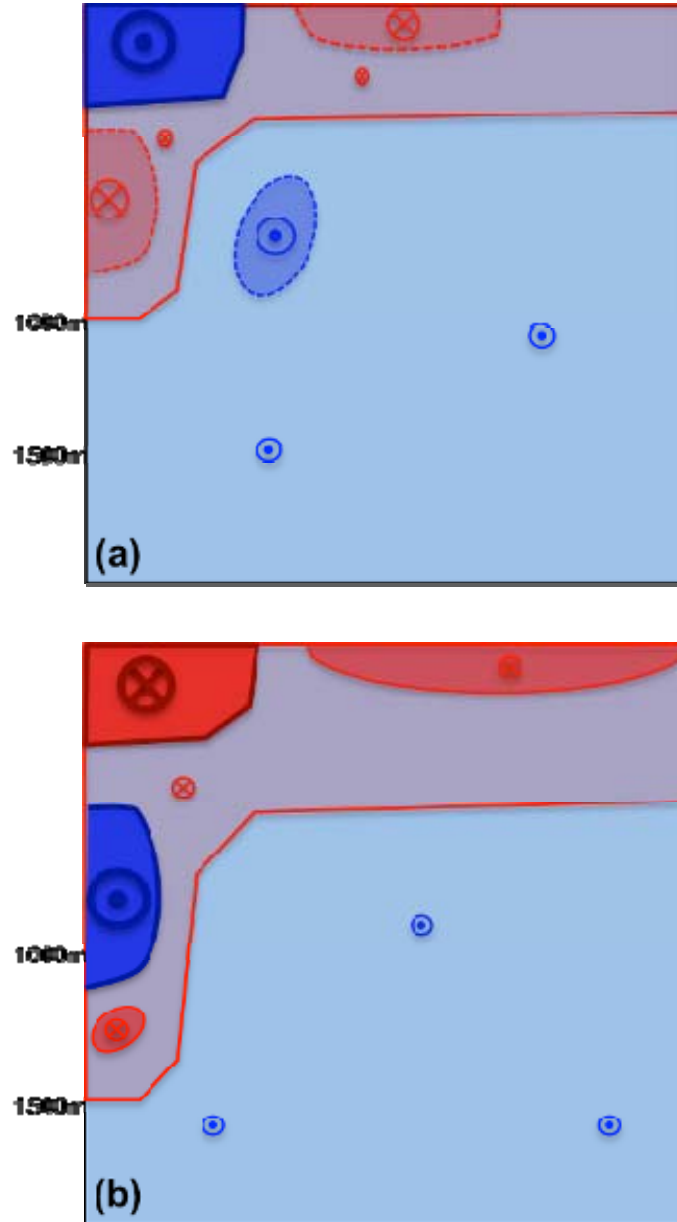
Figure 46. Volume transport across the Equator (looking northward) for experiment 2, cases (a) 13 and (b) 12. Red colors and crossed circles represent northerly flow while blue colors and dotted circles represent southerly flow. Color intensity represents flow magnitude.

As shown in Figure 46, the strongest asymmetry between cases occurs in the deep western boundary. When heating is applied in the southern hemisphere, a Deep Western Boundary Current (DWBC) is fully formed at depth (Figure 46b). This feature counters

the interior circulatory flow, and is of similar density to the interior waters, thus contributing negatively to the equatorial transport and thereby lowering the calculated MOC magnitude. However, when heating is applied to the northern hemisphere mid-latitudes, the DWBC that forms is oriented in the opposite direction, is shallower and slightly weaker, and covers less area than in the southern heating case (Figure 46a).

Though not shown, the ACC forced runs show an equatorial plane structure that is similar to the southern mid-latitude perturbation runs, but the associated DWBC flow is, , weaker. Another feature common to the ACC runs is that the interior flow seems more oriented in a north to south pattern than do all of the other runs. Interior transport measured at the Equator was consistently smaller when positive, and larger when negative, than the interior transport in the non-ACCruns.

When looking at the Walin-based inferred calculations, a pattern can be discerned that is related to the features discussed above. Outside of the ACC, the Walin calculations for both hemispheres give very similar magnitudes, despite the obvious differences with the actual Equatorial transport. For the ACC runs, the Walin calculations seem to be relatively close, and in fact, overstate the actual flow at the Equator. These two observations provide strong evidence that the Walin calculation does not capture the DWBC signal, but does capture the general interior flow forced by the ACC.

Overall, the direct heating runs seemed to provide more consistent correlations between the Walin-based inferred calculations and the actual Equatorial volume flux. In cases 12 and 13, the strong density spike in the lower density regions can be ignored, as they are most likely localized effects that are not connected at depth (see section IV.C.2). Other specific conditions where the Walin-based calculations diverged from Equatorial values can be explained by the presence and structure of the DWBC. This feature does not seem to be captured by the Walin methodology. If this is in fact true, it may mean that the mixed-layer density field does not contain a direct signal from the DWBC. Another interesting feature that appeared in the ACC calculations was a small but systematic density offset between Equatorial and Walin-based calculations. This offset may possibly be attributed to diabatic heating effects.

The distribution of the inter-hemispheric transport—northward or southward—for every case run was positively correlated with the hemispheric location of the heating perturbation. In the majority of cases, including all the configuration two cases, significant features of the equatorial volume flux distribution were correlated in the Walin-RKD calculation. In most of these cases, the general shape and character of the signal, if not the magnitude, is consistent with the Walin-RKD calculation. The differential heating patterns seen within the Configuration 1 cases, especially the WBC perturbation cases, also tend to correlate patterns of interior heat transfer with the ability to detect interior circulation from surface data. Thus, we are lead to two major conclusions: first, significant changes in the internal structure of the ocean circulation system, such as isopycnal outcropping, DWBCs, and interior flow magnitudes, can be affected by the spatial distribution of perturbations in heating. Second, the internal changes in circulation structure at the Equator are connected to the density structure and gradients in the surface mixed-layer. Taken together, these arguments support an adiabatic view of the thermocline dynamics.

VI.   FOR FURTHER STUDY

There are several areas where research may be continued on this topic, some of which are listed below. The simplest extension would be to incorporate salinity forcing. All of the results presented in this study are based upon a truncated linear equation of state, where density changes are solely a function of heating changes. Incorporating salinity will allow a more realistic modeling of the surface forcing mechanisms seen in the ocean. Precipitation, freezing, and evaporative processes could be modeled in a similar manner as SST forcing utilized in this study.

All of the model runs performed for this study utilized symmetric wind-stress forcing and, where applied, a symmetric baseline SST forcing pattern. The use of asymmetric wind stress and heating patterns would provide the chance to study perturbation effects on different global climate landscapes. The Configuration 1 (SST forcing) experiments indicate that perturbations had only a small effect on the MOC. However, adjusting the forcing to more realistic asymmetric patterns may enhance the effects of perturbations. Also, since the Walin-RKD method utilized in this study is theoretically based upon "residual" flows, it is more likely that the Walin-based calculations utilized herein will align with the actual transport at the Equator if asymmetric global patterns are used.

One of the key assumptions in most modeling studies is the assumption that the tidally induced mixing is distributed uniformly in the world ocean. We know, however, that this is not the case: the influence of the moon and sun in relation to the Earth's rotation produce giving rise to tides and contributing to internal wave generation, which are highly variable and depend on the local patterns of topography. It is believed (Munk and Wuncsh 1998; Kuhlbrodt et al. 2007; among others) that this process may provide a mechanism of energy transport into the interior. Another feature that could be incorporated into model runs is double-diffusive mechanics, which may enhance vertical mixing in areas where it is not previously expected. Therefore, a model which could

incorporate more sophisticated models of tidal mixing and double-diffusive processes might be very useful in further diagnosing the importance of adiabatic and diabatic processes in the ocean interior.

APPENDIX: DATA TABLES AND THEORETICAL FORMULATION

A.   DENSITY SCATTERPLOT DATA

Table 2.   Density Values at the MOC maximum (heat flux forced model run; comparison between measured and Walin-based inferred values).

Case	4	5	6	7	8	9	10	11	12	13	14	15
Density of MOC$_{max}$ Walin Calc.	1025.56	1025.71	1025.89	1026.03	1026.01	1026.01	1026.06	1026.08	1025.70	1025.53	1025.52	1025.43
Density of MOC$_{max}$ Equatorial Calc.	1025.57	1025.52	1025.68	1025.76	1025.78	1025.79	1025.79	1025.80	1025.67	1025.54	1025.53	1025.63

Table 3.   Density Values at the MOC maximum (SST forced model run; comparison between measured and Walin-based inferred values).

Case	4	5	6	7	8	9	10	11	12	13	14	15
Density of MOC$_{max}$ Walin Calc.	1024.09	1026.12	1024.06	1025.93	1025.93	1025.94	1026.63	1026.67	1024.88	1025.30	1024.78	1025.06
Density of MOC$_{max}$ Equatorial Calc.	1026.30	1026.10	1025.52	1026.43	1026.45	1026.43	1026.42	1026.35	1024.66	1024.71	1024.68	1024.80

B.   THE RADKO-KAMENKOVICH-DARE FORMULATION

Following RKD (2008) and Dare (2006), the two surface properties used in this study to reconstruct the large scale meridional overturning in the ocean are the mixed-layer density (σ_m) and the air-sea density flux (B). In RKD (2008), the sea surface density flux (B) is defined as:

$$B = -\frac{\alpha H}{C_p} + \beta \rho_0 \frac{(E-P)S}{1-S} \tag{7}$$

where (α, β) are the expansion/contraction coefficients of seawater, ρ_0 is the standard seawater density, H is the heat flux from the atmosphere into the ocean, E and P are the evaporation and precipitation rates, S is the salinity, and C_p is the specific heat capacity of water.   However, for this idealized study evaporation and precipitation are ignored

71

processes, and salinity is treated as a constant, thus eliminating the 2nd right hand term in Equation (7) and reducing the density flux to a function of heat flux only:

$$B = -\frac{\alpha H}{C_p} \qquad (8)$$

Andrews and McIntyre (1976) showed that the distribution of density and tracers in the eddying flows cannot be given by only the Eulerian mean circulation; the distribution must also involve the eddy-induced advection. Therefore, the starting point for our analysis becomes the time-mean density equation that takes into account the eddy fluxes as follows:

$$\vec{V} \cdot \nabla \sigma + \nabla (\overline{\vec{V}' \sigma'}) = \frac{\partial B}{\partial z} \qquad (9)$$

where σ is the time-mean density anomaly, primes denote the perturbations from this mean due to transient eddies, and B represents the vertical density flux due to small-scale processes and air-sea fluxes. While the eddy flux is normally associated with mesoscale variability, it is convenient to include in it all transient processes, such as the effects of the seasonal cycle and variation in the mixed-layer depth.

The eddy fluxes in Equation (9) can be broken down into two distinct components (Radko and Marshall 2006):

- The adiabatic advection by the eddy-induced velocity of the residual mean theory ($\vec{V}^*$), which is assumed to be non-divergent ($\nabla \cdot \vec{V}^* = 0$) ; and

- The remaining diabatic component that can be written without loss of generality as the vertical convergence of the vertical flux $\left(-\frac{\partial B_{eddy}}{\partial z} \right)$.

As a result of this transformation, Equation (9) becomes:

$$\vec{V}_{res} \cdot \nabla \sigma = \frac{\partial \tilde{B}}{\partial z} \qquad (10)$$

where the residual velocity ($\vec{V}_{res} = \vec{V} + \vec{V}^*$) represents the advection of density and tracers by both mean field and adiabatic eddies, and ($\tilde{B} = B + B_{eddy}$) includes the diabatic effects

72

of the small-scale mixing and eddies. This equation is referred to as the residual buoyancy equation. Furthermore, incompressibility is assumed for the residual flows leading to:

$$\frac{\partial u_{res}}{\partial x} + \frac{\partial v_{res}}{\partial y} + \frac{\partial w_{res}}{\partial z} = 0 \tag{11}$$

Following Marshal and Radko (2003), the dynamics of the thin, vertically homogeneous mixed-layer ($-h_m < z < 0$) must be discussed separately from those of the stratified interior ($z < -h_m$). We start with the mixed-layer first; here the residual buoyancy equation takes the form:

$$u_{res} \frac{\partial \sigma_m}{\partial x} + v_{res} \frac{\partial \sigma_m}{\partial y} = \frac{\partial \tilde{B}}{\partial z} \tag{12}$$

where σ_m is the mixed-layer density. Since the mixed layer is assumed homogeneous, integration over its depth results in:

$$U \frac{\partial \sigma_m}{\partial x} + V \frac{\partial \sigma_m}{\partial y} = B_0 + B_{mlc} - \tilde{B}\Big|_{z=-h_m} \tag{13}$$

where $U = \int_{-h_m}^{0} u_{res} dz$, $V = \int_{-h_m}^{0} v_{res} dz$, B_0 is the air-sea density flux, B_{mlc} is the contribution from diabatic eddies in the mixed-layer, and $\tilde{B}\Big|_{z=-h_m}$ is the vertical density flux due to diabatic processes immediately below the mixed-layer.

In Equation (14), total density flux on the right-hand side is assumed to be dominated by the direct forcing term B_0. This assumption is substantiated by Radko and Marshall (2006), and Radko (2006), whose calculations, indicate that B_0 exceeds B_{mlc} by at least an order of magnitude in the ACC and by more on larger planetary scales that are the focus here. In addition, small-scale mixing and diabatic eddy effects represented by $\tilde{B}\Big|_{z=-h_m}$ are significantly reduced below the mixed-layer. Hence these two terms can be dropped and Equation (13) can be approximated by:

$$U \frac{\partial \sigma_m}{\partial x} + V \frac{\partial \sigma_m}{\partial y} = B_0 \tag{14}$$

Next, by integrating the residual continuity equation (Equation 11) over the depth of the mixed layer and noting that the vertical component of the residual velocity vanishes at the sea surface, we arrive at:

$$\frac{\partial U}{\partial x} + \frac{\partial V}{\partial y} = w_{res}\big|_{z=-h_m} \tag{15}$$

For convenience, from this point forward $w_{res}\big|_{z=-h_m}$ will be written as w_{res}.

The next step consists of introducing a convenient measure of the strength of the residual flow that enters (escapes) the mixed-layer at a given sea surface density range. This is readily deduced by taking the integral of w_{res} over an area (S) bounded by two nearby isopycnal surfaces (σ and $\sigma + \Delta\sigma$):

$$G(\sigma) = \iint\limits_{S} w_{res}\, dS \tag{16}$$

This configuration is indicated by the shaded area in Figure 47. The advantage of this formulation is that it allows $G(\sigma)$ to be expressed in terms of the known quantities U and V in Equation (15). By using this relation, and Green's theorem, $G(\sigma)$ can be expressed as a line integral:

$$G(\sigma) = \iint\limits_{S} w_{res}\, dS = \iint\limits_{S} \left(\frac{\partial U}{\partial x} + \frac{\partial V}{\partial y} \right) dS = \oint\limits_{\partial S} (U\, dy - V\, dx) \tag{17}$$

where ∂S is the boundary of the region S.
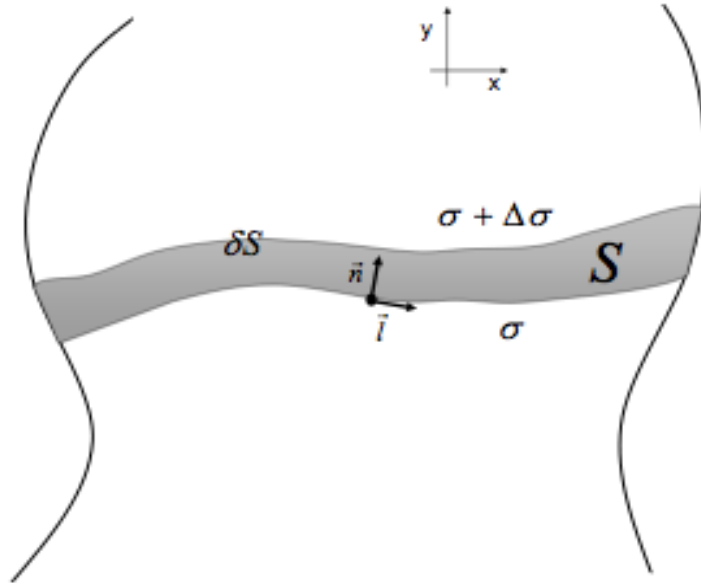
Figure 47.   Left: Surface configuration for evaluation of $G(\sigma)$, (From Dare 2006)

By assuming no flux across the zonal boundaries (if they exist) or the exact cancellation of zonal fluxes in the case of a re-entrant flow, the line integral in Equation (17) simplifies to:

$$G(\sigma) = \int_{\sigma} (Udy - Vdx) - \int_{\sigma+\Delta\sigma} (Udy - Vdx) \qquad (18)$$

where the integration along isopycnals is in the positive x-direction. By introducing the unit vector normal to buoyancy contours, $\vec{n} = \dfrac{\nabla\sigma_m}{|\nabla\sigma_m|}$, Equation (18) is rewritten as:

$$G(\sigma) = \int_{\sigma+\Delta\sigma} \vec{U}\cdot\vec{n}\ \ dl - \int_{\sigma} \vec{U}\cdot\vec{n}\ \ dl \qquad (19)$$

with $\vec{U} = (U,V)$ and l being the arc length along a density contour. Figure 48 provides the schematic interpretation of Equation (19).   Note that Equation (19) essentially represents a mass budget into or out of the parcel that exists between two adjacent isopycnals and between the surface and the base of the mixed layer. Since the mixed layer is assumed homogeneous, density is assumed to be nearly constant within this parcel, and therefore the mass budget also represents a volume budget.

75
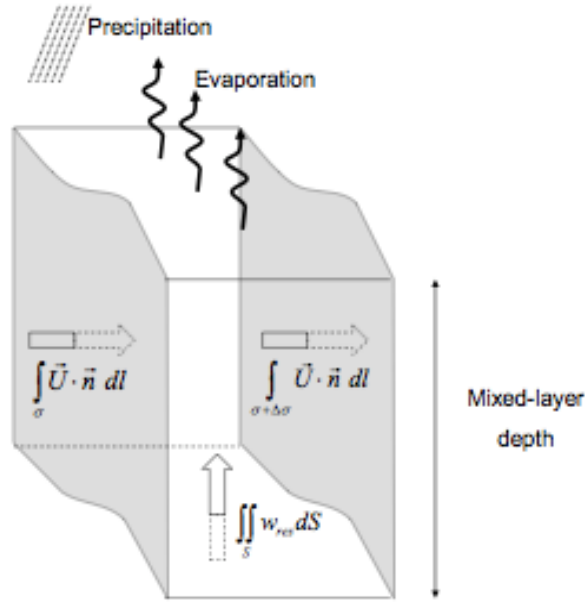
Figure 48.   Mass budget representation for Mixed-layer parcel (From Dare 2006)

Taking the limit $\Delta\sigma \to 0$, Equation (19) becomes:

$$G(\sigma) = \frac{\partial F}{\partial \sigma}\Delta\sigma \tag{20}$$

where

$$F(\sigma) = \int_{\sigma} \vec{U} \cdot \vec{n} \; dl \tag{21}$$

By observing that $\vec{n} = \dfrac{\nabla \sigma_m}{\left|\nabla \sigma_m\right|}$, Equation (14) can be rewritten as $\vec{U} \cdot \vec{n} = \dfrac{B_0}{\left|\nabla \sigma_m\right|}$ and then substituted into Equation (20), yielding:

$$f(\sigma) = \int_{\sigma} \frac{B_0}{\left|\nabla \sigma_m\right|} dl \quad \sigma_1 \text{ and } \sigma_2:$$

$$V(\sigma_1, \sigma_2) = \iint_{S(\sigma_1 < \sigma < \sigma_2)} w_{res} dS = \int_{\sigma_1}^{\sigma_2} \frac{G(\sigma)}{\Delta\sigma} \partial\sigma = F(\sigma_2) - F(\sigma_1) \tag{23}$$

where F(σ) is given by Equation (22).**1.   Diapycnal Volume Flux Calculation**

76

Having obtained an expression for residual volume flux, we can now set up the structure whereby diapycnal and adiabatic fluxes can be calculated. We start by noting that for nearly every density outcropping that occurs in the Southern Hemisphere, one occurs for the Northern Hemisphere. Thus, the density outcroppings are connected as a surface that spans a portion of both hemispheres. However, each density contour has distinct southern and northern values for F, denoted as $F_S(\sigma)$ and $F_N(\sigma)$, respectively. Since residual flow is assumed to be non-divergent, the total diapycnal residual flux across the isopycnal σ (denoted $V_d(\sigma)$) is equal to the flux from the ocean interior into the mixed-layer within the area defined by $\sigma_m < \sigma$ (see Figure 49), or:

$$V_d(\sigma) = \iint_{\sigma' < \sigma} G(\sigma)d\sigma = F_S(\sigma) + F_N(\sigma) \quad for \quad \sigma > \sigma_0 \tag{24}$$

where $V_d(\sigma)$ is defined as positive for an upward integrated flux across the isopycnal. Net diapycnal fluxes into and out of a volume can thereby be evaluated in this manner, within the context of two different surface density contours containing the evaluated volume between them.
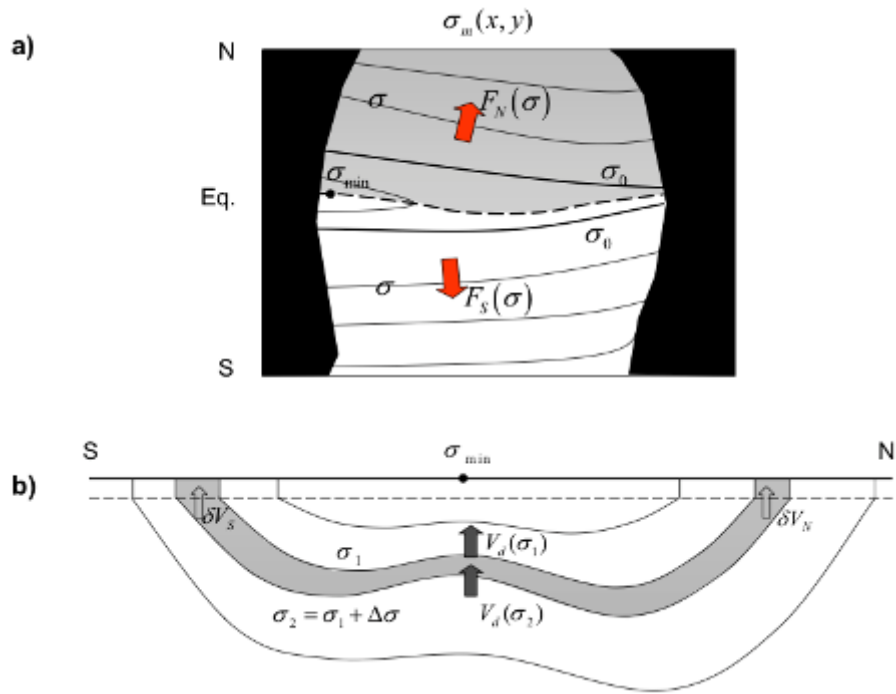
Figure 49.   Schematic of the analytical framework. Once the mixed-layer residual volume fluxes and subduction rates are calculated for a set of isopycnals in each hemisphere, an inter-hemispheric comparison can be made to determine net flow within those isopycnals between the hemispheres (From Dare 2006)

2.   Adiabatic Advection Calculation

In order to quantify the magnitude and pattern of the isopycnal pole-to-pole adiabatic MOC component, the Southern and Northern Hemisphere calculations must be separated. In each hemisphere, the range of possible density values are noted as an interval $\left[\sigma_0, \sigma_{max}\right]$ where σ_0 is an arbitrary value (preferably the lowest density contour occurring in the hemisphere) and σ_{max} denotes the highest density value. Within this interval, in each hemisphere, Equation (23) is used to denote the net residual flux at the bottom of the mixed-layer, as follows:

$$V_N(\sigma) = \iint\limits_{\substack{S(\sigma_0 < \sigma < \sigma_{max}) \\ North}} w_{res} dS = F_N(\sigma_{max}) - F_N(\sigma)$$

$$V_S(\sigma) = \iint\limits_{\substack{S(\sigma_0 < \sigma < \sigma_{max}) \\ South}} w_{res} dS = F_S(\sigma_{max}) - F_S(\sigma)$$

(25)

Since the residual flow in non-divergent, the sum of all fluxes entering the interior volume bounded by the isopycnals σ_{max} and σ is zero, and the sum could be written as:

$$V_d(\sigma_{max}) - V_d(\sigma) - V_N(\sigma) - V_S(\sigma) = 0 \tag{26}$$

If there were no diapycnal flows, Equation (26) would reduce to $V_N(\sigma) = -V_S(\sigma)$ which indicates that all subducted water in one hemisphere is upwelled in the other. In such a case, the isopycnal flux in the density interval $\left[\sigma_0, \sigma_{max}\right]$ is uniform and the adiabatic volume transport, $V_a(\sigma)$ would become $V_a(\sigma) = V_N(\sigma) = -V_S(\sigma)$. This is not the case in the real ocean. Diapycnal fluxes do exist, and therefore isopycnal/adiabatic fluxes cannot be precisely determined from V_S and V_N. However, they can be reasonably estimated by assuming that values of V_a lie in between $-V_S(\sigma)$ and $V_N(\sigma)$. Thus a simple estimate of the isopycnal/adiabatic flux V_a within the density interval $\left[\sigma_0, \sigma_{max}\right]$ is given by a linear average of the two net residual fluxes at the bottom of the mixed-layer:

$$V_a(\sigma) = \frac{1}{2}\left[V_N(\sigma) - V_S(\sigma)\right] \tag{27}$$

Here, positive values of V_a are associated with a downward residual flux at the base of the mixed-layer in the Southern Hemisphere and the corresponding upward flux in the Northern Hemisphere. Further, since the length of the density contours approaches zero as the density value approaches its maximum, the $F_S(\sigma_{max})$ and $F_N(\sigma_{max})$ components of the $V_S(\sigma)$ and $V_N(\sigma)$ calculations (from Equation 25) both become approximately zero. Therefore, Equation (27) reduces to:

$$V_a(\sigma) = \frac{1}{2}\left[F_S(\sigma) - F_N(\sigma)\right] \tag{28}$$

79

3. Extensions on the Preceding Analytical Framework

Another advantage of this construction is that it can be further extended to cases where isopycnal contours do not necessarily interact with land (or a model boundary). Consider an isopycnal (σ) whose contour spans parts of both the Northern and Southern Hemispheres but do not interact with any land boundaries. The line integral across such a contour can be split into a northern and southern component at an arbitrary point (e.g., the Equator). Evaluation of both line integrals in the same sense cancels the Equatorial portion of each component, thus allowing the developed framework to be maintained for this study (see Figure 50).
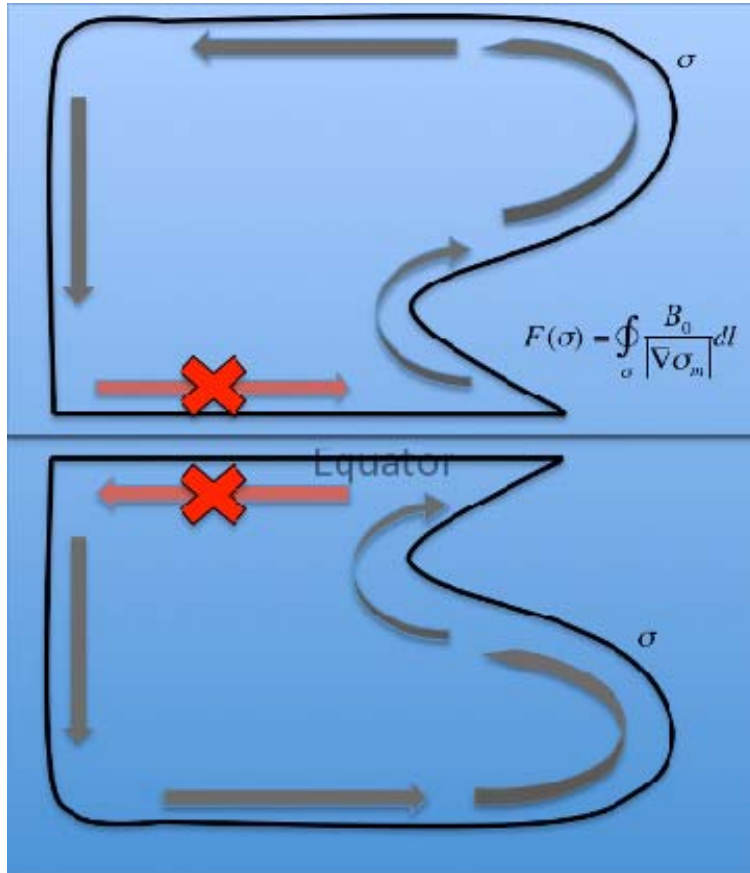

$$F(\sigma) = \oint_{\sigma} \frac{B_0}{|\nabla \sigma_m|} dl$$

Figure 50.   Schematic of the analytical extension. Note the line-integral components along the Equator cancel each other.

LIST OF REFERENCES

Adcroft, A., et al., 2008: *The MITgcm User Manual*. MIT Department of EAPS.

Aguado, E., and J. E. Burt, 2005: *Understanding Weather and Climate*, 4th Ed. Prentice-Hall, 560 pp.

Andrews, D. G., and M. McIntyre, 1976: Planetary waves in horizontal and vertical shear: The generalized-Palm relation and the mean zonal acceleration. *J. Atmos. Sci.*, **33**, 2031–2048.

Boccaletti, G., R. Ferrari, D. Ferriera, A. Adcroft, and J. Marshall, 2005: The vertical structure of oceanic heat transport. *Geophys. Res. Lett.*, **32**, 1–4

Bryan, F., 1987: Parameter sensitivity of primitive equation ocean general circulation models. *J. Phys. Oceanogr.,* **17**, 970–985.

Bryden, H. L., H. Longworth, and S. Cunningham, 2005: Slowing of the Atlantic meridional overturning circulation at 25° N. *Nature*, **438**, 655–657.

Dare, P., 2006: Residual-mean analysis of the air-sea fluxes and associated oceanic meridional overturning. M.S. thesis, Naval Postgraduate School, 10.

De Boer, A. M., J. R. Toggweiler, and D. M. Sigman, 2008: Atlantic dominance of the meridional overturning circulation. *J. Phys. Oceangr.,* **38(2)**, 435–450.

De Boer, A. M., A. Gnanadesikan, N. Edwards, and A. J. Watson, 2010: Meridional density gradients do not control the Atlantic overturning circulation. *J. Phys. Oceangr.,* **40(2)**, 368–380.

Ganachaud, A., and C. Wunsch, 2000: Improved estimates of global ocean circulation, heat transport and mixing from hydrographic data. *Nature*, **408**, 453–457.

Gent, P. R., and J. C. McWilliams, 1990: Isopycnal mixing in ocean circulation models. *J. Phys. Oceangr.,* **20**, 150–155.

Gnanadesikan, A., and Coauthors, 2005: Gfdls cm2 global coupled climate models-part 2: The baseline ocean simulation, *J. Climate*, **19**, 675–697.

Greatbatch, R. J., and J. Lu, 2003: Thermohaline convection with two stable regimes of flow. *J. Phys. Oceanogr.,* **33**, 1618–1632.

Hirschi, J., and J. Marotzke, 2007: Reconstructing the meridional overturning Circulation from boundary densities and the zonal wind stress. *J. Phys. Oceanogr.,* **37**, 743–763.

Kuhlbrodt, T., A. Griesel, M. Montoya, A. Levermann, M. Hofmann, and S. Rahmstorf, 2007: On the driving processes of the Atlantic meridional overturning circulation. *Rev. Geophys.*, **45**, RG2001, doi: 10.1029/2004RG000166.

Ledwell, J.R., A. J. Watson, and C. Law, 1993: Evidence for slow mixing across the pycnocline from an open-ocean tracer-release experiment. *Nature*, **364**, 701–703.

Levitus, S., 1982: Climatological Atlas of the World Ocean. NOAA Tech. Paper 3, 172 pp.

Luyten, J. R., J. Pedlosky, and H. Stommel, 1983: The ventilated thermocline, *J. Phys. Oceanogr.*, **13**, 292–309.

Marshall, J., and T. Radko, 2003: Residual-mean solutions for the Antarctic Circumpolar Current and its associated overturning circulation. *J. Phys. Oceanogr.*, **33**. 2341–2354.

Mignot, J., Levermann, A., and A. Griesel, 2006: A Decomposition of the Atlantic Meridional Overturning Circulation into Physical Components Using Its Sensitivity to Vertical Diffusivity. *J. Phys. Oceangr.,* **36**, 636–650.

Munk, W., 1966: Abyssal recipes. *Deep-Sea Res.,* **13**, 707–730.

Munk, W., and C. Wuncsh., 1998: Abyssal recipes II: energetics of tidal and wind mixing. *Deep-Sea Res.,* **45**, 1977–2010.

Olbers, D., D. Borowski, C. Volker, and J. Wolff, 2004: The dynamical balance, transport and circulation of the Antarctic Circumpolar Current. *Antarctic Science,* **16**, 439–470.

Olbers, D., and M. Visbeck, 2005: A model of the zonally averaged stratification and overturning in the Southern Ocean. *J. Phys. Oceanogr*. **35**, 1190–1205.

Radko. T., and J. Marshall, 2006: The Antarctic Circumpolar Current in Three Dimensions. *J. Phys. Oceanogr.*, **36**, 651–669.

Radko, T., 2005: Analytical solutions for the ACC and its overturning circulation. *J. Mar. Res.*, **63**, 1041–1055.

Radko, T., 2007: A mechanism for establishment and maintenance of the meridional overturning circulation in the upper ocean. *J. Mar. Res.*, **65**, 85–116.

Radko, T., Kamenkovich, I., and P. Dare, 2008: Inferring the pattern of the oceanic meridional transport from the air-sea density flux. *J. Phys. Oceanogr.,* **38**, 2722–2738.

Samelson, R.M., and G. Vallis, 1997: Large-scale circulation with small diapycnal diffusion: two-thermocline limit. *J. Mar. Res.*, **55**, 223–275.

Samelson, R. M., 1998: Large-Scale Circulation with Locally Enhanced Vertical Mixing. *J. Phys. Oceangr.*, **28**, 712–726.

Samelson, R. M., 2004: Simple Mechanistic Models of Middepth Meridional Overturning. *J. Phys. Oceanogr.,* **34**, 2096–2103.

Samelson, R. M., 2009: A simple dynamical model of the warm-water branch of the mid-depth meridional overturning cell, J. Phys. Oceanogr., **39**, 1216–1230.

Sandström, J. W., 1916: Meteorologische Stu- dien in Schwedischen Hochgebirge. *Goteborgs Kungl. Vensk. Vitterh.-Samh. Handin- gar,* **27**, 1–48

Stommel, H., and A. B. Arons, 1960a: On the abyssal circulation of the world ocean – I: Stationary planetary flow pattern on a sphere. *Deep Sea Research*, **6**, 140–154.

Stommel, H., and A. B. Arons, 1960b: On the abyssal circulation of the world ocean – II: An idealized model of the circulation pattern and amplitude in oceanic basins. *Deep Sea Research*, **6**, 217–233.

Stommel, H. M., 1961: Thermohaline convection with two stable regimes of flow. *Tellus,* **13**, 224–230.

Speer, K., and E. Tziperman, 1992: Rates of water mass formation in the North Atlantic Ocean. *J. Phys. Oceanogr., 22,* 93–104.

Timmermann, A., and H. Goosse, 2004: Is the wind stress forcing essential for the meridional overturning circulation? *Geophys. Res. Lett.*, **31**, L04303.

Trenberth, K. E., and J. Caron 2001: Estimates of meridional atmosphere and ocean heat transports, *J. Climate*, **14**, 3433–3443.

Toggweiler, J. R., and B. Samuels, 1993: Is the magnitude of the deep outflow from the Atlantic Ocean actually governed by Southern Hemisphere winds? *The Global Carbon Cycle,* M. Hei- mann, Ed., NATO ASI Series, Vol. I **15**, Springer-Verlag, 303–331.

Toggweiler, J. R., and B. Samuels, 1995: Effect of Drake Passage on the global thermohaline circulation. *Deep-Sea Res.,* **42A**, 477–500.

Toggweiler, J. R., and B. Samuels, 1998: On the ocean's large-scale circulation near the limit of no vertical mixing. *J. Phys. Oceangr.,* **28**, 1832–1852.

Tsujino, H., and N. Suginohara, 1999: Thermohalie circulation enhanced by wind forcing. *J. Phys. Oceanogr*., **29**, 1506–1516.

Tziperman, E., 1986: On the role of interior mixing and air-sea fluxes in determining the stratification and circulation of the oceans. *J. Phys. Oceanogr.* **16,** 680–693.

Walin, G., 1982: On the relation between sea-surface heat flow and thermal circulation in the ocean. *Tellus*, **34**, 187–195.

Webb, D. J., and N. Suginohara, 2001a: The Interior Circulation of the Ocean, in *Ocean Circulation and Climate,* edited by G. Siedler, J. Church, and J. Gould, Academic Press, chapter 4.2, 715 pp.

Webb, D. J., and N. Suginohara, 2001b: Vertical mixing in the ocean. *Nature*, **409**, 37.

Widener, D., 2008: Influence of the Antarctic Circumpolar Current on the Atlantic meridional circulation**.** M.S. thesis, Naval Postgraduate School.

Wunsch, C., and R. Ferrari, 2004: Vertical mixing, energy, and the general circulation of the oceans. *Annu. Rev. Fluid Mech.*, **36**, 281–314.

Wyrtki, K., 1961: The thermohaline circulation in relation to general circulation in the oceans. *Deep-Sea Res.,* **8(1),** 39–64.

INITIAL DISTRIBUTION LIST

1. Defense Technical Information Center
   Ft. Belvoir, Virginia

2. Dudley Knox Library
   Naval Postgraduate School
   Monterey, California

3. Timour Radko
   Department of Oceanography
   Naval Postgraduate School
   Monterey, California

4. Jeff Paduan
   Department of Oceanography
   Naval Postgraduate School
   Monterey, California

5. Philip A. Durkee
   Department of Meteorology
   Naval Postgraduate School
   Monterey, California